



# Shock train and pseudo-shock phenomena in internal gas flows

Kazuyasu Matsuo<sup>a,\*</sup>, Yoshiaki Miyazato<sup>a</sup>, Heuy-Dong Kim<sup>b</sup>

<sup>a</sup> *Department of Energy and Environmental Engineering, Graduate School of Engineering Sciences, Kyushu University,  
Kasuga, Fukuoka 816-8580, Japan*

<sup>b</sup> *Department of Mechanical Engineering, College of Engineering Sciences, Andong National University,  
Andong 760-380, South Korea*

## Contents

1. Introduction	34	7. Pseudo-shocks in flow devices	63
2. Definitions of shock trains and pseudo-shocks	37	7.1. Supersonic wind tunnel diffusers	64
2.1. Shock train	37	7.2. Supersonic inlet diffusers	66
2.2. Pseudo-shock	38	7.3. Inlet/combustor isolators	67
3. The state of the art	41	7.4. Supersonic ejectors	70
4. Properties of pseudo-shocks	42	7.5. Shock tubes	72
4.1. Shape of shock train	42	7.6. Circular thrust gas bearings	74
4.2. Static pressure distributions	44	7.7. MHD power generators	76
4.3. Neumann and Lustwerk's experiment	46	7.8. Other flow devices	78
4.4. Static pressure ratio across pseudo-shock	47	8. Control methods of pseudo-shocks	81
4.5. Length of pseudo-shock	48	8.1. Boundary layer suction	81
5. Numerical calculations on shock trains	49	8.2. Passive control	83
5.1. Review of previous studies	49	9. Self-excited oscillations of pseudo-shocks	86
5.2. Flow structure in shock train region	50	9.1. Shock oscillations in transonic diffusers	87
5.3. Pressure rise in shock train region	53	9.2. Oscillations of shock trains	90
6. Flow models of pseudo-shocks	54	9.3. Correlation between shock oscillations and pressure fluctuations	91
6.1. Shockless model	54	10. Concluding remarks	94
6.2. Diffusion model	56	References	95
6.3. Modified diffusion model	59		
6.4. Other flow models	60		

---

\* Corresponding author. Tel.: 00 81 92 583 7588; fax: 00 81 92 592 0211; e-mail: matsuo@ence.kyushu-u.ac.jp

Notation

$A$	cross-sectional area	<i>Greek letters</i>	
$C_f$	coefficient of friction	$\gamma$	ratio of specific heats of gas
$C_p$	specific heat at constant pressure of gas	$\delta$	boundary layer thickness
$D$	diameter or equivalent diameter of duct	$\delta^*$	boundary layer displacement thickness
$h$	half-height of duct	$\theta$	boundary layer momentum thickness
$H$	height of duct	$\mu$	fractional mass flow rate (see Section 6.1)
$L$	streamwise length scale	$\rho$	density
$m$	mass flow rate	<i>Sub/superscript</i>	
$M$	Mach number	0	total or stagnation state
$p$	static pressure	1	just upstream state of normal shock or pseudo-shock
$p_0$	stagnation or total pressure	2	just downstream state of normal shock or pseudo-shock
$r$	radial distance	a	atmospheric state
Re	Reynolds number	b	ambient state
$t$	time	e	freestream state outside of boundary layer, duct exit
$T$	temperature	n	normal shock
$u$	streamwise velocity	p	plenum chamber or supply state, pseudo-shock
$w$	Crocco number ( $\equiv$ (flow velocity)/(limiting velocity) $= u/\sqrt{2C_p T_0}$ )	rms	root mean square value
$w^*$	Crocco number at sonic condition ( $= \sqrt{(\gamma - 1)/(\gamma + 1)}$ )	*	sonic state or throat state
$x$	streamwise coordinate		
$y$	transverse coordinate		

Abstract

The interaction between a normal shock wave and a boundary layer along a wall surface in internal compressible flows causes a very complicated flow. When the shock is strong enough to separate the boundary layer, the shock is bifurcated and one or more shocks appear downstream of the bifurcated shock. A series of shocks thus formed, called “shock train”, is followed by an adverse pressure gradient region, if the duct is long enough. Thus the effect of the interaction extends over a great distance. The flow is decelerated from supersonic to subsonic through the whole interaction region. In this sense, the interaction region including the shock train in it is referred to as “pseudo-shock” in the present paper, as Crocco called it. The shock train and pseudo-shock strongly affect the performance and efficiency of various flow devices. In the present review some fundamental characteristics of the shock train and pseudo-shock are first described. Some simple predictions are made to simulate these very complicated phenomena. Pseudo-shocks appearing in various flow devices are explained. Control methods of the pseudo-shocks are also described. Finally, the current understanding of self-excited oscillation of pseudo-shock is reviewed. © 1999 Elsevier Science Ltd. All rights reserved.

1. Introduction

Since the pioneering work of Ernst Mach, a shock wave has been long treated as a discontinuity. In many practical situations, the shock wave, whether it is normal or oblique to flow direction, nearly always meets wall surfaces on which a boundary layer develops. Then a complex interaction

phenomenon between the shock wave and the boundary layer occurs at the foot region of the shock. Under this circumstance, the shock can no longer be a discontinuity but is characterized by a finite adverse pressure gradient.

For the past five decades, the shock/boundary layer interaction phenomenon has been the subject of many research studies. Much has been learned from both experimental and theoretical researches. These researches showed that the interaction significantly influences the entire flow field, especially when the shock is strong enough to separate the boundary layer.

The interaction phenomenon is frequently present on a variety of flow fields such as aerofoils, aircraft bodies, missiles, to name a few. Comprehensive reviews on the interaction phenomenon were given by many researchers, Green [1] and Delery [2], for example. These works made a great contribution to make clear the interaction physics for “external” flows such as flows around aerofoils. It has been recognized that the interaction in the external flows is largely influenced by the flow Mach number just upstream of the shock, the Reynolds number based upon the boundary layer thickness at the foot of the shock, and the body configuration, being related to the longitudinal pressure gradient imposed to the interaction field.

Very frequently, the shock wave/boundary layer interaction has also been found in “internal” flows. With most of the interaction flows appearing in a variety of flow devices including ducts, pipelines, supersonic wind tunnels, supersonic inlets of aircraft engines, supersonic ejectors, etc., a normal shock is formed at a position in the flow passage, depending on the pressure conditions imposed at both upstream and downstream of the flow passage, the passage geometry, and the wall friction due to viscosity. Under this situation, the physics of the interaction may be different from our previous understanding that has been obtained from the external flows so far.

For the sake of the design of supersonic wind tunnel diffusers, Neumann and Lustwerk [3,4] conducted an experiment with a constant area tube for conditions wherein a normal shock was present in the tube. They showed that an ideal shock which was assumed for the case of no boundary layer was never obtained and instead, due to the presence of the boundary layer, the pressure rise by the shock extended from 8 to 12 tube diameters. Their experiment in Ref. [3] published in 1949 was probably the first extensive one on the shock/boundary layer interaction in internal flows.

Also, in relation to the supersonic wind tunnel diffuser, Lukasiewicz [5] reviewed shock compressions in ducts in 1953. He said that “the region of shock compression may involve several curved or oblique shocks, forming regular or Mach-type reflections”. Shapiro [6] referred to “normal shock in ducts” in his famous textbook published in 1953, quoting the experimental data in Ref. [3] and explained “a series of bifurcated normal shocks”. Since that time, many researches have been devoted to this very important practical problem in internal flow passages. For example, to the authors’ knowledge, even the papers on normal shock/boundary layer interactions in “a duct with a constant area” amount to more than 40, about a half of which are listed in Refs. [7–28].

According to the previous studies [6,11,15,29,30], the flow pattern of the interaction between a normal shock and a turbulent boundary layer in a constant area duct can be classified into four different possible configurations, as schematically illustrated in Fig. 1. In the case of the freestream Mach number  $M_{1e}$  just upstream of the shock less than about 1.2, as shown in Fig. 1a, the interaction is so weak that the shock is straight and normal to the flow, being very close to an inviscid normal shock. No separation appears in this case. The case for the Mach number between

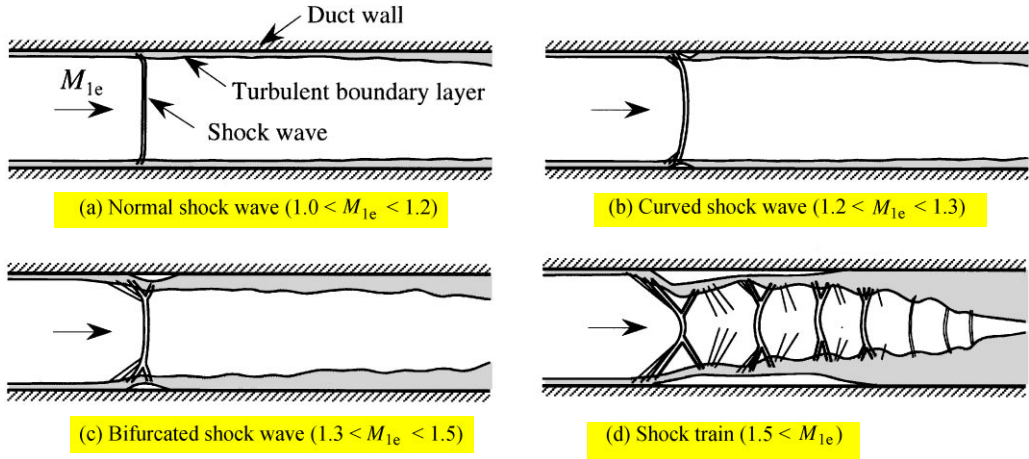


Fig. 1. Schematic sketch of normal shock wave/turbulent boundary layer interaction in a constant area duct.

about 1.2 and 1.3 is illustrated in Fig. 1b. The interaction is fairly weak and the shock changes inclination continuously with increasing distance from the wall. The boundary layer may not separate or separates at the foot of the shock, but there is a strong tendency towards reattachment. As the Mach number increases further, a single nearly normal shock with bifurcated ends is observed, as shown in Fig. 1c, as the results of boundary layer separation and the separation is extensive, showing little tendency to reattach.

The interaction becomes significant for high Mach numbers, and for the Mach number over about 1.5, as illustrated in Fig. 1d, one or more shocks appear downstream of the bifurcated shock. A series of shocks in line, as shown in Fig. 1d, has been called in many ways in various papers, and we use the term “shock train” in the present paper to indicate such a sequence of shocks. The detail of this terminology will be discussed in Section 2.1.

The supersonic flow upstream of the shock train is decelerated and the wall static pressure increases through the shock train region. The important experimental fact, which will be described later in Section 2.2, is that the static pressure continues to rise after the shock train over a certain distance along the duct, “if the duct is long enough”. In this case, the static pressure recovery is performed through both the shock train region and the subsequent static pressure recovery region. The details will be discussed in Section 4.2.

In 1958, Crocco [31] pointed out regarding duct flows that “a simple normal shock is not, in most cases, the proper mechanism of transition from the supersonic to the subsonic conditions, and the actual mechanism is more complicated, leading to a more gradual transition which is substantially different from the simple discontinuity of a normal shock”. He called this transition process “pseudo-shock”. In the present paper, the term “pseudo-shock” is used to indicate the flow region from the head of the shock train to the end of the subsequent static pressure recovery region mentioned above. This terminology will be also discussed in Section 2.2.

In recent years, the shock train and pseudo-shock phenomena have received increasing attention because of its importance in industrial fields as well as many phenomenological aspects which still remain unanswered. It has become necessary to understand fully the mechanism of the shock train

and pseudo-shock phenomena in order that prediction methods and control strategies are developed and hence plants or flow devices are designed and operated with good performance.

This review describes the mechanism of the shock train and pseudo-shock phenomena, with emphasis on the physics of the normal shock/boundary layer interaction involved in these processes. This paper contains 10 sections. At first, the definitions of the shock trains and pseudo-shocks are clearly given in Section 2. The state of the art of these phenomena is mentioned in Section 3. Section 4 describes the flow properties with regard to the shock trains and pseudo-shocks. Some results and the problems in relation to numerical calculations on these phenomena are mentioned in Section 5. Some flow models for the pseudo-shocks are described in Section 6. In Section 7 some examples of the pseudo-shocks in various flow devices are presented. Section 8 contains some control methods of the pseudo-shock flows in ducts. Flow unsteadiness due to the self-excited oscillations of the pseudo-shocks is discussed in Section 9. Finally, Section 10 contains concluding remarks.

## 2. Definitions of shock trains and pseudo-shocks

### 2.1. Shock train

As mentioned above, we refer to such a series of repeated shocks as shown in Fig. 1d as a “shock train”. A typical **schlieren photograph** of the shock train is shown in Fig. 2. This photograph was taken in Kyushu University in Japan and reported in the paper [32] written in Japanese published in 1969. The duct has a square cross-section of  $32 \times 32 \text{ mm}^2$ , and the flow is from left to right. The freestream Mach number  $M_{1e}$  just upstream of the first shock is equal to 1.75 and the Reynolds number based on the equivalent diameter of the duct is  $8.2 \times 10^5$ . The interaction was generated under a fully developed turbulent boundary layer.

By “region of shock train”, we represent the region where the series of shocks in line can be visible by optical observations. The region of shock train in Fig. 2 contains about ten normal shocks. It should be pointed out here that, as will be described in Section 4.2, at **the end of the shock train the flow is not fully subsonic but still mixed supersonic-subsonic, with the supersonic portion decelerating to subsonic without shocks** [17,22].

Up to the present, the “shock train” defined above has been called in many ways by many researchers, such as multiple-branch shock [33], shock system [34], etc., as listed in Table 1. As far as the authors know, the term “shock train” was first used by Billig [35] in 1988. Since then, this

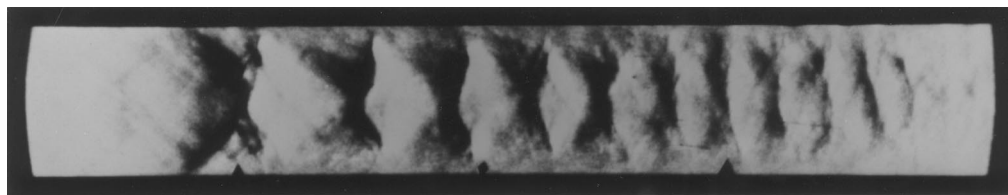


Fig. 2. Schlieren photograph showing shock train in rectangular duct ( $M_{1e} = 1.75$ , reproduced from Ref. [32]).

Table 1  
Examples of a synonym of “shock train” in various references

Year	Authors	Technical term
1953	Lukasiewicz [5] Cohen and Valerino [33] Shapiro [6]	Several curved or oblique shocks Multiple-branch shock A series of bifurcated normal shocks
1958	Crocco [31]	A series of X shocks
1964	Faro [34]	Shock system
1973	Waltrup and Billig [9]	A series of shocks
1985	Om and Childs [17]	Multiple shock
1990	Carroll and Dutton [22]	A series of nearly normal shocks
1991	Lin et al. [38]	Multiple normal shocks
1992	Carroll and Dutton [24] Sullins and McLafferty [40]	A series of oblique shocks Bifurcated normal shock waves
1993	McCormick [25]	Lambda foot shock system
1996	Nill and Mattick [27]	A series of shocks

term is used in the papers [22,27, 36–40]. In Refs. [22,36–39], this term is used exactly as the same meaning as that defined in this paper. On the other hand, in Refs. [27,40], this term is used to indicate the flow of “pseudo-shock” which will be defined in the next section.

## 2.2. Pseudo-shock

First of all, in order to understand the features of duct flows including the shock train, a typical static pressure distribution [7] obtained experimentally in a constant area rectangular duct of  $40 \times 50 \text{ mm}^2$  is shown in Fig. 3b. The experimental conditions of the freestream Mach number  $M_{1e}$ , the ratio of the boundary layer thickness just upstream of the shock train to the duct half-height  $\delta_1/h$ , etc., are shown in the figure. The horizontal axis represents the distance from the first shock position at the centerline of the duct, and the vertical axis is the ratio of local static pressure to the stagnation pressure of the upstream flow of the shock. The curve marked 1 shows the pressure distribution measured along a horizontal line 0.4 mm above the bottom wall ( $y/h = 0.02$ ), and the curve marked 2 along the centerline of the duct. These curves were exactly reproduced from Ref. [7].

Curve 1 in Fig. 3b is considered to be nearly the same as the static pressure distribution along the duct wall and shows that the pressure increases monotonically. Curve 2 indicates that the pressure at the centerline rises and falls repeatedly as a result of the presence of the successive normal shocks in the shock train. It should be noted that curve 1 overlaps with curve 2 after the point j, and this point may be located near the end of shock train. Behind this point, the pressure still increases.

Fig. 3a shows a supposed schematic illustration of the flow structure in the shock train region corresponding to the same experimental conditions of Fig. 3b. In drawing the illustration, the Mach number contours of both the experiment of  $M_{1e} = 1.5$  in Ref. [17] and the experiment of  $M_{1e} = 1.6$  in Refs. [22,24] were referred. This illustration will be referred later in Section 4.2.

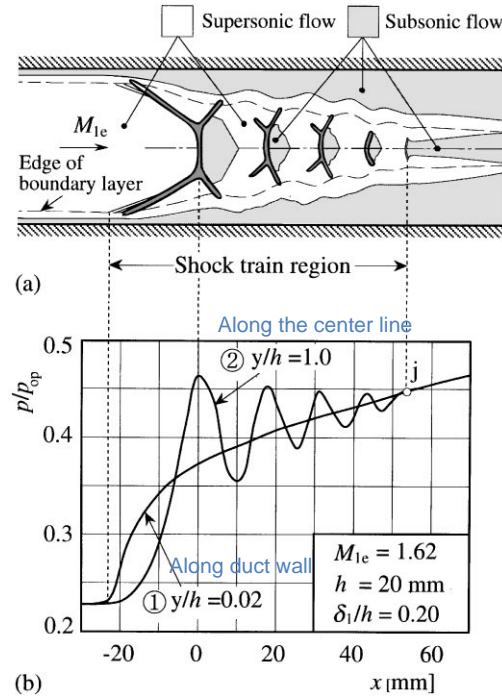


Fig. 3. Static pressure distributions and structure of flow with shock train in constant area passage (Experimental data from Ref. [7]). (a) Schematic sketch showing flow structure in shock train region. (b) Static pressure distributions.

Fig. 4 shows an illustration of the shock train shown in Fig. 2 and the corresponding static pressure distributions at the wall and at the centerline of the duct drawn supposedly and schematically, by referring to the experimental results of Refs. [7,8,17]. As shown in this figure, the pressure begins to rise at the point 1 where the foot of the first shock of the shock train is located, and increases continuously at the wall, but fluctuates at the centerline up to the point j, as mentioned above. This pressure rise between the points 1 and j is caused by the shock train.

If the flow is fully subsonic and uniform at the point j in Fig. 4, then the static pressure downstream of this point should decrease along the duct due to the frictional effect. However, it should be noted that the shock train is followed by the “mixing region” as shown in the figure. In this region there exist no shocks, but the pressure increases to some extent and the pressures at the wall surface and at the centerline are the same. Whether this mixing region, in other words, post-shock train adverse pressure gradient region, appears or not depends on the duct length, as will be explained in Section 4.2, and if the duct is long enough, it may appear. In such a case the static pressure reaches maximum at the point 2, and after this point the pressure gradually decreases. The flow mechanism in the “mixing region” will be discussed later in Section 4.2.

Since the static pressure rises from the point 1 to the point 2 and the flow is evidently supersonic and subsonic at the points 1 and 2, respectively, it may be reasonable to regard this region, that is, the “whole interaction region between the normal shock and the boundary layer”, as a “normal shock”. However, it is not a real shock, although it contains a series of genuine shocks of the “shock



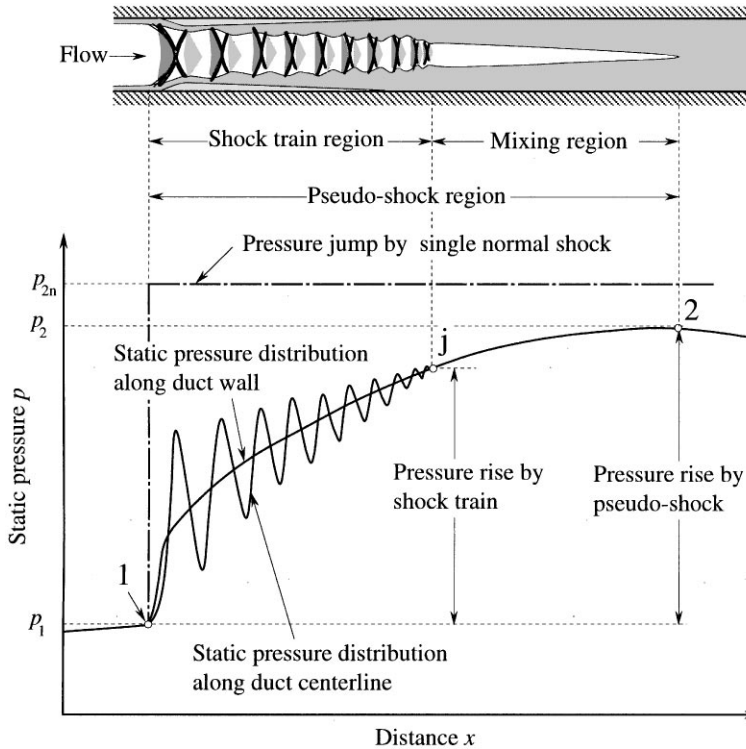


Fig. 4. Schematic static pressure distribution along duct centerline and wall surface in constant-area duct for condition wherein a “normal” shock is present.

train” within it. Hence we refer to this region as “pseudo-shock”, as Crocco [31] called it, although the authors think that he should have called it “pseudo-normal shock”.

If no boundary layer is present, the pressure rises “discontinuously” from  $p_1$  to the Rankine-Hugoniot value  $p_{2n}$  by a single normal shock, as shown in Fig. 4. In real flows, the pressure rise extends over a great distance rather “continuously” to the value  $p_2$ . The value  $p_2$  is in general smaller than  $p_{2n}$ , which will be shown in Section 4.4. The pseudo-shock region, which is defined as the region between the points 1 and 2, has been expressed in many ways in previous papers: for example, “shock region” in Refs. [3,6], “region of shock compression” in Ref. [5], “pressure recovery zone” in Ref. [13]. In this way, up to present, a variety of technical terms have been used in confusing way in order to describe the shock train and pseudo-shock phenomena.

The definition mentioned above may be difficult to distinguish the “pseudo-shock” from the “shock train” except for the case of long and nearly constant area ducts where the “mixing region” may appear. Hence, in the present paper, we use the term “shock train” when we pay attention to the series of successive shocks caused by the normal shock/boundary layer interactions, and, when the “whole interaction region” is considered to play a part of a single normal shock in flow passages, we use the term “pseudo-shock” in order to represent the whole interaction region.

The pseudo-shock plays a very similar role as a single normal shock in the sense that the flow is decelerated from supersonic to subsonic, etc. Therefore, the normal shock in internal flows in the



simplest assumption should be replaced by the pseudo-shock in more rigorous analysis, and it should be noted that, **since the pseudo-shock is formed by the interaction of a normal shock with a boundary layer, the flow properties and flow pattern in the region are greatly affected by the boundary layer as well as the Mach number just upstream of the shock.**

### 3. The state of the art

Shock wave is a kind of abrupt disturbance that leads to discontinuous and irreversible changes in such flow properties as pressure, temperature, etc. According to the history of shock wave written in Ref. [41], etc., Stokes first found the existence of such a discontinuity in flow field in 1849, and then Mach presented a clear visual evidence of the shock in 1886. Rankine in 1870 and Hugoniot in 1887 defined the thermodynamic properties regarding the shock, separately. However, they did not relate the shock properties to the second law of thermodynamics. Later, Rayleigh and Taylor showed that the equations suggested by Rankine and Hugoniot can be applied to only compressible shocks because those are reasonable physically.

In many engineering practices, it is frequently required that we do not treat the detailed structure of the shock, but primarily we are concerned with the net changes in the flow properties across the shock. If we assume that no normal shock/boundary layer interaction is present in an internal flow, then the thickness of the normal shock is generally of the order of molecular mean free path [42]. In real flows, the shock necessarily interacts with the boundary layer along the wall surfaces, and in the case of a strong interaction, the shock no longer remains a single shock, but gives way to the “shock train” or “pseudo-shock”.

A great deal of research studies have been made on shock waves in various academic fields. Now the term “shock wave” is very familiar, but the “shock train” or “pseudo-shock” seems to be not so well known. In recent years, there has been an increasing need for elevating the operating gas pressure at plants or industrial fields, and a shock can be formed in pipe lines or in flow elements such as valves and orifices to meet the prevailing pressure conditions. The simplest theoretical prediction for such a circumstance is to consider only a single normal shock. But, as mentioned above, in such an internal flow, the pseudo-shock should be considered instead of a normal shock. These phenomena are also very important in various flow devices operating at supersonic speed such as air inlets of supersonic aircraft engines, which will be described in Section 7.

Recently, the problem of shock trains and pseudo-shocks has been one of the most challenging problems in computational fluid dynamics. Some kinds of turbulence models were incorporated into multi-dimensional compressible viscous equations [37,38,43–46], and the detailed flow field, that could not have traced by experiment, was revealed, to some extent. What is practically obtained from such calculations was, however, not so much as expected. Furthermore, the computational results are often not in agreement with experiments. The main reason for this is probably that the effects of turbulence and viscosity are not accounted for correctly due to deficiencies in the turbulence modelling (see Knight [47], Viegas and Horstmann [48]). Also the phenomena associated with the shock-induced separation, reattachment, flow unsteadiness, etc., cannot be predicted correctly. Some of the results of numerical calculation will be shown in Section 5.

In general, describing complicated flows by a simple model may be useful to understand the essential features of the flow. As for the pseudo-shocks in a constant area duct, the first flow model called “shockless model” was proposed by Crocco [31] in 1958. Since then, some flow models have been presented in Refs. [11,15,49–52]. These models will be explained in Section 6.

On the other hand, the development of the recent measurement techniques gave considerable help in grasping the physics of the pseudo-shocks. A laser doppler velocimeter system was employed to obtain the quantitative data on the pseudo-shocks in Refs. [22–24, 28]. But some data are still open to questions: for example, whether the tracer particles can trace the gas flow well, particularly in the region near the foot of the shock. Furthermore, one of the important factors which makes the experiment of the shock trains difficult is that each shock of the shock train is not located at a fixed point but it oscillates with time about its time-mean position, even if the upstream and downstream pressures are kept constant. The details of the self-excited oscillations of the shock trains will be explained in Section 9, by referring to Refs. [53–57].

To summarize, as the shock train and the pseudo-shock phenomena are extremely complex, they are not well understood in spite of great effort of research in this area. However, they should be fully understood from the viewpoint of engineering and industrial practices. Its detailed mechanism should be also known for obtaining appropriate control strategies so that a system design is able to reflect those. It should be worthwhile noting that the unsolved problems would be answered by both more systematic experiments and more sophisticated numerical calculations.

#### 4. Properties of pseudo-shocks

In order to design and/or operate flow devices in which shock trains or pseudo-shocks are supposedly present, it will be required to estimate the pressure distribution along the flow direction, the pressure rise, and the length necessary to fully achieve the pressure rise. Before progressing to pseudo-shocks in a variety of flow devices, this section deals with such properties of the pseudo-shocks in straight flow passages with constant area, under adiabatic wall condition.

##### 4.1. Shape of shock train

The shape of each shock constituting the shock train in the pseudo-shock region is mainly affected by the Mach number and the boundary layer just upstream of the shock train. The effect of the latter is referred to as “flow confinement” effect, as characterized by the ratio of the undisturbed boundary layer thickness to the duct half-height or duct radius in axisymmetric geometries.

A series of photographs [22] which clearly reveal the effects of the flow confinement on the shape of shock train in a rectangular duct are reproduced in Fig. 5. The flow is from left to right. The incoming Mach number  $M_{1e}$  and the unit Reynolds number per meter were held constant at 1.6 and  $3 \times 10^7$ , respectively, and the flow confinement parameter,  $\delta_1/h$ , where  $\delta_1$  is the upstream boundary layer thickness and  $h$  is the duct half-height, was varied. The top photograph shows the shock positioned near the nozzle exit, where the boundary layer is thinnest.

Proceeding from top to bottom in Fig. 5, the shock is progressively further from the nozzle exit and the boundary layer is correspondingly thicker. The first shock in all cases is bifurcated, while the subsequent shocks are not. It is clearly visible that within the single shock train in each

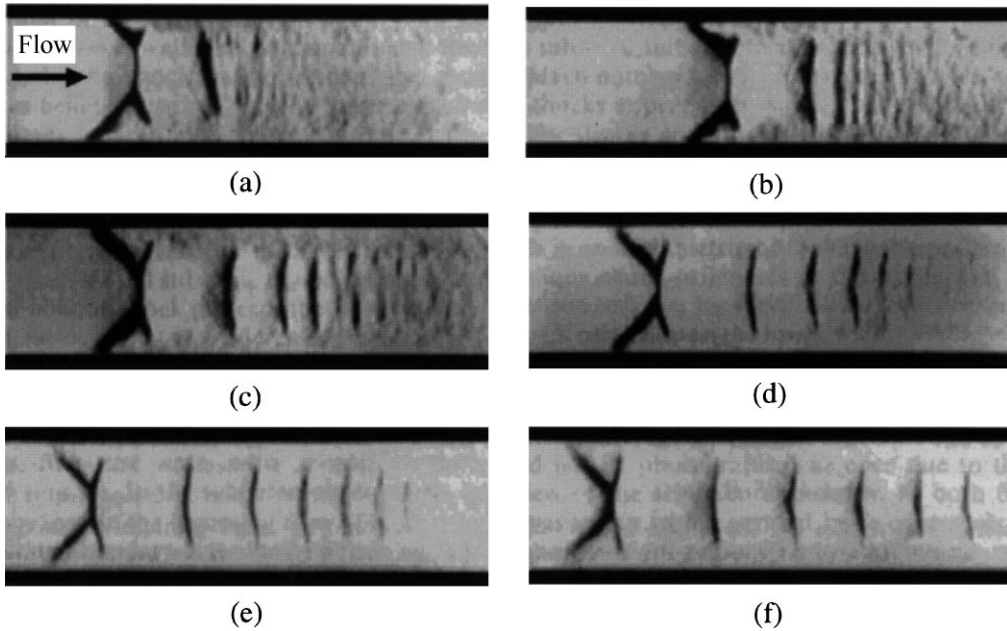


Fig. 5. Schlieren photographs reproduced from Ref. [22] ( $M_{1e} = 1.6$ ). (a)  $\delta_1/h = 0.08$ ; (b)  $\delta_1/h = 0.14$ ; (c)  $\delta_1/h = 0.27$ ; (d)  $\delta_1/h = 0.32$ ; (e)  $\delta_1/h = 0.40$ ; (f)  $\delta_1/h = 0.49$ .

photograph, the spacing between two successive shocks decreases. Also, it can be noted from these photographs that, when the Mach number  $M_{1e}$  is kept constant and the flow confinement parameter  $\delta_1/h$  increases, the number of shocks and the spacing between two successive shocks increase, and hence the length of the shock train also increases. Likewise, as the Mach number increases, the number of shocks, the spacing between two consecutive shocks, and the length of shock train increase to some extent [38].

In case of a moderate normal shock/boundary layer interaction, as shown in Figs. 2 and 5, the normal part of the leading shock is still present in the central part of the duct. We call such a shock train “normal shock train”. With further increase in flow Mach number and for a significant interaction, the point of bifurcation of the leading shock moves away from the wall and reaches the centerline of the duct. Then the normal part of the leading shock disappears. This type of shock train is called “oblique shock train”.

For the oblique shock train, the number of shocks and the spacing between two consecutive shocks are less sensitive to the change of the flow confinement [22,38]. The primary difference between normal and oblique shock train stems from the difference in Mach number. Generally, the oblique shock train is observed for interactions of Mach number larger than 1.8–2.2 [8,11,37,38], depending on the state of boundary layers.

Om and Childs [17] performed an experiment of the shock train phenomena in a constant area circular duct at a freestream Mach number of 1.49 and a Reynolds number of  $4.90 \times 10^6$  per meter. From their detailed pitot, static, and wall pressure measurements, they obtained the axial distribution of the boundary layer displacement thickness. Based on the result, they made an equivalent

one-dimensional flow model regarding the formation of each shock in the shock train. According to this model, the displacement buildup due to the first shock is large enough to choke the flow. The subsonic flow, immediately behind the first shock, accelerates in the converging flow passage until the sonic state is reached. After that, supersonic expansion takes place and this supersonic region is terminated by the formation of the second shock, and the same process occurs. In this way, it seems that reacceleration of the flow following each shock is caused by adjustments in the wall boundary layer.

#### 4.2. Static pressure distributions

As mentioned in Section 2.2, the shock train is followed by the mixing region where static pressure recovery is achieved to some extent without shocks, if the duct is long enough. An example [40] of such a flow is shown in Fig. 6. This was measured on the wall in a rectangular constant area duct, and the freestream Mach number ahead of the shock was 2.0. The vertical axis represents the ratio of the local static pressure  $p$  to the static pressure  $p_1$  just upstream of the shock train, and the horizontal axis denotes the distance from the duct entrance. This figure has been modified a little from the original one in order to make it more intelligible, but the values of the experimental points and the position and length of the shock train region are reproduced exactly from Ref. [40]. The static pressure rises from  $p_1$  at the point 1 to about  $3.2p_1$  at the point j by the shock train, and then rises to about  $3.6p_1$  at the point 2 through the mixing region. The value of  $3.6p_1$  is 80% of the pressure recovery of  $4.5p_1$  by the normal shock. The pressure rises rapidly in the shock train region and then continues to rise rather moderately up to the point 2.

According to the previous studies [17,22,40], the reason why the pressure rises from the point j to the point 2 in Fig. 6 is considered as follows: As shown in Fig. 3a, the flow outside the boundary layer remains supersonic throughout the shock train region, but in the core region, the flow

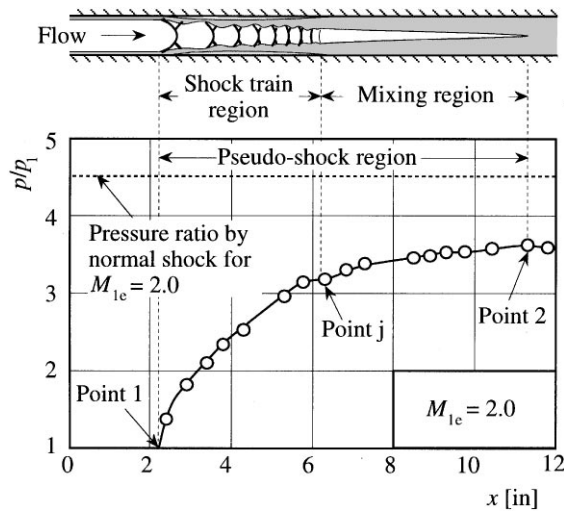


Fig. 6. Static pressure distribution along wall in rectangular duct (Experimental data from Ref. [40]).

undergoes successive changes from supersonic to subsonic by the series of normal shocks. Hence, the flow remains mixed supersonic–subsonic at the end of the shock train, although normal shocks cease to exist in the core flow. Behind the shock train, the mixing of a highly non-uniform profile created in this way by the shock train gives rise to pressure rise. Once the flow reaches subsonic speeds, friction tends to accelerate the flow. At some point, the pressure decrease due to Fanno flow is greater than the increase due to mixing, and a maximum pressure is reached, followed by a gradual decrease in pressure. The maximum point in pressure is just the end of pseudo-shock.

When the duct is not long enough, the static pressure recovery region between the points j and 2 in Fig. 6 becomes shorter, and the pressure recovery in this region reduces. An example of such a case is shown in Fig. 7. This experiment was conducted by Waltrup and Billig [9], prompted by the design of scramjet engines. In this experiment, compressed air was fed through a contoured axisymmetric nozzle into constant area cylindrical ducts whose exits were either open to the atmosphere or throttled through a butterfly valve.

Fig. 7 shows the axial distributions of wall static pressure  $p$  normalized by the plenum pressure  $p_{op}$ . The horizontal axis denotes the distance  $x$  from the duct inlet (nozzle exit), and the duct exit is located at  $x = 578$  mm as shown in the figure. In all cases, the static pressure at the duct exit is the external pressure whether it be atmospheric or that generated by throttling. Evidently, the pressure rise in each case is performed only by the shock train, and there appears no subsequent pressure rise. A striking feature of these results is the similarity in shape and slope of all of the profiles. This suggests that the shock train structure for the tests with  $p_{op}$  higher than the minimum  $p_{op}$  (310 kPa) represents just a proportional part of the shock train structure in the minimum case.

After statistically analyzing their experimental results, Waltrup and Billig [9,58] developed the following empirical relationship between the pressure distribution in the shock train region and

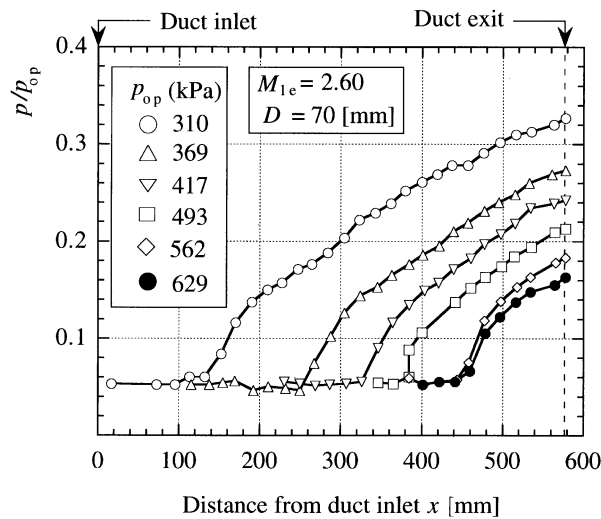


Fig. 7. Wall static pressure distributions in short cylindrical duct wherein a shock-train is included (Experimental data from Ref. [9]).

several duct flow parameters:

$$\frac{x(M_1^2 - 1) \text{Re}_\theta^{1/4}}{D^{1/2} \theta_1^{1/2}} = 50 \left( \frac{p}{p_1} - 1 \right) + 170 \left( \frac{p}{p_1} - 1 \right)^2 \quad (1)$$

where  $x$  is the distance downstream from the beginning of the pressure rise,  $M_1$  is the Mach number of approach flow,  $\theta_1$  is the boundary layer momentum thickness for undisturbed flow,  $D$  is the diameter,  $\text{Re}_\theta$  is the Reynolds number based on boundary layer momentum thickness, and  $p/p_1$  is the ratio of the local wall pressure to the static pressure at the beginning of the pressure rise.

As will be described later in Section 7.3, Bement et al. [59] conducted experiments on a rectangular constant area combustor/inlet isolator duct and concluded that there is good agreement between their experimental results and the predicted pressure distributions by Eq.(1). Also, Nill and Mattick [27] performed experiments of a shock wave reactor for the purpose of chemical processing, and showed that the above relation agrees with their results.

#### 4.3. Neumann and Lustwerk's experiment

Before proceeding to the discussion of the pressure ratio across the pseudo-shock, we shall examine the experimental results by Neumann and Lustwerk [3], because, referring to these results which were also cited in the textbook by Shapiro [6], Crocco [31] mentioned that the pressure rise by the pseudo-shock is almost equal to that of an inviscid normal shock for the same Mach number, but this conclusion does not appear to be correct.

The experimental setup in Ref. [3] consisted of a circular supersonic nozzle with a nominal Mach number of 5, followed by a 50 in long 1 in diameter tube in which wall pressure distribution was measured for different back pressures. Lukasiewicz [5] analyzed the observed results. Assuming a Fanno flow, he calculated the flow Mach number from the pressure distributions. The “Fanno flow” Mach number  $M_F$  is shown in Fig. 8 against the nondimensional distance  $x/D$  from the entrance of the tube. From the figure, it is seen that a great deal of the decrease in Mach number occurs along the tube. After some considerations, he concluded that the measured pressure ratio by the shock compression is in good agreement with the predicted pressure ratio by the normal shock on the basis of  $M_F$ . Note that the value of  $M_F$  represents a mean Mach number over the cross section of the tube and, as a necessity, it is lower than the Mach number  $M_e$  of the main flow outside the boundary layer or at the centerline of the tube, because the velocity profile over the cross section is not uniform.

Hence, the main flow Mach number  $M_e$  was calculated by using the measured wall pressure distributions and assuming an isentropic flow, and then the corresponding boundary layer thickness  $\delta$  was roughly evaluated. The results of  $M_e$  and  $\delta/(D/2)$  are shown against  $x/D$  in Fig. 8. It may be said from the figure that, up to the point of  $x/D$  being about 30, where  $\delta/(D/2)$  is smaller than 0.9, the boundary layer does not fill the tube cross section completely, and the isentropic Mach number  $M_e$  of the main flow may be valid in this range. In that case, since  $M_e$  is larger than  $M_F$ , the measured pressure ratio across the shock region is smaller than the pressure ratio across an inviscid normal shock on the basis of  $M_e$ . From the above consideration, it may be reasonable to conclude that the experimental data in Ref. [3] show lower pressure ratio than that by the normal shock for the same Mach number  $M_e$ .



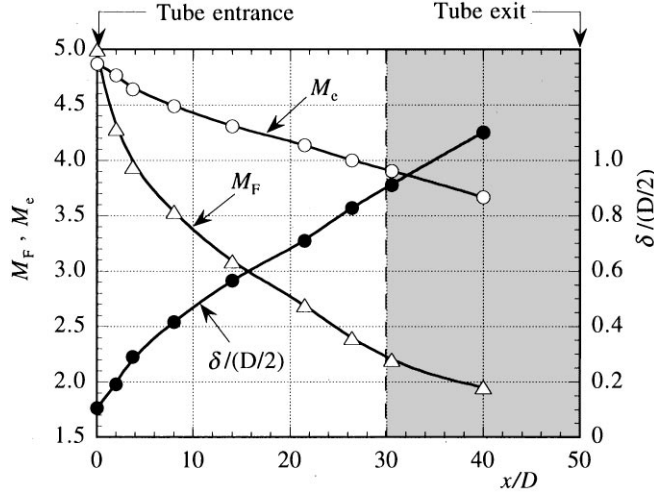


Fig. 8. Mach number and boundary layer thickness along the tube in Neumann and Lustwerk's experiment in Ref. [3].

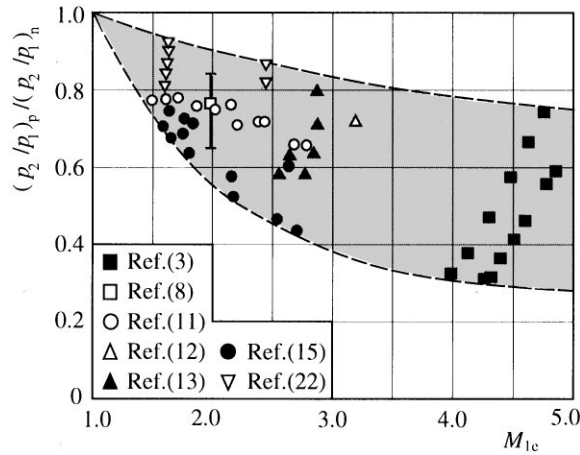


Fig. 9. Static pressure ratio across pseudo-shock normalized by that across normal shock versus freestream Mach number upstream of shock.

#### 4.4. Static pressure ratio across pseudo-shock

In this and the next sections, we consider a duct with a constant area long enough for a maximum point such as the point 2 in Figs. 4 and 6 appearing in the static pressure distributions. In this case, the static pressure ratio across the pseudo-shock can be defined by the ratio of the static pressure at the point 2 to that at the point 1, that is,  $p_2/p_1$ .

In Fig. 9, the measured static pressure ratio across the pseudo-shock,  $(p_2/p_1)_p$ , divided by the theoretical pressure ratio across the normal shock for the same Mach number,  $(p_2/p_1)_n$ , is plotted

against the freestream Mach number just upstream of the shock,  $M_{1e}$ . This figure contains the data obtained from sufficiently long ducts. Some of the data of Ref. [3] corrected on the basis of  $M_{1e}$  by the authors are also shown. The shaded area between two dashed lines denotes the range of scattering data. The experimental data show a great deal of scattering. This is considered mainly due to the fact that the flow confinement effect of the boundary layer is different from experiment to experiment.

Anyway, it can be said from Fig. 9 that the pressure ratio across the pseudo-shock is lower than that of an inviscid normal shock. This tendency becomes more remarkable as the Mach number increases. The reduction in the static pressure rise in comparison with that of the normal shock may be a result from the existence of upstream boundary layer, wall friction, turbulence mixing loss occurring inside the pseudo-shock, etc.

Better correlation may be obtained by considering the flow properties associated with the wall boundary layer, for example, the flow confinement parameter or the Reynolds number based on the boundary layer thickness. This problem will be discussed in Section 6.3. However, it should be said that the effects of these parameters on the pseudo-shock flows are not fully understood so far. Further work is highly needed to obtain full understanding on this ambiguous problem.

#### 4.5. Length of pseudo-shock

The length of the “shock train” can be defined clearly by the length of region where a series of shocks can be visible by optical observations. This definition can be applicable to any internal flow. On the other hand, in case of a long duct with a constant area, the length of “pseudo-shock” can be defined as the distance from the point 1 to the point 2 in Figs. 4 and 6, that is, the distance from the onset of pressure rise to the point where the pressure is maximum. This definition is invalid for flows in various devices such as supersonic diffusers, ejectors, etc., because the flow passages in these devices change from place to place along the flow direction and so, due to the prevailing streamwise pressure gradient, the end point of the pseudo-shock cannot be identified. From the viewpoint of many engineering problems, it may be rather practical to diagnose what is the length necessary to fully achieve the pressure recovery in such a flow. In this section we consider the length of pseudo-shock,  $L_p$ , only in the case of a long straight duct with a constant area.

Fig. 10 shows the relationship between the length of pseudo-shock divided by the equivalent diameter of the duct,  $L_p/D$ , and the freestream Mach number  $M_{1e}$  upstream of the shock. The experimental data were collected from the tests in rectangular and circular ducts long enough. Some of the data of Ref. [3] corrected on the basis of  $M_{1e}$  by the authors are also shown. The solid line represents the values calculated by the “diffusion model” [11] for pseudo-shocks. According to this flow model, which will be described in Section 6.2, the length is given as follows:

$$\frac{L_p}{D} = \frac{2}{c} \sinh^{-1} \left( \frac{w_1 - w_2}{2w^*} \right), \quad (2)$$

where,  $w_1$ ,  $w_2$ , and  $w^*$  are the Crocco numbers at the initial and final sections of the pseudo-shock, and at the sonic condition, respectively, and  $c$  is an empirical constant of 0.114.

Similar to Fig. 9, there is a great deal of scattering in the data in Fig. 10, probably mainly due to different flow confinement effects of the boundary layers. To reduce this scattering, the effect of the flow properties associated with the wall boundary layer on the pseudo-shock length should be

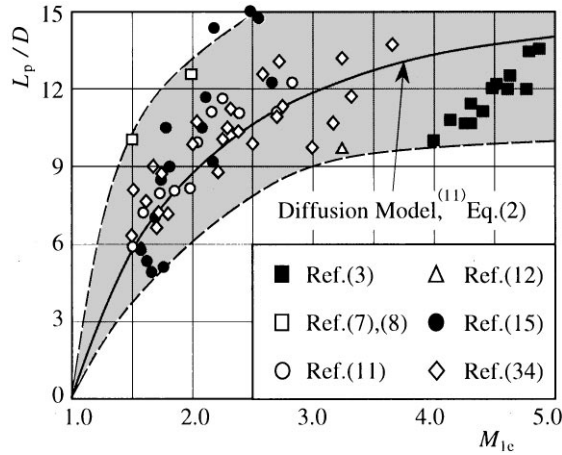


Fig. 10. Non-dimensional pseudo-shock length in constant area duct versus freestream Mach number upstream of shock. So this reference(11) can give us what kind of Diffusion Model (This model is introduced for diffusion of flow velocities between the high and low speed regions at the final section of pseudo-shock) they have used to obtain  $L/D$  ratio w.r.t  $M_{1e}$ .

known. This problem awaits further work. In spite of this scattering, a qualitative explanation can be still made from the figure. The experimental data have a tendency qualitatively similar to the solid curve by Eq. (2), that is, the length of pseudo-shock increases with increase in the upstream Mach number, but it is very likely to approach a nearly constant value for further increase in the Mach number. For the upstream Mach numbers larger than 2, it should be noted that the length of the pseudo-shock extends over 6–15 times the equivalent diameter of the flow passages.

If we apply Eq. (1) to the pressure distribution of the pseudo-shock and replace the pressure  $p$  with the static pressure  $p_2$  at the end of pseudo-shock,  $x$  in Eq. (1) represents the end point of pressure rise, that is, the length of pseudo-shock  $L_p$ . The empirical correlation shows that for a given  $p_2/p_1$ ,  $L_p$  varies inversely with  $(M_1^2 - 1) \text{Re}_\theta^{1/4}$  and directly with  $D^{1/2} \theta_1^{1/2}$ . This relation shows that the pseudo-shock length is a strong function of  $M$  and a weak function of  $\text{Re}_\theta$  and  $D$ .

## 5. Numerical calculations on shock trains

Up to present, a lot of numerical investigations have been presented on the shock/boundary layer interactions. In this section, we will focus our attention to the multiple shock system, namely, the shock train, caused by the normal shock/boundary layer interactions in ducts and review the studies of numerical calculation on the structure of the shock train in the flow passages with a constant area, showing the state of the art of the current understanding on the shock train phenomena. Also, some of the computational results are compared with the experimental results.

### 5.1. Review of previous studies

In the past years, the problem of shock/boundary layer interaction was beyond the reach of numerical simulation. The reason was that the interaction physics was not sufficiently known. For the past four decades, much has been learned from experimental works. With the recent

development of fast and large computer system, it was possible to simulate the interaction phenomenon by numerical calculation. Most of the previous numerical investigations on the shock/boundary layer interactions were focused on external flows [60,61], and reports on the interaction phenomenon in internal flows were very rare.

More recently, some computational efforts have been devoted to the interaction physics in the internal flows. These were, however, restricted to the simple flow fields with a constant area. To our knowledge, there are only a few reports on the shock train phenomena in ducts. Firstly, Hataue [43] computed the shock train phenomena in a constant area duct by using Harten-type second-order TVD scheme based on the two- and three-dimensional Navier–Stokes equations and analyzed the mechanism of bifurcation of the first normal shock in the shock train and the transition process from the normal shock train to the oblique shock train. The calculated pressure distribution in the shock train region is in good qualitative agreement with the experimental data conducted by Tamaki et al. [7]. He also gained an insight into the effects of the upstream Mach number and the upstream boundary layer thickness on the shock/boundary layer interaction.

Lin and his co-workers [38,44] computed the compressible Reynolds-averaged Navier–Stokes equations developed by Chakravarthy et al. [62]. They employed the Baldwin–Lomax zero-equation model for regions with no separation and a backflow turbulence model for regions with separation. Their computation contained the effects of boundary layer thickness and Mach number on the normal shock train, by placing the boundary layer profiles of various momentum thicknesses at the duct entrance and changing the incoming Mach number. The comparison of the pressure rise across the shock train by their computations with Waltrup and Billig correlation shown in Eq. (1) will be discussed in Section 5.3.

Recently, Carroll et al. [45] conducted numerical investigation for multiple shock wave/turbulent boundary layer interactions in the rectangular duct. The computational results for Mach number 1.6, using MacCormack scheme, indicate the inadequacy of Baldwin–Lomax zero-equation turbulence model without further modifications for shock-induced separation. Some improvement was made by applying the Wilcox–Rubesin two-equation turbulence model. However, numerical difficulty was still encountered for the case of higher Mach number flows. Also, Yamane et al. [46] computed the Reynolds-averaged Navier–Stokes equations with the Baldwin–Lomax zero-equation model and investigated the effects of upstream Mach number and upstream boundary layer on the structure of the shock train.

However, great differences are still encountered in comparison with experimental results as will be shown in the next section. Although the computational results mentioned above provided much detailed information on the shock train phenomena, the data obtained by numerical calculations are not sufficient to fully grasp the flow physics with respect to the shock train phenomena. Further studies are needed to get better understanding on such complex flows.

## 5.2. Flow structure in shock train region

Carroll and Dutton [22] performed a detailed experiment on the characteristics of shock trains in a rectangular duct. The series of photographs of their experiment was shown in Fig. 5 in Section 4.1. Carroll et al. [45] conducted a numerical simulation on the shock train structure for the case of freestream Mach number  $M_{1e}$  just upstream of the shock train of 1.61 and the flow confinement parameter  $\delta_1/h$  of 0.32 (as the other conditions, stagnation pressure of  $206 \pm 0.7$  kPa, stagnation

temperature of  $295 \pm 2$  K, unit Reynolds number of  $30 \times 10^6/\text{m}$ , and undisturbed boundary layer thickness of 5.4 mm), and compared the results with the experimental ones just for the same operating conditions in Ref. [22].

An example of their results is reproduced in Fig. 11 [45]. They described in their paper that both computations of the Wilcox–Rubesin two-equation turbulence model and the Baldwin–Lomax algebraic turbulence model failed to properly locate the shock train in the duct, and so the results in Fig. 11 have been shifted to a common origin beginning at the wall static pressure rise.

The Baldwin–Lomax results, as shown in Fig. 11c, capture three shocks in the shock train with the first one bifurcated. However, the Mach number remains supersonic through the first shock. The bifurcation point in the Baldwin–Lomax case is closer to the centerline than in the experiments, possibly contributing to the failure to capture subsonic flow following the normal portion of the first shock. Insufficient streamwise grid resolution may also be a contributing factor. The spacing between the shocks is overpredicted, as is the length of the shock train. The Wilcox–Rubesin case shown in Fig. 11b is better in predicting the global structure of the shock train. This computation captures the first, second, and third shocks in the shock train. The later shocks are very weak. The spacing between shocks nearly matches the experiments. However, similar to the Baldwin–Lomax case, the Wilcox–Rubesin computation locates the bifurcation points too close to the centerline.

Fig. 12 [45] shows another example of their results representing the wall static pressure distributions in the shock train for the same condition ( $M_{1e} = 1.61$ ,  $\delta_1/h = 0.32$ ) as that in Fig. 11.

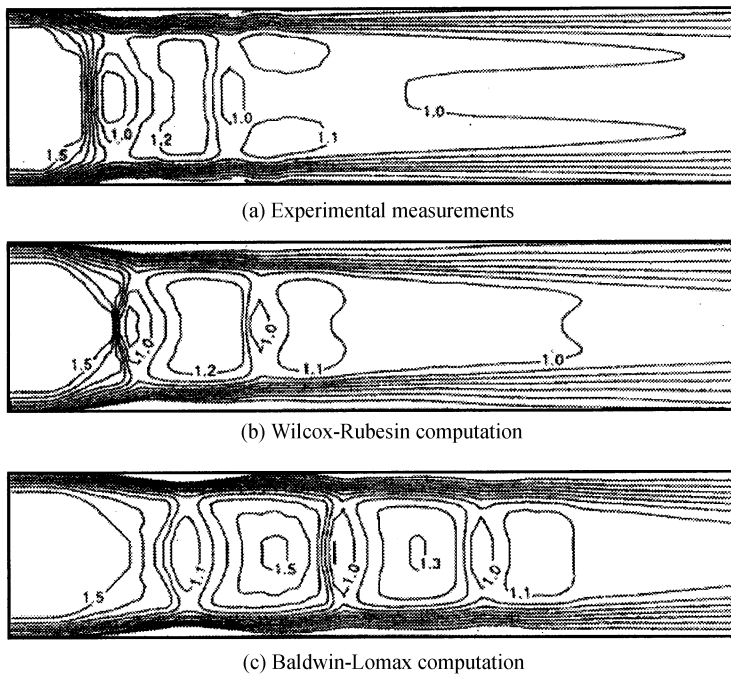


Fig. 11. Mach number contour plots: plot range is 0.4–1.5 in increments of 0.1 ( $M_{1e} = 1.61$ ,  $\delta_1/h = 0.32$ ) [45].

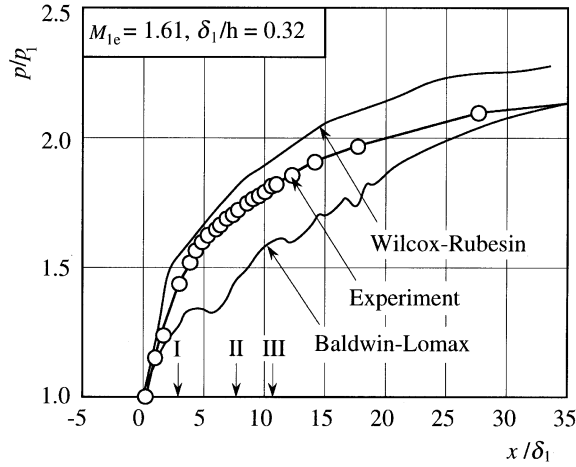


Fig. 12. Wall static pressure distribution, shifted for common initial pressure rise. I, II, and III denote the locations of the first, second, and third shocks, respectively [45].

The horizontal axis denotes the distance  $x$  from the beginning at the pressure rise divided by the boundary layer thickness  $\delta_1$ , and the vertical axis is the local static pressure normalized by the static pressure  $p_1$  just upstream of the shock train. The Wilcox–Rubesin computation shows a more rapid pressure rise than is actually present while the Baldwin–Lomax results have an initially steep pressure rise, then a more gradual downstream pressure increase. The exit pressure imposed in the Wilcox–Rubesin computations is higher than in the experiments. This is done in an effort to properly locate the shock train in the duct. The experimental exit pressure level is used for the Baldwin–Lomax case.

The major conclusion from Fig. 12 is that neither the Wilcox–Rubesin nor the Baldwin–Lomax computations properly predict the magnitude of the wall static pressure rise, even though they do predict the general shape of the pressure rise. This may be resulting partly from the fact that the side wall boundary layers are present in the experiment, but are not modeled in the two-dimensional computations. This is consistent with the overprediction of the pressure in the Wilcox–Rubesin computation, but fails to explain the differences in the Baldwin–Lomax computation.

It should be noted that the computational results by both the turbulence models could not represent the physics of the shock train that reveals in the experiments. The location of the shock train had unreasonably coincided with the experimental result for comparison of both the results. Nevertheless, the computation results show only poor agreement with experiments. It might be the turbulence model that is typically blamed for these discrepancies.

Visbal and Knight [63] evaluated the three different versions of the Baldwin–Lomax turbulence model by a detailed comparison with available experimental data for compression ramp flows over a range of corner angle and Reynolds number. From the results, they concluded that the Baldwin–Lomax turbulence model is found to be unsuitable for separated two-dimensional supersonic interactions due to the unphysical streamwise variation of the computed length scale in the vicinity of separation and to fail to simulate the rapid recovery of the boundary layer downstream of reattachment.



However, in a recent paper, Marshall and Dolling [64] suggested that poor agreement between computation and experiment may not be entirely due to the turbulence model. They presented an interesting comparison between unswept, separated flow compression ramp experiments and computations based on turbulence models ranging from zero-equation schemes to the more recent multi-scale models. It was shown that the agreement with experiment is generally poor irrespective of the turbulence model used. It was demonstrated quite convincingly that low frequency shock unsteadiness controls the distribution of time-averaged surface properties.

The inability of such unsteady effects to be properly captured by conventional turbulence models incorporated into Reynolds-averaged Navier–Stokes simulations may be responsible for discrepancies between computation and experiment. Thus, the unsteady flow physics of the shock wave/turbulent boundary layer interactions, which will be discussed in Section 9, should be understood more completely for simulating the shock train phenomena.

### 5.3. Pressure rise in shock train region

The complex nature of the shock train has prevented the development of a basic theory or an analytical model which predicts the internal characteristics of the flow. However, there are several works which have been successful at predicting overall properties of the shock/boundary layer interactions.

As described in Section 4.2, Waltrup and Billig [9] developed the shock train correlation, Eq. (1), based on their parametric experiments. Lin et al. [38,44] applied Eq. (1) to two-dimensional planar duct with a height of  $H$ , by replacing the diameter  $D$  in Eq. (1) with the height  $H$ , and compared their numerical calculations with Eq. (1). A computational fluid dynamics (CFD) code with TVD scheme for compressible, Reynolds-averaged Navier–Stokes equations, developed by Chakravarthy et al. [62] was used. A hybrid turbulence model developed by Goldberg [65] and Goldberg and Chakravarthy [66] was employed. The model contained the Baldwin–Lomax zero-equation model for regions with no separation and a backflow turbulence model for regions with separation. The computational grid contained  $501 \times 51$  grid points in the duct and  $51 \times 101$  grid points in the open space.

The results are shown in Fig. 13 [38]. As is illustrated at the top of the figure,  $S$  in the horizontal axis represents the distance from the foot of the first shock to the duct exit. The condition at the duct entrance is prescribed by a uniform inflow with or without a boundary-layer profile of designated momentum thickness. Also the subscripts  $i$  and  $1$  show the inflow condition of the duct inlet and the condition just upstream of the shock train, respectively. The vertical axis is the ratio of the back pressure  $p_b$  to the static pressure  $p_1$  at the beginning of the pressure rise. The solid line, calculated from Eq. (1), represents a nondimensional shape for the pressure rise in the shock train at the wall surface. From the figure, in general, the CFD predicted pressure rise curve, in nondimensional form, follows the Waltrup–Billig correlation closely with the exception for the case of  $M_i = 1.8$ . Strictly speaking, it is noted that for most cases the CFD curve is leaning toward the right side of the correlation curve. Physically this means that a planar duct with height the same as a diameter of cylindrical duct is expected to result in longer shock length for the same inflow conditions and back pressure. Hence, as Lin et al. [38] pointed out, investigations on the issue of scaling for various geometries should be necessary.

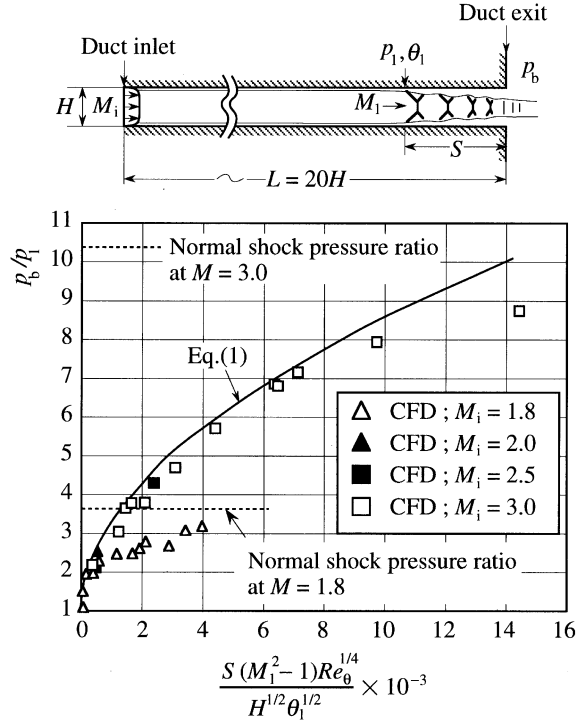


Fig. 13. Comparison of CFD results with Waltrup–Billig correlation given by Eq. (1) (Data reproduced from Ref. [38]).

## 6. Flow models of pseudo-shocks

The pseudo-shock flow is a multi-dimensional viscous compressible flow including a series of successive shocks in its region. Simplifying such a very complicated flow and employing an approximate but simple flow model may be useful for many practical engineering aspects. This section describes some simplified flow models of the pseudo-shock, which will provide better understanding of this phenomenon. In these models, the complex flows are boldly assumed to be one-dimensional, and it should be noted that these models are restricted to constant area ducts.

### 6.1. Shockless model

Crocco [31] first presented a flow model of the pseudo-shock in a duct, which is called “shockless model”. He considered that the total entropy increase due to successive shocks would be negligible compared with that due to a single normal shock. He assumed that the essential dissipative phenomenon for the pseudo-shock does not reside in the shocks but in the turbulence generated in the dissipative region near the wall surface. He made further assumption that in the limit the presence of the shocks may be disregarded entirely and that the main flow in the central core region is uniform and isentropic. Crocco supposed that the nonuniform dissipative region may be

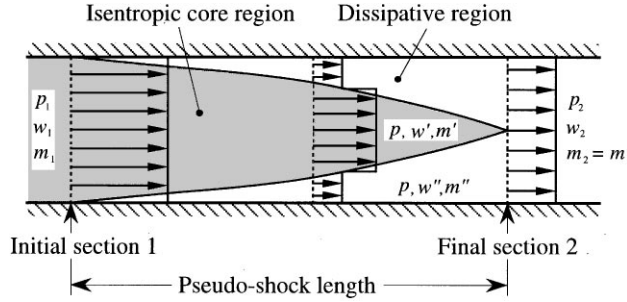


Fig. 14. Shockless model of pseudo-shock by Crocco [31].

approximately treated as an equivalent uniform region. Under this circumstance, appropriate average values were applied to the flow properties.

As the result, as shown in Fig. 14, starting from the initial section 1 (subscript 1) where the flow is still undisturbed and supersonic, the dissipative region spreads through the isentropic core region, until it eventually occupies the whole flow field at the final section 2 (subscript 2), where the flow is subsonic. In the figure,  $m$  is the mass flow rate and  $w$  is the Crocco number which is defined as the flow velocity divided by the limiting velocity (see Notation in the present paper). Crocco number is in proportion to flow velocity if the stagnation temperature of the flow is kept constant. The primed and double-primed quantities refer to the isentropic core region and the dissipative region, respectively. The pressure in the two regions is the same at each section, being designated by  $p$ , and it is given by the following isentropic relation in the central core region:

$$\frac{p}{p_1} = \left( \frac{1 - w'^2}{1 - w_1^2} \right)^{\gamma/(\gamma-1)}, \quad (3)$$

where  $\gamma$  is the ratio of specific heats of gas. The wall friction is assumed negligibly small. Thus, the stagnation enthalpy and stagnation temperature are the same throughout the flow field.

For the flow analysis, it is convenient to introduce the fractional amount of mass flow rate  $\mu \equiv m''/m_1$  for the flow in the dissipative region. Thus  $\mu$  increases from zero at the initial section to unity at the final section. With the given initial condition ( $M_1, p_1$ , etc., at the point 1, and  $\gamma$ ), the flow properties inside the pseudo-shock can be calculated as a function of  $\mu$ , using Eq. (3) together with the conservation equations of mass, momentum, and energy.

An example of numerical calculation of the shockless model for  $M_1 = 3.0$  (that is,  $w_1 = 0.802$ ) and  $\gamma = 1.4$  is shown in Fig. 15, where the Crocco numbers  $w'$  and  $w''$ , and the static pressure rise normalized by the pressure difference across the shock,  $(p - p_1)/(p_2 - p_1)$ , are plotted against  $\mu$ . The horizontal dotted line denotes the sonic value of Crocco number  $w^* = 0.408$ . As is evident from the figure, according to this model, the flow in the isentropic core region gradually decelerates while the flow in the dissipative region accelerates due to the mixing effect of the two regions, but both the velocities do not coincide at the final section, where  $w'$  is still supersonic and  $w''$  is subsonic. The static pressure gradually increases with increase in  $\mu$ .

This very simple model reveals the essential characteristics of the pseudo-shock. However it should be pointed out that, if the growing rate of the dissipative region spreading into the

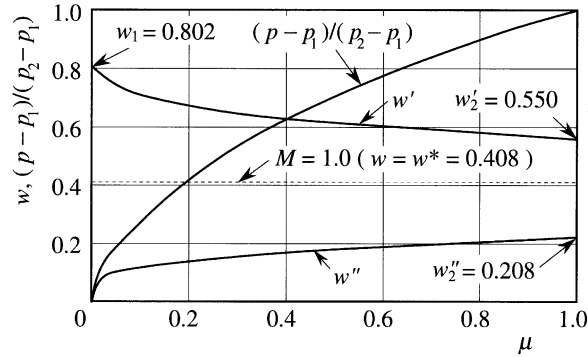


Fig. 15. Calculation results by shockless model. Crocco number and static pressure against the fractional amount of dissipative flow for initial Mach number  $M_1 = 3.0$  and  $\gamma = 1.4$ .

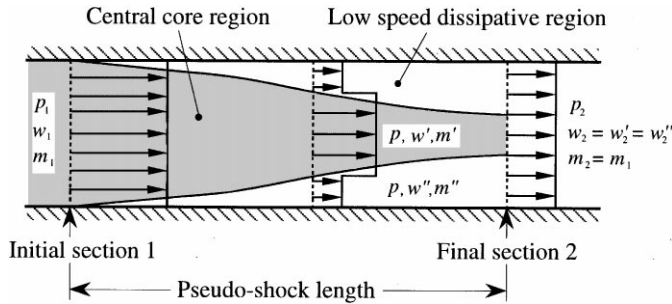


Fig. 16. Diffusion model of pseudo-shock [11].

isentropic core is given, the fractional mass flow rate  $\mu$  could be related to the axial distance along the duct so that the pressure distribution can be calculated, but this model provides no information about it. Another point is that, since this model assumes uniform flows at both upstream and downstream of the shock and no boundary layer is present, the flow properties at the final section (for example,  $w_2' = 0.208$  at  $\mu = 1.0$  in Fig. 15) are exactly the same as those given by a single normal shock.

### 6.2. Diffusion model

Ikui et al. [11] made some improvement for Crocco's shockless model. They considered that the high-speed uniform flow in the central core region of a duct is not isentropic and the mass flow rate in the central core does not vanish even at the final section of the pseudo-shock, as shown in Fig. 16. The final section was defined as the point where the velocity in the central core region which decreases with distance becomes equal to the velocity in the lower speed dissipative region near the wall which increases with distance.

Similar to the shockless model, the assumptions for supersonic and subsonic uniform flows were applied at the initial and final sections, respectively. It was assumed that, inside the pseudo-shock,

the high speed flow at the central region and the lower speed flow near the wall surface are diffused together, eventually resulting in the subsonic uniform flow at the final section, and that the streamwise velocity variation in the two regions is expressed by the following relations:

$$\frac{dw'}{dx} = -cw', \quad (4)$$

$$\frac{dw'}{dx} + B \frac{dw''}{dx} = 0. \quad (5)$$

Eq. (4) represents the velocity variation in the central core region, and  $c$  is the coefficient of the velocity decay, which was determined experimentally by 0.114 in Ref. [11]. Eq. (5) combines the streamwise velocity variation in the central region with the lower velocity flow close to the wall, and the coefficient  $B$  is derived from the boundary conditions at the initial and final sections of the pseudo-shock.

Combining the above two equations with the conservation equations of mass, momentum, and energy, the flow properties within the pseudo-shock can be calculated. The static pressure within the pseudo-shock is given by

$$\frac{p - p_1}{p_2 - p_1} = \frac{\{w_1^2(w_1^2 - 2w^{*2}) + w_1^2w^{*2}e^{-c(x/D)}\}(1 - e^{-c(x/D)})}{(w_1^2 - w^{*2})^2 - w_1^2(w_1^2 - w^{*2})e^{-c(x/D)}(1 - e^{-c(x/D)})}, \quad (6)$$

where  $x$  is the distance from the initial section of the pseudo-shock and  $D$  is the equivalent diameter of the duct. The length of the pseudo-shock by this model is expressed by Eq. (2), as described in Section 4.5. They called the above flow model “diffusion model”. This model does not attempt to predict the exact pseudo-shock structure, but rather assumes that the flow smoothly reaches the final subsonic state.

Since Eq. (6) does not contain boundary layer parameters, in comparison with Eq. (1) given by Waltrup and Billig [9], it is easy to calculate the pressure distribution within the pseudo-shock. It should be noted that, similar to the shockless model, this model gives the same flow properties at the final section of the pseudo-shock as those predicted by a single normal shock, since the wall friction inside the pseudo-shock is not involved and the flow is assumed to be uniform at both upstream and downstream of the shock.

Fig. 17 shows an example of calculation by the diffusion model for the same flow conditions ( $M_1 = 3.0$ ,  $\gamma = 1.4$ ) as those in Fig. 15, where the Crocco numbers  $w'$  and  $w''$ , the normalized pressure rise  $(p - p_1)/(p_2 - p_1)$ , and the fractional mass flow rate  $\mu$  are plotted against the nondimensional distance  $x/D$  from the initial section of the pseudo-shock. The Crocco number  $w'$  reduces exponentially along the flow direction, and it agrees with the Crocco number  $w''$  at the final section of the pseudo-shock ( $w'_2 = w''_2 = 0.208$ ). In this case the length of pseudo-shock is about  $11.9D$ . The static pressure rises rather steeply in the front region and more gradually in the rear region. The fractional mass flow rate  $\mu$  increases from zero at  $x/D = 0$  to about 0.74 at the final section.

Fig. 18 [11] shows a comparison of the experimental results of wall static pressure distributions in the pseudo-shocks with the calculated values by the diffusion model. The horizontal axis is the nondimensional distance from the initial section of the pseudo-shock,  $x/D$ , and the vertical axis is

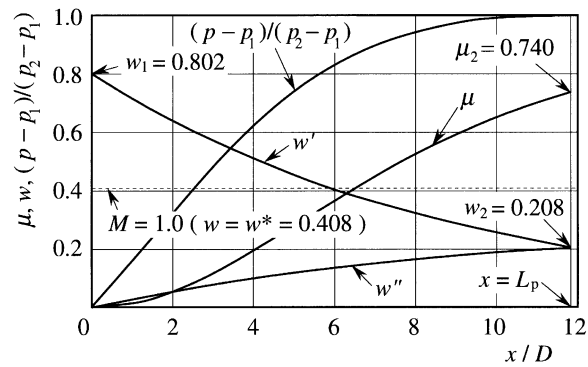


Fig. 17. Calculation results by diffusion model. Crocco number, static pressure, and fractional amount of low speed dissipative region against the distance from initial section of pseudo-shock for initial Mach number  $M_1 = 3.0$  and  $\gamma = 1.4$ .

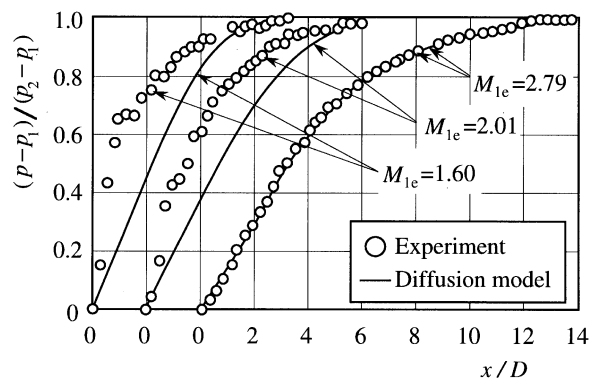


Fig. 18. Wall static pressure distributions in pseudo-shocks by experiment and by diffusion model [11] (Note: each curve displaced 2 to right of previous one).

the pressure rise  $p - p_1$  normalized by the pressure difference across the pseudo-shock  $p_2 - p_1$ . The parameter  $M_{1e}$  in the figure represents the freestream Mach number just upstream of the shock. Good agreement is obtained for high Mach numbers but not for lower Mach numbers. The reason is that a supersonic flow with a low Mach number is not fully diffused within the distance, leading to significant deviation from the assumptions of the uniform flows both at upstream and downstream of the pseudo-shock.

Nill and Mattick [27] conducted an experiment of shock/boundary layer interactions on a constant area duct to investigate the effect of this highly dissipative process on the performance of the shock wave reactor for chemical processing. They compared their experimental results with values calculated by Eq. (6), and showed that a steeper pressure rise is observed at the beginning of the pseudo-shock, but it is in general close to the theoretical curve.



### 6.3. Modified diffusion model

The two models mentioned above neglect the effect of upstream boundary layer and wall friction in the pseudo-shock region. Therefore, the pressure rise across the pseudo-shock by these models is equal to the Rankine–Hugoniot value, but they are different in general from the previous experimental data, as was pointed out in Section 4.4. Ikui et al. [15] revised their early diffusion model by taking account of the upstream boundary layer at the initial section as well as the wall friction inside the pseudo-shock. Therefore, by this model, the static and total pressure ratios across the pseudo-shock depend not only in upstream Mach number but also on upstream boundary layer and wall friction.

An empirical relation of the pseudo-shock length which they derived from previous and their own experimental results was incorporated into their “modified diffusion model”. A conceptual schematic sketch of the modified diffusion model is shown in Fig. 19. At the initial section, two mean flows of the supersonic flow in the central core region and the subsonic flow near the wall were assumed. Therefore the fractional mass flow rate  $\mu_1$  at the initial section is not zero but a positive value less than unity. The different points of this model from the previous two models are summarized in Table 2.

The experiment in Ref. [15] was performed in constant area rectangular ducts, and the duct height was varied to investigate the effect of the boundary layer thickness  $\delta_1$  upstream of the shock on the pseudo-shock structure. The experimental results are compared with the calculated results

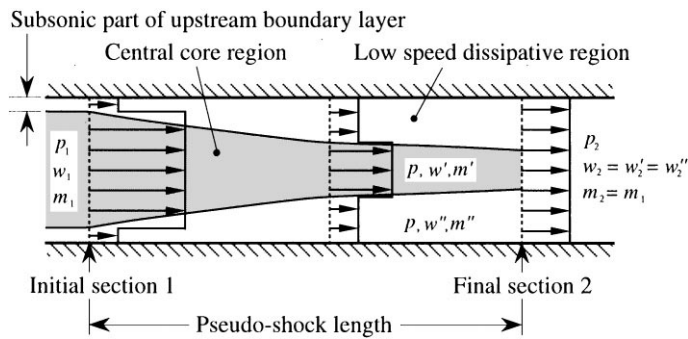


Fig. 19. Modified diffusion model of pseudo-shock [15].

Table 2  
One-dimensional flow model of pseudo-shock in straight flow duct

Year	Model	Velocity profile and $\mu$ at inlet	Inside of pseudo-shock region	Velocity profile and $\mu$ at exit	Ref.
1958	Shockless model	Uniform $\mu_1 = 0$	No friction	Uniform $\mu_2 = 1$	[31]
1973	Diffusion model	Uniform $\mu_1 = 0$	No friction	Uniform $0 < \mu_2 < 1$	[11]
1981	Modified diffusion model	1/7 power profile $0 < \mu_1 < 1$	Wall friction considered	Uniform $\mu_1 < \mu_2 < 1$	[15]

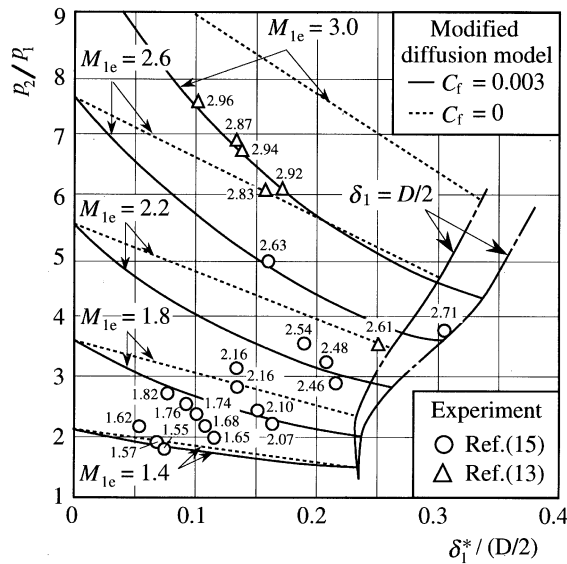


Fig. 20. Comparison of experiment and calculation using modified diffusion model [15].

by the modified diffusion model in Fig. 20, where the horizontal axis represents the ratio of the upstream boundary layer displacement thickness to the equivalent radius of the ducts, and the vertical axis the pressure ratio across the pseudo-shock. The dotted and solid lines indicate the calculation results for the coefficients of wall friction of  $C_f = 0$  (no friction) and  $C_f = 0.003$ , respectively. The two dash-dotted lines at the right end of these dotted and solid lines represent the border lines where  $\delta_1 = D/2$ , that is, the boundary layer is considered to fill the duct cross section completely. Therefore, on the left side of this line, there exists a freestream outside of the boundary layer, but not on the right side. The figures shown in each line and in each experimental point indicate the freestream Mach number  $M_{1e}$ . Note that the values of  $p_2/p_1$  for  $\delta_1^*/(D/2) = 0$  on the vertical axis correspond to the theoretical values by Rankine–Hugoniot equation.

It can be said from Fig. 20 that the static pressure ratio across the pseudo-shock reduces as the boundary layer displacement thickness increases for each Mach number. Such a tendency becomes more remarkable for higher Mach number. It should be noted that good agreement of the analytical results with the experiment is obtained if the wall friction is considered. Especially the agreement seem to be better for a high Mach number. In practice, there is likely to be large separation region inside the pseudo-shock with such a high Mach number [9,22]. Under this situation, the coefficient of wall friction may be negligible or may have a negative value. The existing data regarding the wall friction inside the pseudo-shock is, at present, very insufficient to resolve this conflict.

6.4. Other flow models

In addition to the flow models mentioned above, some other flow models with regard to pseudo-shocks have been proposed by some researchers. For example, Zimont and Ostras

presented the jet-flow model [49]. They analyzed the case of a developed pseudo-shock which occurs at fairly thick boundary layers, where the entropy increase in a system of X-shaped shocks (at the freestream Mach number  $M_{1e}$  just upstream of the pseudo-shock larger than about 2.0) can be neglected. In this case the flow upstream of the pseudo-shock is rapidly smeared out because of viscous friction and the cross-sectional velocity distributions exhibit a smooth bell shape.

Therefore, Zimont and Ostras assumed that the development of the dissipation zone inside the pseudo-shock is of jet-like nature and obeys the laws governing the behavior of a submerged supersonic jet. Also, they considered that the existence of frictional forces at the wall has significant effect on the flow properties at the end of the pseudo-shock. Furthermore, considering the constant total temperature through the pseudo-shock and negligible transverse pressure gradient at any cross-section in addition to the above assumptions, they derived two independent integral equations with respect to the flow velocity and the static pressure from the conservation of the mass and momentum. However, the equations contain the terms of Bessel function in the integrand. Because of implicitity and complexity, the calculation is not straightforward and further simplification is needed for a practical use.

Fig. 21 shows the comparison of Zimont and Ostras' experimental data [49] on the pressure distributions along the wall in the pseudo-shock region with those calculated from their jet-flow model, with a schematic illustration of their experimental apparatus. In the experiment, the static pressures were measured on the cylindrical duct with an internal diameter of  $D = 81.4$  mm and the Mach number  $M_i$  at the inlet of the test section was 3.2. The distance  $X$  from the inlet of the test section to the onset point of the pressure rise due to the shock train could be adjusted in the range from  $4D$  to  $7D$ , by means of the throttle located downstream of the test section.

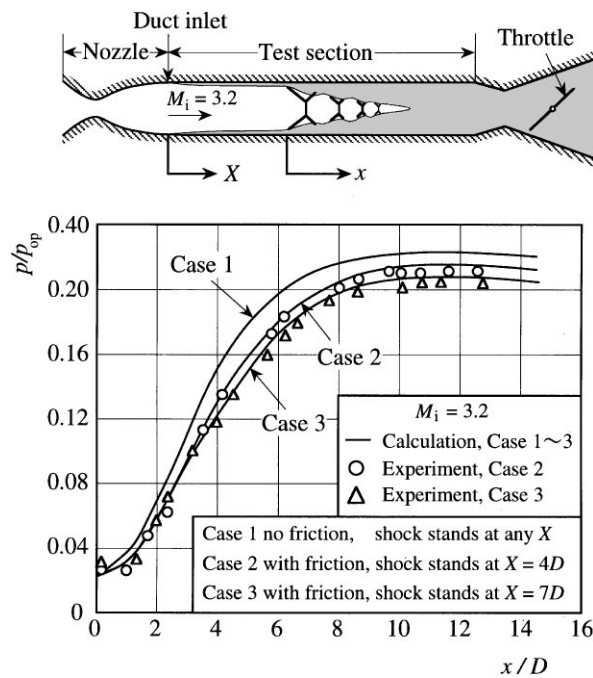


Fig. 21. Wall static pressure distributions in pseudo-shocks by experiment and by jet flow model [49].

The horizontal axis in Fig. 21 represents the nondimensional distance  $x/D$  streamwise from the point of initial pressure rise and the vertical axis is the ratio of the local wall static pressure  $p$  to the stagnation pressure  $p_{op}$  upstream of the nozzle. Case 1 represents the calculated results without friction. Cases 2 and 3 show the calculated or experimental results with friction for  $X/D = 4$  and 7, respectively. Each calculated static pressure rises gradually through the pseudo-shock region and reaches the maximum value at the end ( $x/D =$  about 11) of the pseudo-shock. As the distance  $X/D$  increases, the calculated static pressure rise across the pseudo-shock becomes smaller. This tendency quantitatively agrees well with the experimental results.

Shchetinkov proposed another analytical flow model for the pseudo-shock. Fig. 22a illustrates his separation model [50], where  $h$  and  $h_s$  indicate the half-height of a duct and the height of the separation region, respectively. He assumed that the flow velocity in the separation region, the transverse pressure gradient at any cross-section and the variation of total temperature through the pseudo-shock region are negligible and derived the relationship for the  $h_s/h$  and the Mach number  $M$  inside the pseudo-shock from the conservation laws of mass and momentum.

The separation model can obtain the distributions of the  $M$  and  $h_s/h$  inside the pseudo-shock if the wall pressure distribution in the pseudo-shock region and the initial Mach number  $M_1$  just upstream of the pseudo-shock are known in advance from experiment or any other means. That is, this model predicts only the approximate configuration of the separation region, by means of the known values of the streamwise static pressure inside the pseudo-shock and the initial Mach number.

Fig. 22b, which was reproduced from Ref. [50], shows the streamwise distribution of  $h_s/h$  calculated from the separation model by using the experimentally obtained wall static pressure distribution which is shown as a solid line in the figure and was obtained by Tamaki et al. [8]. The test section in Ref. [8] consisted of a rectangular duct surrounded by two flat plates having a slightly divergent angle so as to make the pseudo-shock stable. The height of the duct was  $2h = 40$  mm at the leading edge of the plates and the width between the side plates was 30 mm. The length of the test section was 1200 mm. Both of the top and bottom plates were sloped 1 mm per 200 mm from the center line, forming a slightly divergent duct. The duct was connected to a supersonic nozzle with freestream Mach number  $M_{1e} = 1.99$  at the duct inlet.

In Fig. 22b, the horizontal axis denotes the streamwise distance  $x$  from the onset point of the pressure rise and the vertical axis is the ratio of the local wall pressure  $p$  to the upstream stagnation

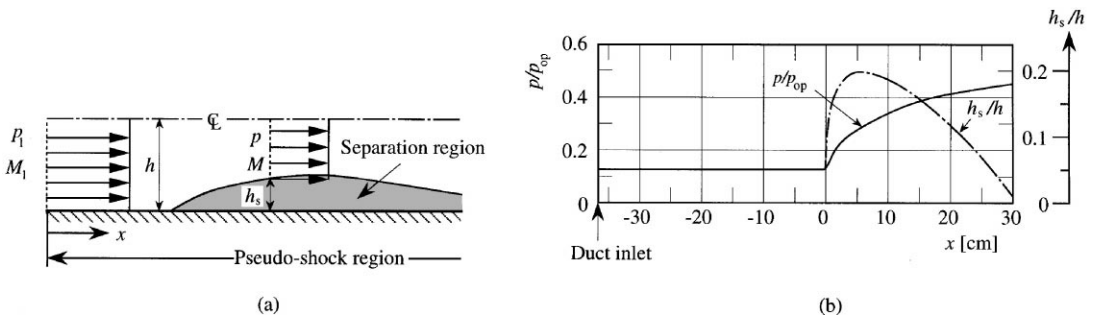


Fig. 22. Calculation of separation region in pseudo-shock by separation model [50]. (a) Separation model of pseudo-shock. (b) Experimental total and wall static pressure distributions and calculated separation height.

pressure  $p_{op}$ . The  $h_s/h$  increases rapidly near the onset point of the pressure rise, reaches the maximum at  $x =$  about 5 cm, and then decreases gradually with increasing distance  $x$ . Finally, the  $h_s/h$  seems to have a negative value in the range of  $x$  greater than 30 cm.

Recently, Nagai and Yaga [51] conceived that the velocity profiles at the initial and final sections of the pseudo-shock would be self-similar to each other. Neglecting the wall friction and heat transfer inside the pseudo-shock, they derived the relationships across the pseudo-shock. According to their analytical results, for a given freestream Mach number just upstream of the pseudo-shock, the ratio of the total pressure at the final section to that at the initial section of the pseudo-shock increases as the boundary layer thickness at the initial section increases. This result is not supported by any experiment made previously [8,15].

More recently, Matsuo et al. presented the mass-averaging pseudo-shock model [52] by considering the proper mean properties over a cross-sectional area at initial and final sections of the pseudo-shock. Their model neglects both the wall friction and the heat transfer inside the pseudo-shock and can obtain the flow properties across the pseudo-shock by the explicit relations. For a higher incoming Mach number, the analytical results agree quantitatively well with the experimental results. However, the flow characteristics inside the pseudo-shock cannot be calculated by using this flow model.

In contrast to one-dimensional flow model described above, Tamaki et al. proposed the shock reflection model [8]. The flow properties in the pseudo-shock can be calculated using the oblique shock relations with the shock angles obtained from optical observation. However, this model needs to know in advance the shock angles of a series of shocks in the shock train.

Up to this point, we have discussed the pseudo-shock which stands steadily in the flow passages with a constant area of the simplest configuration that is rarely encountered in many engineering practices. Nevertheless, the current understanding on this phenomenon is not sufficient. No flow model mentioned previously could properly predict the flow characteristics of the pseudo-shock with a good accuracy. This is mainly due to poor understanding on the physics of the shock train and the pseudo-shock. More sophisticated flow model is highly needed for reasonable prediction of the pseudo-shock, for example involving the transverse pressure gradient, heat transfer and the flow unsteadiness, if necessary. We may need two or three-dimensional flow models, if we want to make more accurate prediction of the pseudo-shock in internal flow systems.

## 7. Pseudo-shocks in flow devices

In the previous sections, we described the results of experimental, numerical, and analytical investigations of the shock train and pseudo-shock phenomena in constant area ducts. These phenomena commonly occur in confined, internal, supersonic flows where normal shocks are supposed to stand and interact with wall boundary layers. Examples include supersonic wind tunnel diffusers, supersonic ramjet or scramjet inlets, and supersonic gas ejectors. This section deals with the pseudo-shock phenomena in such flow devices.

Generally, the cross-sectional area of flow in various devices changes along the flow direction. The variation of cross-sectional area would have no effect on a normal shock structure because of its extremely thin thickness. On the other hand, the pseudo-shock structure is significantly affected by the area change, because its length extends over a great distance along the passage. For example,

even to determine the pseudo-shock length in a straight divergent channel is very complicated [67]. Hence the description in this section may be rather qualitative.

### 7.1. Supersonic wind tunnel diffusers

A supersonic wind tunnel diffuser decelerates the supersonic flow in the test section to low subsonic speeds. The wind tunnel performance is characterized by the overall pressure ratio of the plenum pressure  $p_{op}$  to the pressure  $p_{oe}$  at the diffuser exit where the static pressure may be equal to the total pressure because of low subsonic velocity. A lower overall pressure ratio is desirable for the economical wind tunnel operation. For the reason, as shown in Fig. 23, a supersonic diffuser with contraction is used. The diffuser throat, which is also called the second throat, must be larger than the nozzle throat.

The simple one-dimensional theory assuming a normal shock and no boundary layer is given in various textbooks on gas dynamics, for example, Liepmann and Roshko [68]. According to this inviscid theory, the second throat area  $A_2$  must be large enough to accommodate the mass flow when there is a normal shock in the test section. The minimum permissible area of the second throat  $A_{2min}$  and the minimum overall pressure ratio needed for starting the wind tunnel,  $(p_{op}/p_{oe})_{min}$ , are given by the following equations, respectively:

$$\frac{A_{2min}}{A_t} = \frac{A_{2min}}{A_1^*} \frac{A_1^*}{A_t} = \frac{p_{op}}{p_{oe}} \frac{A_1^*}{A_t} = \left[ \frac{(\gamma - 1)M_t^2 + 2}{(\gamma + 1)M_t^2} \right]^{1/2} \left[ \frac{2\gamma M_t^2 - (\gamma - 1)}{(\gamma + 1)M_t^2} \right]^{1/(\gamma - 1)}, \quad (7)$$

$$\left( \frac{p_{op}}{p_{oe}} \right)_{min} = \left[ \frac{(\gamma - 1)M_t^2 + 2}{(\gamma + 1)M_t^2} \right]^{\gamma/(\gamma - 1)} \left[ \frac{2\gamma M_t^2 - (\gamma - 1)}{\gamma + 1} \right]^{1/(\gamma - 1)}, \quad (8)$$

where  $A_t$  and  $M_t$  are the cross-sectional area and the flow Mach number of the test section, respectively, and  $A_1^*$  is the cross-sectional area of the nozzle throat.

When the overall pressure ratio increases gradually and attains to the value of Eq. (8), a normal shock stands in the test section, and as soon as the pressure ratio exceeds by a small amount, the shock passes through the second throat, and takes up a position in the diffuser where the area is equal to the test section area. Thus the tunnel starts. For the second throat area larger than  $A_{2min}$ , the minimum overall pressure ratio needed for starting is independent of the second throat area, as

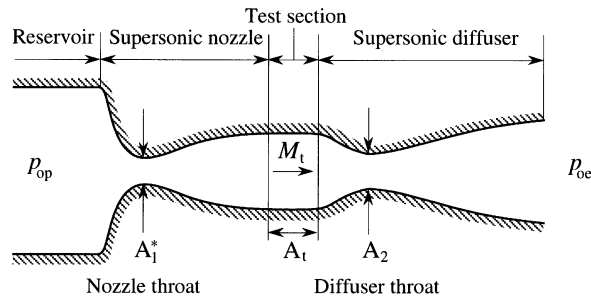


Fig. 23. Geometry of supersonic wind tunnel.



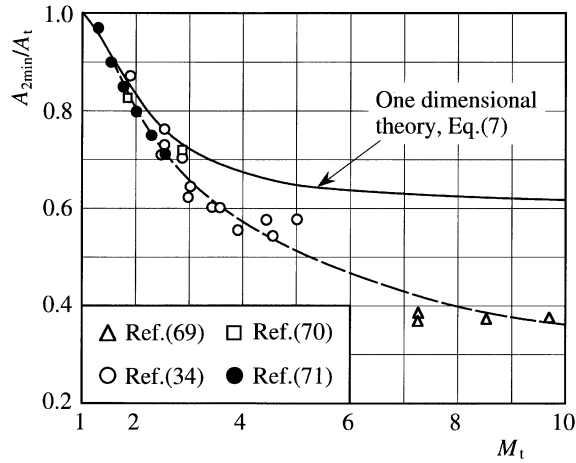


Fig. 24. Minimum area of the second throat for starting supersonic wind tunnel.

is seen from Eq. (8). However the previous experiments [69,70] show that it depends not only the Mach number  $M_t$  but also the area ratio  $A_2/A_1^*$ .

Previous experimental results [34, 69–71] of the minimum permissible area of the second throat  $A_{2min}$  are shown against the test section Mach number in Fig. 24, together with the calculated results by Eq. (7). The dashed line denotes the fitting curve of the experimental points. It can be clearly seen that for lower Mach numbers the agreement between the theory and experiment is fairly good, but for higher Mach numbers, the experimental data are smaller than the theoretical values, and the difference increases with the Mach number.

The reason is evident [70]. In the theory, deceleration of the supersonic flow takes place in a single normal shock. The ratio  $p_{op}/p_{oe}$  in Eq. (7) indicates the ratio of the total pressure upstream of the shock which is standing at the test section to the total pressure at the second throat, and so this ratio is given in the theory as the total pressure ratio across a normal shock with a Mach number of  $M_t$ . In reality, the deceleration is done by the pseudo-shock with a certain length scale. Then the total pressure loss between the test section and the second throat, which determines the value of  $p_{op}/p_{oe}$  in Eq. (7), depends on not only the Mach number  $M_t$  but also the correlation between the pseudo-shock length and the length from the test section to the second throat of the diffuser. The latter length is usually short in comparison with the former length. In such cases, the ratio  $p_{op}/p_{oe}$  and so the value of  $A_{2min}/A_t$  in Eq. (7) is smaller than those predicted by a single normal shock.

The starting problem of the supersonic wind tunnel is closely dependent on the geometry of the second throat of the supersonic diffuser. The process is discussed on the basis of the pseudo-shock concept in Ref. [72]. It should be added that pressure recovery in supersonic diffusers up to the Mach number of 26 is shown in Ref. [73]. Improvement of a supersonic wind tunnel performance is achieved by reducing the starting and operating overall pressure ratio. Therefore, the pseudo-shock phenomenon should be understood more clearly for better design of the wind tunnel.

7.2. Supersonic inlet diffusers

During operation in the supersonic velocity regime, air-breathing jet engines require an inlet which reduces the supersonic flow velocity to low subsonic and provides for the highest pressure recovery with a minimum stagnation pressure loss. Under the situation of a started inlet, the overall compression process in the supersonic inlet (or intake) diffuser is made in three stages, that is, supersonic compression (velocity deceleration and static pressure recovery) by compression waves and oblique shocks, deceleration with a “normal shock” from supersonic to subsonic, and the subsequent subsonic compression. The “normal shock” mentioned above in the supersonic inlet diffuser is usually called a terminal shock.

The performance and stability of the supersonic inlet is strongly affected by the structure of the terminal shock and its location. The simplest realization of the terminal shock is a single normal shock. But such a simple pattern rarely occurs in reality. The boundary layer on the wall surface of the inlet interacts with the shock, creating a shock train and a pseudo-shock for a higher Mach number. Many experimental [39,74], and computational [75,76] investigations have been reported so far on the terminal shock, and a comprehensive review is given by Hamed and Shang [77] on the shock/boundary layer interactions that is pertinent to the flow prediction in supersonic inlets. In this section, we describe the supersonic inlet flows from the viewpoint of pseudo-shocks briefly.

Typical terminal shock patterns presented by Sajben et al. [39] are shown in Fig. 25, where  $M_\infty$  and  $M_{1e}$  represent the freestream Mach number and the Mach number immediately upstream of the terminal shock, respectively. The range of interest of  $M_\infty$  is from 2.5 to 6, and  $M_{1e}$  is assumed to vary up to 3. For  $M_{1e}$  smaller than 1.3, the structure is a single normal shock, showing some curvature near the walls. Above this value, shock-induced separation occurs and the shock develops bifurcation patterns. For  $M_{1e}$  above 1.6, a normal or oblique shock train appears. The above classification is very similar to that in the constant area ducts shown in Fig. 1.

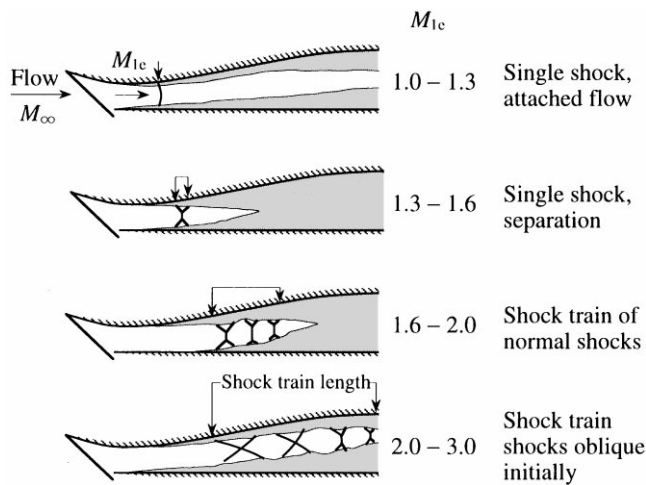


Fig. 25. Typical terminal shock patterns. Mach number ( $M_{1e}$ ) ranges given are approximate; actual values are configuration dependent [39].

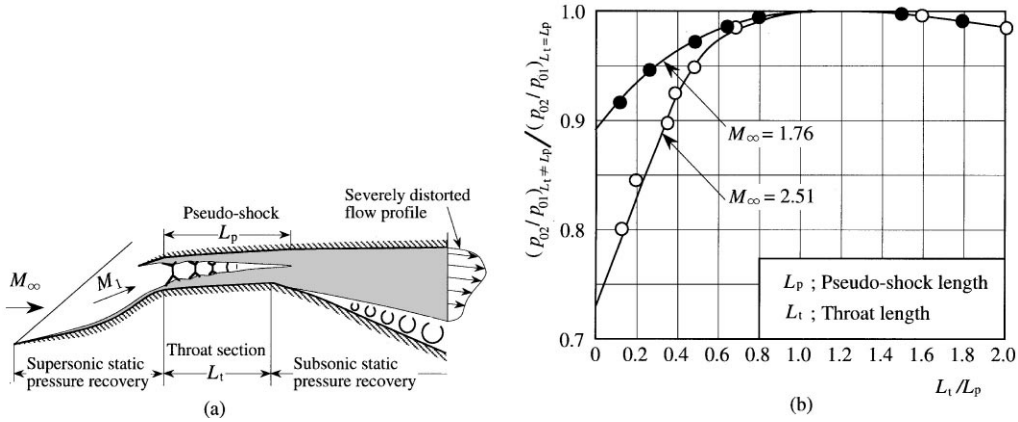


Fig. 26. Pseudo-shock in supersonic inlet diffuser and relation between throat length and total pressure recovery (original figures from Ref. [78]). (a) Schematic of shock train with separation in supersonic inlet diffuser. (b) Effect of throat length on inlet total pressure recovery.

Mahoney [78] showed very clearly the effect of the pseudo-shock length on the total pressure recovery in the supersonic inlet. As shown in Fig. 26a, the freestream Mach number  $M_\infty$  is reduced to the Mach number  $M_1$  through the supersonic static pressure recovery region, and then the transition from supersonic to subsonic flow occurs across a “normal shock” that stands in the minimum area, or throat, under normal design operating conditions. The normal shock interacts with the boundary layers along the walls to form a pseudo-shock. The results is a substantial reduction in the total pressure recovery and a severely distorted flow profile that can degrade combustion efficiency.

A solution to the problem is that the throat of the inlet is stretched to contain the entire pseudo-shock. The effect of changes in throat length  $L_t$  relative to pseudo-shock length  $L_p$  is shown in Fig. 26b. If  $L_t$  is equal to  $L_p$ , then the total pressure recovery,  $p_{02}/p_{01}$ , of the compression process is the maximum attainable with the inlet configuration. If  $L_t$  is longer than  $L_p$ , there are additional viscous losses, but the overall total pressure recovery decreases only gradually with increasing throat length. If  $L_t$  is shorter than  $L_p$ , the total pressure recovery decreases with decreasing throat length, and the recovery loss is much greater at a higher Mach number of  $M_\infty = 2.51$  than at a lower Mach number of  $M_\infty = 1.76$ .

From the results mentioned above, Mahoney concluded as follows: At any design Mach number, the total pressure recovery of a supersonic inlet is sensitive to throat section design. For throat lengths equal to or slightly greater than the pseudo-shock length, the recovery is the maximum attainable. In order to incorporate the proper length throat in any inlet, the designer must know the length of the pseudo-shock and parameters that control the pseudo-shock length.

### 7.3. Inlet/combustor isolators

During the past two decades, a significant progress has been brought toward the realization of air-breathing supersonic combustion ramjets (called scramjets, briefly). The scramjet has the

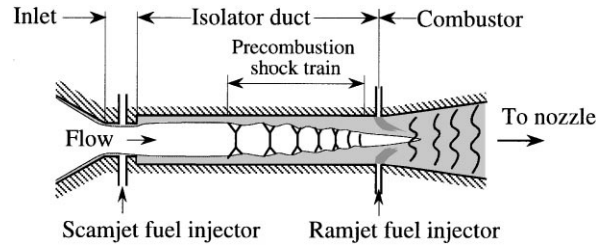


Fig. 27. Schematic illustration of dual-mode ramjet/scramjet combustor.

potential to operate efficiently at very high Mach numbers. Any air-breathing flight vehicle operating at hypersonic speeds will require a combined cycle engine which operates efficiently from low subsonic to supersonic speed range. From this point, the dual-mode engine concept was proposed by Curran and Stull in 1964 [79].

A schematic illustration of the dual-mode ramjet/scramjet combustor is shown in Fig. 27. When operating in the ramjet mode, the air leaves the inlet at supersonic speeds in the case of absence of combustion. However, the combustion in the combustor creates a back pressure which requires a shock to form ahead of the combustor. **The shock is required to be of sufficient strength to decelerate the supersonic flow from the inlet to subsonic at the combustor entry for a conventional subsonic burning.** This shock is usually referred to as the precombustion shock [36,58,79]. Stabilizing the precombustion shock and isolating it from the inlet is imperative to avoid an inlet unstart and a significant loss in thrust. For this purpose, **a constant area duct is placed between the inlet and the combustor.** This duct is called an **isolator duct** and its key function is to prevent the **static pressure rise associated with combustor operation from unstating the inlet.**

When the dual-mode engine system shown in Fig. 27 is operating in the scramjet mode, the flow through the engine is supersonic everywhere and it would appear that there is no need for an isolator duct. However, the rate of area increase in the combustor is frequently insufficient to relieve thermal choking from heat addition to the supersonic stream, and an adverse pressure gradient arises [79]. Hence, as shown in the figure, the scramjet fuel injector is installed at the upstream end of the isolator and the duct is used as a constant area combustor for the higher speeds [40].

In the ramjet mode, the precombustion shock in the isolator duct interacts with the wall boundary layers to form a pseudo-shock if the duct is long enough. As was shown in Fig. 10, the pseudo-shock has a substantial length. It is unrealistic to design such a long isolator duct. Therefore a pressure rise much less than a normal shock is achieved by the precombustion shock train. The precombustion shock train in the isolator duct has been investigated experimentally [40,58,59] and numerically [37,38,44] by many researchers.

One of the results is represented in Fig. 28. This shows the static pressure distributions on the wall surface of the generic high-speed engine model in the experiment by Bement et al. [59] This model consists of an inlet, sidewall ramps, an isolator, and a combustor. In this experiment, a flow with a Mach number of 3.4 enters the inlet which is designed to compress the captured air flow to Mach 2.6. Additional internal compression is provided by the following sidewall ramps. The actual Mach number at the isolator entrance was 1.94 in the experiment in Fig. 28. The constant area

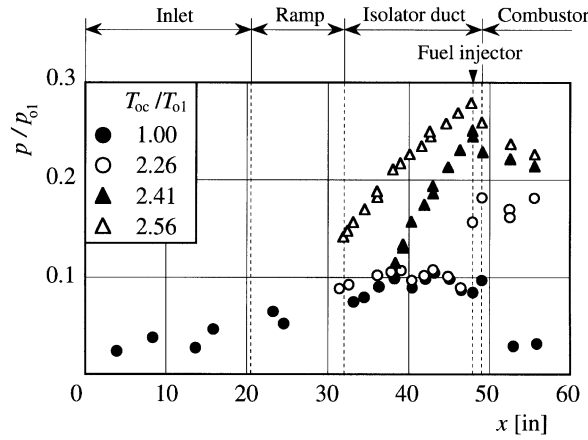


Fig. 28. Axial wall static pressure distributions for different combustor temperature ratios (experimental data from Ref. [59]).

isolator duct has a rectangular cross section (4.00 in by 4.12 in) and 17.24 in long. At the trailing edge of the isolator was a step increase in area (1.5:1) to the combustor section. Fuel injectors were located 1.44 in upstream of the isolator trailing edge.

In Fig. 28 the horizontal axis indicates the distance from the inlet leading edge and the vertical axis is the ratio of the local static pressure  $p$  to the total pressure  $p_{01}$  at the isolator entry. The parameter,  $T_{0c}/T_{01}$ , is the total temperature ratio at the combustor exit and at the isolator inlet. The pressure measurements ahead of the initial pressure rise are in agreement with those made without combustion and are omitted from Fig. 28 for clarity. The different pressure distributions in the figure were a result of the combustor backpressure generated when the engine operates at different fuel-air equivalence ratios. As  $T_{0c}/T_{01}$  increases, the precombustion shock moves upstream due to the rise in back pressure caused by an increasing amount of heat release. For the case of  $T_{0c}/T_{01} = 2.56$ , the head of the precombustion shock train is considered to be located nearly at the isolator entrance.

The static pressure rise and the pressure distribution in the isolator duct is very critical for both ramjet and scramjet modes. The pressure distributions in Fig. 28 are very similar to those in Fig. 7. Bement et al. [59] compared their measured static pressure rise characteristics including the data in Fig. 28 with the pressure distributions predicted by Eq. (1) mentioned in Section 4.2, and they concluded that there is very good agreement between them. However, Eq. (1) is developed for axisymmetric circular ducts. According to Ref. [40], instead of Eq. (1), the following correlation was suggested for rectangular ducts in 1993 by Billig:

$$\frac{x(M_1^2 - 1) \text{Re}_\delta^{1/5}}{H^{1/2} \theta_1^{1/2}} = 50 \left( \frac{p}{p_1} - 1 \right) + 170 \left( \frac{p}{p_1} - 1 \right)^2, \quad (9)$$

where  $H$  is the duct height, and the other notations are the same as those in Eq. (1).

Whether the above equation can be applicable to the precombustion shock train in the isolator duct is still uncertain. The sufficient and accurate measurements of flows in combustor tests are

very difficult. However, more systematic works on the precombustion shock train in the isolator duct will be more promising following the successful design of ramjet and scramjet engines.

#### 7.4. Supersonic ejectors

An ejector [80], shown schematically in Fig. 29, is a device in which a primary gas at high pressure is accelerated by a primary nozzle and the high speed primary gas stream entrains and compresses a secondary gas at low pressure. The ejector is not as efficient as a turbofan or a turbopump, in that the ejector is derived by only purely shear action or mixing action between the primary and secondary streams, but an advantage of the ejector system is in its geometrical simplicity, not having any moving part.

For many years, ejectors have found wide applications in jet pumps and vacuum pumps. More recently, ejectors have been investigated for flight applications, especially as a high altitude simulator for rocket-engine testing [81,82] and a method of thrust augmentation of V/STOL aircraft [83,84]. A detailed analysis of the flow patterns in supersonic ejectors in which the primary gas flow is supersonic is presented by Fabri and Siestrunck [85]. In this section, the flows in supersonic ejectors will be described qualitatively from the standpoint of pseudo-shocks.

Fundamentally, the ejector is designed to draw a given mass flow rate  $m_s$  of induced secondary flow from a reservoir at a given stagnation pressure  $p_{0s}$  into a vessel of higher pressure  $p_a$  (generally the atmospheric pressure). Such a compression is obtained by means of a high-pressure primary flow (mass flow rate  $m_p$ ) which is expanded from the primary stagnation pressure  $p_{0p}$  to the same pressure  $p_a$ .

The exhaust performance of the supersonic ejector is mainly determined by the compatibility conditions of two streams flowing in the same duct called the mixing tube. The supersonic primary flow leaves the primary nozzle and enters the mixing tube of larger cross section. The induced secondary flow comes tangentially into contact with the primary flow in the mixing tube. The mixing tube with a contraction or a throat called the second or ejector throat, as shown in Fig. 29, can increase the pressure recovery over that obtained by a constant area mixing tube [82].

For the given secondary gas stagnation conditions and its mass flow rate, the required minimum stagnation pressure of the primary gas and its mass flow rate depend on many parameters such as the Mach number  $M_p$  at the exit of the primary nozzle, the configuration of the mixing tube,

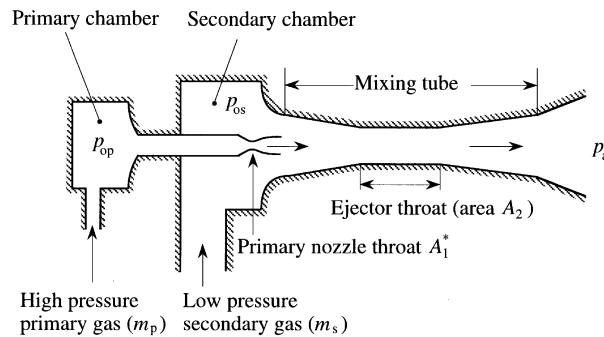


Fig. 29. Schematic illustration of supersonic ejector.

particularly the area ratio of the ejector throat  $A_2$  to the nozzle throat  $A_1^*$ , the relative position of the primary nozzle and the mixing tube, and the back pressure  $p_a$  into which the flow is discharged.

A convenient representation of such an operation is obtained from the nondimensional exhaust performance curve between the ratio of the two mass flow rates,  $m_s/m_p$ , and the ratio of the secondary reservoir pressure to the exhaust pressure,  $p_{0s}/p_a$ , that is, the inverse of the compression ratio. Fabri and Siestrunck [85] classified the performance curves of the ejector with a constant area mixing tube into four patterns, depending on the ratio of the primary reservoir pressure to the exhaust pressure,  $p_{0p}/p_a$ . Matsuo et al. [86] suggested five patterns of the performance curves of the ejector with a throat, depending on the pressure ratio  $p_{0p}/p_a$  and the area ratio  $A_2/A_1^*$ .

An example [86] of schlieren photographs taken in a rectangular supersonic ejector is reproduced in Fig. 30, together with its schematic illustration. The experimental conditions are shown in the caption of the figure. It may be observed that, at this condition, the primary flow is choked at the primary nozzle throat and a shock is standing inside the nozzle. Also, another shock is clearly visible as a “shock train” downstream of the ejector throat. The occurrence of the latter shock indicates that the mixed stream of the primary and secondary flows is choked at the ejector throat.

To estimate the choking condition [87] and the choking location of the flow in the ejector is an important element in the design of a supersonic ejector. The shock generated by the choking of the flow interacts with the boundary layers inside the ejector to form a pseudo-shock, as is clearly visible in Fig. 30. The characteristics and behaviors of the pseudo-shock strongly affect the ejector operation performance. For example, the starting characteristics of the ejector with a second throat depends strongly on the length of the second throat [82]. This can be understood by considering that a pseudo-shock of a finite length is generated in the ejector instead of a single normal shock. Some experiments [88,89] have also shown that the pseudo-shock occurs in the deceleration process of the flow in the ejector. Therefore, in order to predict the ejector performance correctly, the features of the pseudo-shocks should be sufficiently understood.

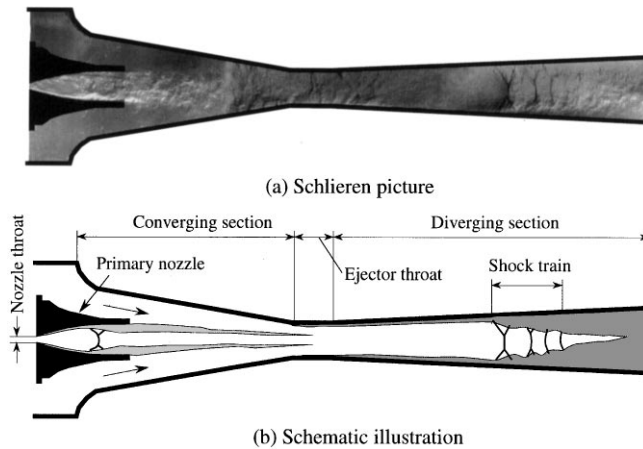


Fig. 30. Schlieren photograph showing supersonic ejector flow and its schematic illustration (the picture reproduced from Ref. [86]) ( $M_p = 3.05$ ,  $A_2/A_1^* = 7.84$ ,  $p_{0p}/p_a = 8.84$ ,  $p_{0s}/p_a = 0.925$ ).

7.5. Shock tubes

The shock tube [90] is a simple and useful device for producing shock waves and high enthalpy flows. It has a variety of applications for investigating various problems in aeronautics, physics, chemistry, etc. In its simplest form the shock tube consists of a long tube divided into two sections by a diaphragm of thin sheet plastic or metal. One side of the diaphragm is charged with gas at high pressure which is called a driver gas, and on the other side a low-pressure gas called a driven or test gas is charged.

A schematic wave diagram of the simplest shock tube is shown in Fig. 31a. When the diaphragm bursts, mechanically or naturally under an increasing pressure difference across the diaphragm, a normal shock front is formed in the low-pressure section and propagates to the right. On the other hand, an expansion wave, which quickly becomes extended, is generated and propagates into the high-pressure section.

The Mach number of the shock generated by the bursting of the diaphragm is mainly determined by the initial pressure ratio,  $p_4/p_1$ , of the driver and driven gases across the diaphragm. Behind the shock, a flow is induced by the shock and a boundary layer is developed along the wall. The shock is followed by a contact surface which divides the driven gas originally in the low-pressure section and compressed and heated by the shock front (this is called a hot or warm gas) from the driver gas originally in the high-pressure section and expanded and cooled by the expansion wave (this is called a cold gas).

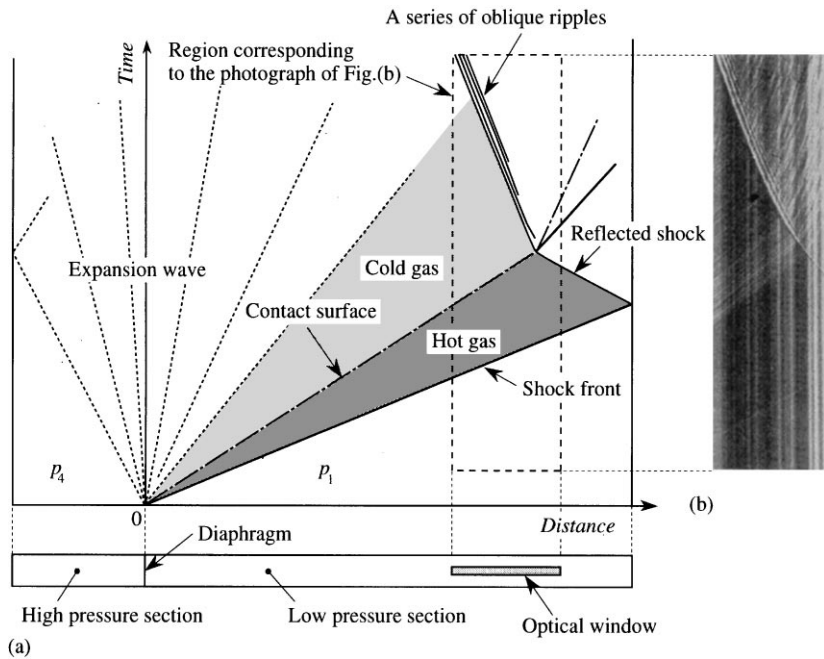


Fig. 31. Wave diagram of shock tube flow and streak schlieren photograph (the photograph reproduced from Ref. [5]). (a) Wave diagram of shock-tube flow. (b) Streak schlieren photograph ( $p_4/p_1 = 30.5$ ).



The shock is reflected at the end of the low-pressure section. The high enthalpy gas behind the reflected shock is used as the reservoir gas for production of hypersonic flows and in chemical kinetic studies. The reflected shock moves to the left and interacts with the boundary layers in the hot gas region induced by the incident shock impinging on the end wall of the low-pressure section. Then the shock meets the contact surface and a collision or interaction occurs between them. One of three possible interaction patterns called undertailored, tailored, and overtailored, occurs depending on the properties of the working gases and the strength of the reflected shock [90].

The streak schlieren photograph shown in Fig. 31b is reproduced from Ref. [5]. This was taken for the initial pressure ratio  $p_4/p_1 = 30.5$  and air as the working gas. The flow inside the shock tube viewed through a narrow and long windows parallel to the tube axis with a schlieren optical system and a drum camera. The photograph can be interpreted to show the region of flow corresponding the dashed rectangle marked in Fig. 31a. It should be noted in the photograph that a series of oblique ripples is observed after the interaction of the reflected shock with the contact surface and that the ripples are approximately parallel with a substantially constant velocity. This seems to indicate that a shock train is generated in the shock tube flow.

Matsuo et al. [91] conducted an experiment on the interaction of the reflected shock with the contact surface using a shock tube of cross section 38 mm square. A series of schlieren photographs taken for  $p_4/p_1 = 340$  and air as the working gas is reproduced in Fig. 32, where  $t$  is the time when the incident shock is reflected at the end wall of the low pressure section. It should be noted here that in real shock tube flows, due to the finite bursting time of the diaphragm and the mixing of the

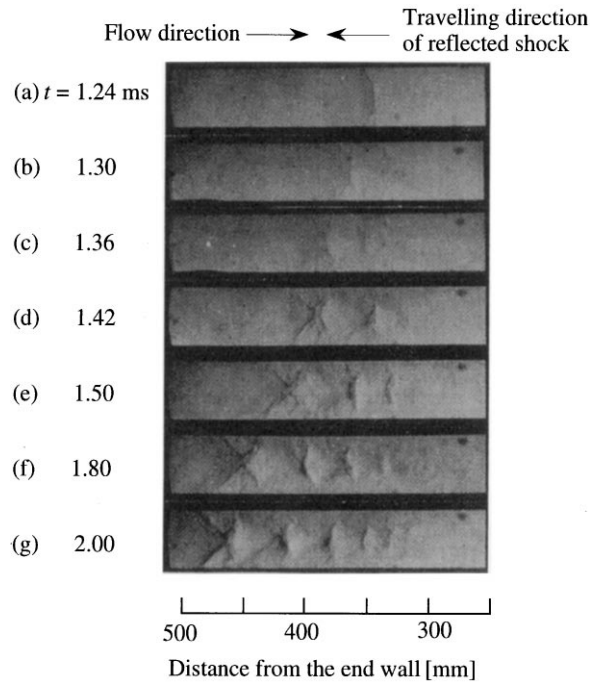


Fig. 32. Schlieren photographs showing the interaction of reflected shock with contact region (reproduced from Ref. [91]).

driver and driven gases, the interface separating the driver gas from the driven gas is not a surface (contact surface) normal to the flow as assumed in the simplest theory, but a mixing region (contact region) having a finite length is formed.

In Fig. 32, the interaction between the reflected shock and the contact region begins in between Fig. 32a and b. Before the interaction, as shown in Fig. 32a, the shock is bifurcated due to the interaction with the wall boundary layers in the hot air region. When the interaction with the contact region begins, as is clearly visible in Fig. 32b–g, after the leading shock, successive shocks are generated and a shock train is formed.

The shock train is not formed by the interaction of the reflected shock only with the boundary layers of the hot gas region, and it is formed by the interaction with the contact region in the case of overtallored conditions [91]. The flow mechanism of transition, in shape of the reflected shock, from the bifurcated shock to the shock train by the interaction with the contact region is discussed in detail in Ref. [91].

### 7.6. Circular thrust gas bearings

For high-speed and lightly loaded bearings, gas and air can be used as lubricants, because gases are readily available and the friction is extremely low. For an externally pressurized gas-lubricated circular thrust bearing, the radial pressure distribution in the clearance between the bearing surface and the moving body surface is very important, because it directly affects the load capacity of the bearing.

Many investigations have been performed on the pressure distributions on the clearance region in the bearings, and it has been observed that, under some operating conditions, particularly at high supply pressures and large clearances, a pressure depression occurs in the neighborhood of the gas supply hole in the pressure distribution [92]. The depression in pressure means that the pressure drops rapidly near the inlet, then rises, and finally decreases up to the atmospheric pressure at the bearing periphery.

This pressure depression contradicted the previous pressure distributions predicted by the theory based on the equations of viscous flows which shows a decreasing in pressure monotonously with the radial distance. The pressure depression phenomenon is undesirable, because it reduces the load capacity and makes the bearing insufficient to use.

Mori [92] considered that the pressure depression may be due to that the flow is choked at the inlet section of the bearing and the flow is accelerated to supersonic at downstream region of the inlet. In this section this phenomenon is discussed from the viewpoint of pseudo-shocks.

For simplicity, he assumed the flow in an externally pressurized circular thrust gas bearing as a radial flow between two parallel plates (radius  $R$ , clearance height  $H$ ) with a single gas supply hole (radius  $r_o$ ) at the center as shown in Fig. 33. The pressurized gas is fed from the supply hole and the flow is choked at the inlet of the clearance. The clearance region consists of two parts, that is, the supersonic region 1 and the subsonic region 2, separated by a single cylindrical normal shock. The flow in the region 1 is a radial, adiabatic, and compressible flow with friction, while the flow in the region 2 is purely viscous flow and the pressure at the exit is the atmospheric pressure  $p_a$ .

With some additional assumptions, he calculated the pressure distribution along the radial distance, and compared the results with his own experimental data. A good agreement was obtained between them. But the calculated results could not explain the gradual recovery of the

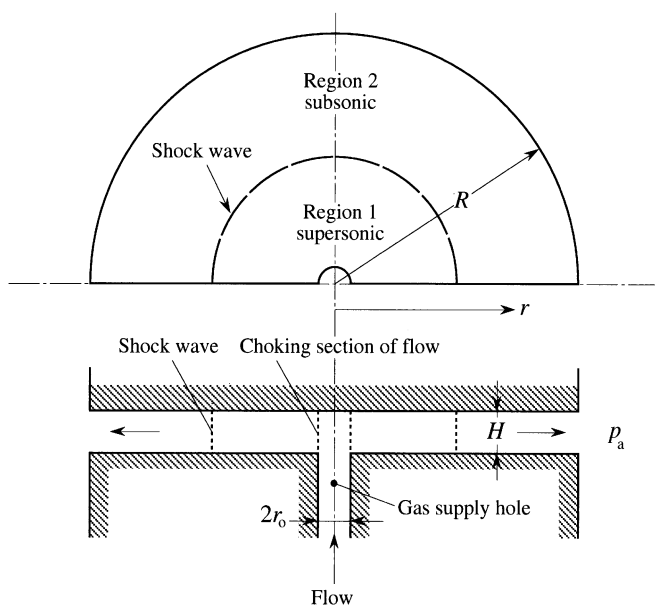


Fig. 33. Schematic illustration of circular thrust gas bearing model in Ref. [92].

pressure in the transition region from supersonic to subsonic velocities which was observed in the experimental pressure distributions.

In order to solve this problem, Mori and Ezuka [93] considered that the normal shock in Fig. 33 should be replaced by a pseudo-shock, and they applied the diffusion model mentioned in Section 6.2 to analyze the flow in an externally pressurized circular thrust gas bearing. An example of their studies is shown in Fig. 34. In the figure, the experimental data were obtained using a circular thrust gas bearing model shown in Fig. 33 with the clearance height  $H = 60, 90$ , and  $120 \mu\text{m}$ , the outer radius of the plate  $R = 30 \text{ mm}$ , and the supply hole radius  $r_o = 2 \text{ mm}$ . Air was used as the working gas. The value of the supply gas pressure was not given in the paper.

The calculated curves in Fig. 34 were obtained by the diffusion model of the pseudo-shock. The point indicated by an arrow represents the maximum pressure in the clearance. The pressure  $p$  in the vertical axis is nondimensionalized by the atmospheric pressure. The calculated pressure distributions are in good agreement with the experimental results, although the experiment was carried out only near the supply hole. It is clearly observed from Fig. 34 that the flow is choked near the inlet of the bearing model and after the acceleration to supersonic speeds, the deceleration to subsonic velocity is done by the pseudo-shock in which the pressure is recovered gradually as predicted by the diffusion model.

In the radial flow between two parallel plates as described in this section, compressed gas is fed at its center and it is accelerated to supersonic in its central region and then, decelerated to subsonic by a cylindrical pseudo-shock, it is further decelerated as the cross-sectional area increases in the radial direction.

The pseudo-shock in such a supersonic radial flow was investigated by Yamane et al. [94,95]. In these papers, they discussed the length and pressure recovery of the pseudo-shock. They defined the

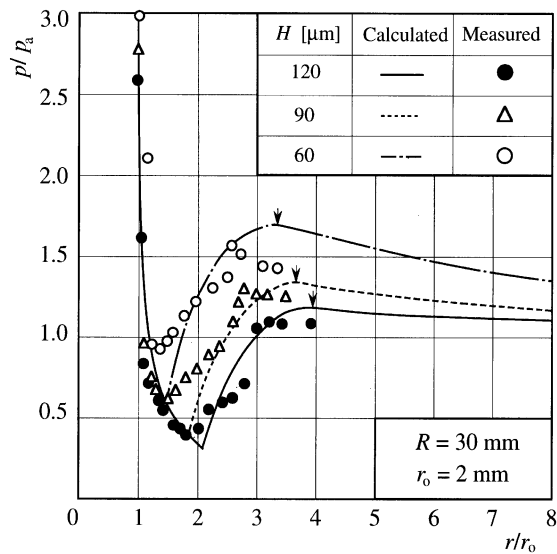


Fig. 34. Radial static pressure distributions in circular thrust gas bearing model (reproduced from Ref. [93]).

final point of the pseudo-shock as the point where the measured pressure distribution deviates from the calculated distribution which is started from the atmospheric pressure at the duct exit, assuming a fully subsonic flow. According to their results, the length and the pressure recovery of the pseudo-shock are smaller than those in a constant area duct. When the radial flow has a swirl, the static pressure recovery decreases with an increasing degree of swirl. These results will be useful in studying the flows in vaneless diffusers of supersonic centrifugal compressors.

7.7. MHD power generators

An electric power is induced resulting from conductors cutting magnetic field lines. In magneto-hydrodynamics (MHD) electric power generation, the conductor is a weakly ionized plasma. Thus, the velocity and electrical conductivity of the plasma are most crucial in MHD power generation. Supersonic flows are of interest in MHD generation, because the power output is proportional to the conductivity and the square of the flow velocity. Therefore, gains in output power and efficiency can be envisaged by making use of supersonic flows. Such a supersonic MHD generator consists of an ionization chamber, supersonic nozzle, generator channel (MHD channel), and diffuser.

Fig. 35 shows two types of MHD power generators. In Fig. 35a, fuel, oxidizer, and seed for ionization are fed into the combustor, and the resulting combustion gas (a weakly ionized plasma) is expanded through the convergent–divergent nozzle to a designated Mach number. The plasma then enters the MHD channel and finally exhausted through the diffuser. The top and bottom of the channel consists of pairs of electrodes connected each other through external load resistances. This type is called a Faraday MHD generator with linear channel. A magnetic field is applied normal to both the flow and electrode directions.

Fig. 35b shows a disk MHD generator. The plasma is fed from the center of the generator, and, accelerated to supersonic velocity through the nozzle, it enters the disk MHD channel. The channel

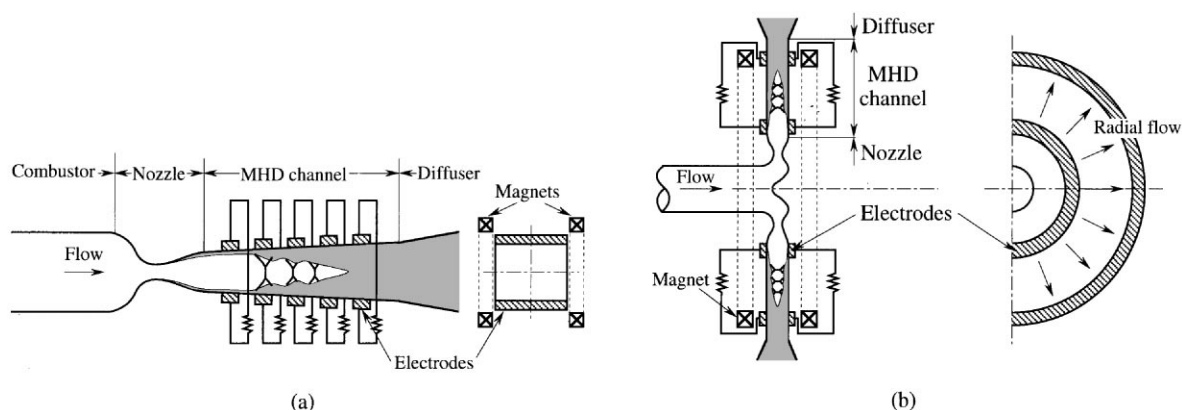


Fig. 35. Schematic illustration of MHD power generator. (a) Faraday type MHD generator (linear channel). (b) Disk type MHD generator (Hall generator).

consists of an inlet circular electrode connected to an exit electrode through an external load resistance, and the electric current flows essentially parallel to the plasma flow. This is called a Hall generator. A magnetic field is applied in the same way as in the Faraday type generator.

The efficiency of the MHD power generator depends strongly on the pressure losses of the working gas passing through the channel. Hence, a great deal of effort has been devoted to make clear the flow in the channel, where a normal shock can stand and interact with the boundary layers, that is, a pseudo-shock may be formed. This section describes some of the previous investigations on the supersonic flows in the MHD channel, paying attention to the pseudo-shock.

Louis et al. [96] conducted an experiment of the combustion-driven Faraday type MHD generator, and showed the location of the shock, its strength, and the length of separated region of the flow. In MHD channel flows, since the Lorentz force can be comparable to the fluid dynamic forces and it acts to the opposite direction of flow, the shock becomes stronger in comparison with the case of no magnetic field. Roy and Wu [97] performed an experiment of the same type of MHD generator. They obtained the static pressure distributions along the generator channel, and mentioned that “the measured pressure shows a gradual rise which indicates that the shock system in the generator is not a single normal shock, but a series of oblique shocks”.

In order to explain the gradually increasing pressure in the supersonic MHD channel mentioned above, Lu and Wang [98] extended Crocco's shockless model of the pseudo-shock described in Section 6.1 to the flow in a linear MHD channel where the cross-sectional area is gradually diverged so that a one-dimensional approach is possible. They considered a channel with a wall consisting of a combination of conductors and electrical insulators, and assumed two flow regions in the MHD channel, a layer near the wall and a main plasma flow in the central portion of the channel. They successfully demonstrated the feasibility of extending Crocco's model to explain qualitatively the observed pressure rise. However, the major drawback in their analysis is the empirical assignment of the axial distribution of the fractional mass flow rate  $\mu$  to start the calculation, as they mentioned in the paper.

The disk MHD generator shown in Fig. 35b has been investigated mainly in Tokyo Institute of Technology [99–101]. An example of the static pressure distribution along the radial direction in

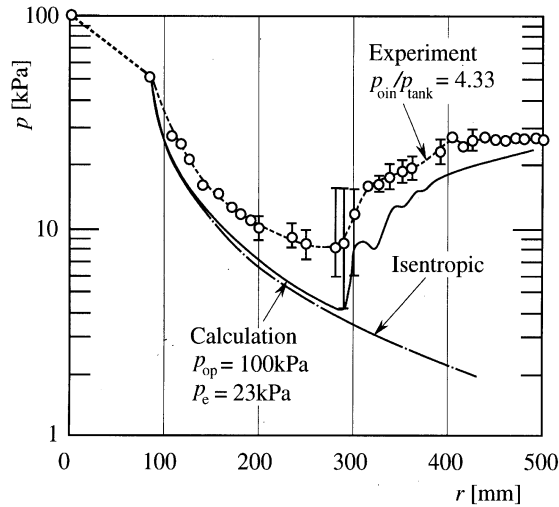


Fig. 36. Wall static pressure distribution along radial direction in a disk MHD generator (experimental and calculated data reproduced from Ref. [99]).

the MHD channel in a case of no power generation (no magnetic field) is shown in Fig. 36 [99]. Air was used as a working gas. The radially diverging channel had a constant height of 20 mm, and the radial distances from the centerline to the inlet (throat) and the exit of the disk channel were 80 mm and 490 mm, respectively. The experimental data were obtained for the condition of the ratio,  $p_{0in}/p_{tank}$ , of the stagnation pressure at the inlet of the generator to the tank pressure downstream of the diffuser was 4.33. The solid line represents the calculated static pressure distribution for the condition of the stagnation pressure  $p_{op}$  upstream of the nozzle is 100 kPa and the exit pressure  $p_e$  is 23 kPa. The pressure ratio is nearly the same as that of the experiment. In the calculation, the compressible Navier–Stokes equation was numerically solved with the boundary condition of a choked flow at the inlet of the channel.

Fig. 36 clearly shows that a pseudo-shock is formed in the channel. The calculated pressure upstream of the shock is close to the isentropic one and lower than the experimental values. The authors mentioned that this difference may be caused by the improper values of some constants in the turbulence model and the insufficiency in the number of grid points. When a magnetic field is applied, the Lorentz force will decelerate the flow, causing more adverse pressure gradient.

The interaction of an electrically conducting gas with a magnetic field in MHD generators produces a very complex flow which is inherently three-dimensional. The MHD pseudo-shock in supersonic generators using high magnetic field strength is directly related to the generator output as well as its efficiency and the sufficient understanding of the phenomenon is left to the future research.

### 7.8. Other flow devices

In addition to the flow devices mentioned above, pseudo-shocks may appear at any place where normal shocks are supposed to stand to decelerate supersonic flows to subsonic and interact with wall boundary layers in internal gas flows. For example, in a supersonic centrifugal compressor, the

flow from an impeller enters in a diffuser at supersonic velocity and the pressure recovery is made in the diffuser. Hence, the supersonic flow is supposed to be decelerated to subsonic by a pseudo-shock in the diffuser.

Although it is very difficult to visualize the flow within turbomachineries, ONERA has several special visualization setups to study aerodynamic flows within a fixed annular cascade, supersonic axial and centrifugal compressors [102]. The schlieren photographs in Fig. 37 were taken in one of the ONERA facilities and reproduced from Ref. [103]. These photographs show the flow within a diffuser with straight blades, taken for the same rotating speed of the impeller of 8000 rpm. The numbers denote the position of the throttle, a higher number corresponding to more choking. In the photograph marked 6, we can see clearly a detached shock at the leading edge of the blade, a weak oblique shock near the inlet and reflected on the blade surface, and a shock train of a pseudo-shock between the blade passage along the flow direction. On the photographs denoted 7, 8, and 9.5, the shock train moves upstream.

Valves are common piping components in a variety of processes. Control valves are pressure reducing devices controlling pressure or mass flow rate by throttling the fluid in the orificial elements. When a gas flows through the converging–diverging passage inside the control valve, the limitation of the mass flow rate through the valve may occur by choking of the flow at the minimum cross section (vena contracta) inside the valve.

Generally, the flow velocity upstream of the valve is low subsonic so that the static pressure  $p_1$  may be equal to its stagnation pressure. Assume that the flow is accelerated to the vena contracta condition (the pressure  $p_c$ ) isentropically inside the valve, and then the static pressure is recovered to  $p_2$  at downstream of the valve. Then the critical pressure ratio for the choking,  $(p_2/p_1)_{\text{crit}}$ , is given by the following equation [104].

$$\left(\frac{p_2}{p_1}\right)_{\text{crit}} = 1 - F_L^2 \left\{ 1 - \left( \frac{2}{\gamma + 1} \right)^{\gamma/(\gamma-1)} \right\}, \quad (10)$$

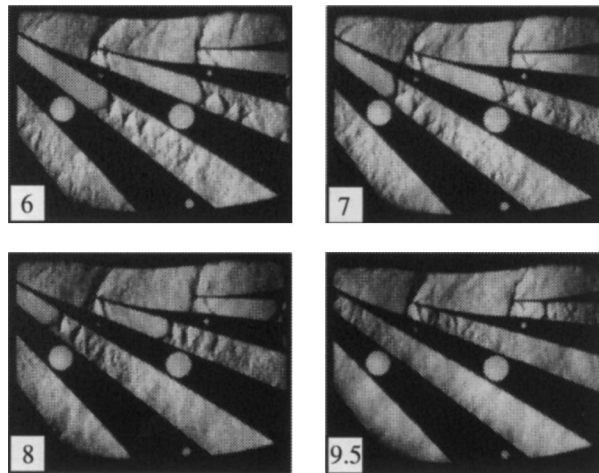


Fig. 37. Schlieren photographs showing the flow in a diffuser with straight blades of a supersonic centrifugal compressor (reproduced from Ref. [103]).

where  $F_L$  is the pressure recovery coefficient defined by  $F_L^2 \equiv (p_1 - p_2)/(p_1 - p_c)$ . For high-pressure recovery (low  $F_L$ ) valves such as butterfly valves ( $F_L \cong 0.5$ ), the critical condition will be reached at lower pressure ratios,  $p_1/p_2$ , across the valve than for the case of low-pressure recovery (high  $F_L$ ) valves such as globe valves ( $F_L \cong 0.95$ ) [104].

An example of the choked air flows through a globe valve is given in Ref. [105] and the paper developed a universal equation of gas flow rate including choked flow conditions for sizing control valves. Addy et al. [106] investigated compressible flow characteristics including mass flow rate, stagnation pressure loss, and static pressure recovery for butterfly valves, and obtained the pressure ratio for the onset of choked flows as a function of the configuration of the valve.

Under the operating condition of choking, a supersonic flow can develop in the vicinity of the vena contracta and downstream of it, and a shock may be generated. Nakano et al. [107] performed an experiment on noise and flow-induced vibration of valve stem using a simple conical plug valve, and obtained some photographs which clearly show shocks generated at downstream of the vena contracta inside the valve. These shocks are extremely complicated in shape.

Brandmaier and Knebel [108] analyzed the flow of steam through a safety valve vent pipe system, which is schematically illustrated in Fig. 38a. The steam from a steam line is, passing through a valve and a discharge elbow, discharged into a vent pipe and finally exhausted to the atmosphere. The vent pipe inlet forms an umbrella fitting, and proper design of the vent pipe is necessary to assure that steam will not be released into the power plant interior.

In order to analyze the flow in the valve and vent pipe, they considered a one-dimensional flow model shown in Fig. 38b. Although mixing of the primary and secondary flows and the flow deceleration occur simultaneously in real flows, this analysis assumed that the two flows first mix

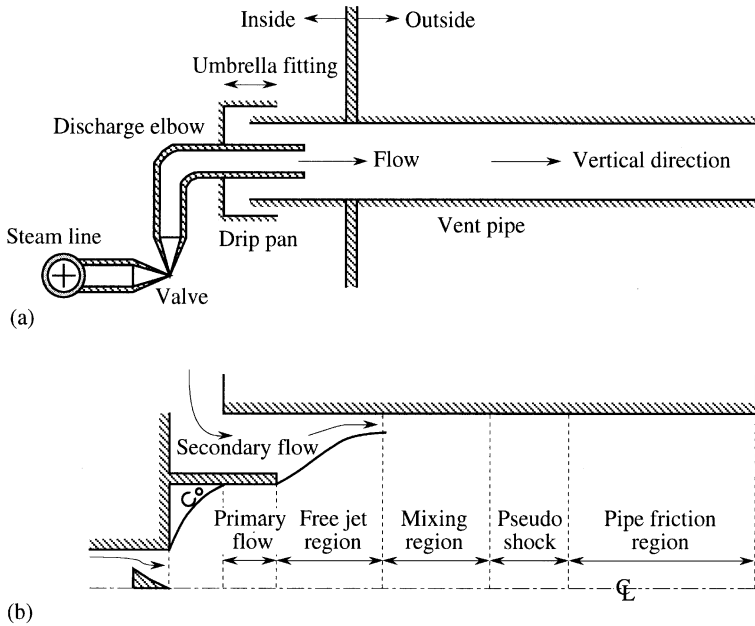


Fig. 38. Safety valve vent pipe system [108]. (a) Schematic illustration. (b) One-dimensional flow model.



to yield a uniform supersonic flow, and then the flow is decelerated through a pseudo-shock. They employed the shockless model by Crocco, and presented a design basis for sizing the vent pipe to prevent blow-back of stream.

At present, a new method for chemical processing called the shock wave reactor [27,109,110] is being developed at the University of Washington. Instead of relying on conventional surface-area heating to initiate pyrolysis, this method uses a standing normal shock in a supersonic flow to achieve a precisely controllable temperature pulse. Hence, the shock wave reactor relies on the temperature recovery after a “normal shock” to initiate the reactors, and it is important to understand the flow field of the shock/boundary layer interaction, i.e., the pseudo-shock in order to design and operate the reactor in a predictable manner.

## 8. Control methods of pseudo-shocks

A normal shock/boundary layer interaction occurring in various flow devices is usually related to the system efficiency or performance, with regard to the total pressure loss, flow instability, and specially required other regulations. Many flow devices very frequently need an appropriate control of the normal shock/boundary layer interaction to meet the design purpose. Until now, a great deal of papers on the control methods of the shock/boundary layer interaction have been presented, and comprehensive reviews were given by Delery [2] and Raghunathan [111]. However, they are for the interaction of a single normal or oblique shock with a boundary layer mainly in an external flow. To our knowledge, there are only a few papers on the control method of the pseudo-shocks in ducts. In this section, we will describe the control techniques which have been applied to the flow field including the pseudo-shock to date.

### 8.1. Boundary layer suction

The performance of flow devices including a pseudo-shock is substantially influenced by both the length of the flow device and the boundary layer characteristics on the device wall, because the pseudo-shock, introduced into the device as a result of the interaction of a normal shock with a boundary layer along the wall, has a finite length. If the boundary layer is thin, there will exist a single nearly normal shock in the device. That is, the boundary layer is indeed responsible for the complicated flow pattern with a series of shocks.

The two schlieren photographs in Fig. 39, reproduced from the paper by Weise [112], clearly show the effect of the boundary layer on the shape of shock train. A shock train is visible in Fig. 39a, where the two slits provided for a removal of boundary layer by suction were unused, and Weise described that “the slits lie in the dead-air region and are therefore inconsequential to the flow”. When the boundary layer upstream of the shock train is removed by suction through the slits, as shown in Fig. 39b, a single nearly normal shock is formed and flow separation is not observed. These photographs were cited in the textbook by Shapiro [6].

Another example [33] of the boundary layer removal from the flow field including the pseudo-shock is shown in Fig. 40, with a schematic illustration of the experimental apparatus. The experiment was conducted in a 98 mm by 254 mm supersonic wind tunnel operating at a nozzle exit Mach number of  $M_i = 2.0$  and at a unit Reynolds number of approximately  $1.6 \times 10^7/\text{m}$ . The

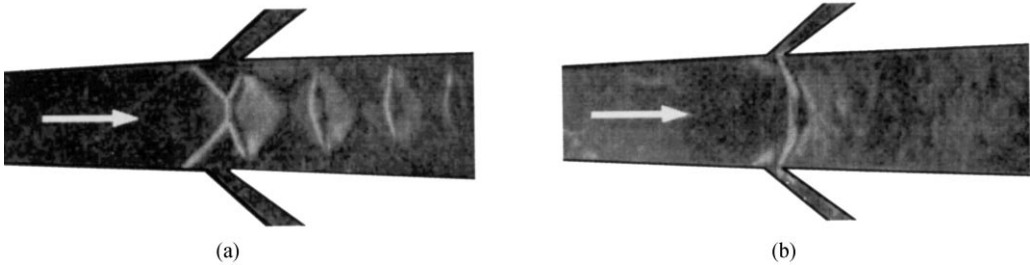


Fig. 39. Schlieren photographs showing the effect of boundary layer removal on the shock train in a supersonic diffuser (reproduced from Ref. [112]). (a) Without boundary layer suction. (b) With boundary layer suction.

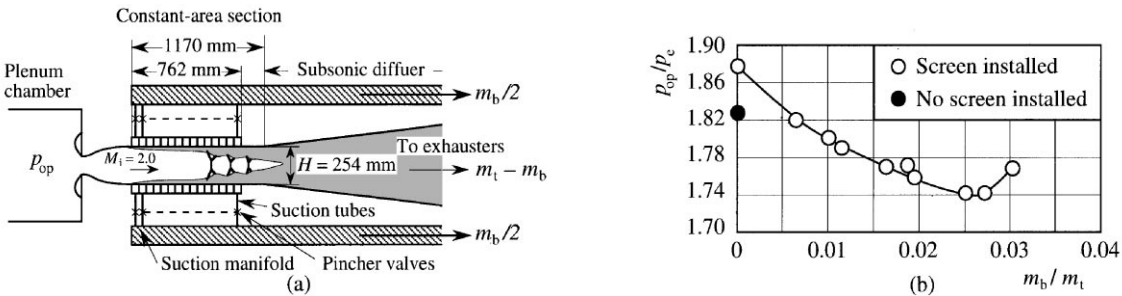


Fig. 40. Effect of boundary layer suction on overall pressure ratios (Experimental data from Ref. [33]). (a) Schematic diagram of boundary layer suction installation. (b) Variation of overall pressure ratio by boundary layer suction.

nozzle from throat to test section was 975 mm long. Behind the nozzle was a constant-area section (test section) of 1170 mm long followed by a subsonic diffuser of 3530 mm long with a rectangular cross section. A part of the top and bottom walls of the constant area test section consisted of the porous walls which were each 762 mm long and 98 mm wide and were divided into 15 51-mm compartments with 40 mesh screen of 18% open area. For each run, the tunnel outlet valve was so adjusted that the pseudo-shock was located at a prescribed position in the constant area section or in the subsonic diffuser. Then an approximately uniform distribution of boundary layer removal was set by the pincher valves shown in Fig. 40a.

An example of the results is shown in Fig. 40b. These data were obtained by controlling the tunnel outlet valve so that the head (onset of pressure rise) of the pseudo-shock was located at 662 mm downstream of the inlet of the test section. This means that, as shown in Fig. 40a, the boundary layer suction was conducted at upstream and inside of the pseudo-shock.

In Fig. 40b, the horizontal axis indicates the ratio of the mass flow rate of air bled  $m_b$  to the total mass flow of air passing through the tunnel  $m_t$  and the vertical axis is the ratio of the plenum pressure  $p_{op}$  to the pressure  $p_e$  at the exit of the subsonic diffuser, that is, the overall pressure ratio  $p_{op}/p_e$  of the tunnel. The white circles show the case of the screen installed, and the black circle on the vertical axis the case of the nonpermeable walls instead of the porous walls. From the two experimental points on the vertical axis, it is said that the installation of the porous walls caused the value of  $p_{op}/p_e$  to increase in the case of no boundary layer suction.

The  $p_{0p}/p_e$  in Fig. 40b decreases with an increase in  $m_b/m_t$  and reaches a minimum value at  $m_b/m_t = \text{about } 0.025$ . The decrease in the overall pressure ratio with an increasing bleed mass flow rate may be due to the fact that the interaction of the shock with the boundary layer becomes weaker so that the pseudo-shock tends to a normal shock. After the minimum point,  $p_{0p}/p_e$  begins to increase again with an increasing  $m_b/m_t$ . This trend is probably due to the increase in Mach number upstream of the pseudo-shock which was caused by an effective area increase by means of the excessive suction.

An appropriate boundary layer suction can reduce the overall pressure ratio required for operating supersonic wind tunnels. However, it also requires an additional work to derive it or there are practical difficulties for the design. There are also many unknown parameters with respect to the suction effects on the performance of the devices including the pseudo-shock. The characteristics of the pseudo-shock should be more thoroughly investigated before this technique would be available to control the pseudo-shock.

## 8.2. Passive control

There are several passive techniques which have been developed for the purpose of artificially controlling the behavior of the shock/boundary layer interaction. The two typical techniques are vortex generators and a passive cavity. The effect of vortex generators is to produce a vortices which energize the low-momentum flow in the boundary layer by transferring the high-momentum fluid from the outer region of the boundary layer. If the vortex generator were to be upstream region of the shock-induced boundary layer separation, this would allow the boundary layer to negotiate the pressure rise without separation or lead to a reduction in separation.

The other technique, passive cavity, consists of replacing a part of the wall surface by a porous plate and a cavity underneath located in the region of the shock/boundary layer interaction [111]. The static pressure rise across the shock will result in a flow through the cavity from downstream to upstream of the shock and produces a system of weaker shocks, causing beneficial reduction in total pressure loss through the shock.

McCormick [25] conducted an experimental comparison of the two passive approaches on the shock/boundary layer interaction in an axisymmetric wind tunnel. The schematic sketches of the experimental apparatus in Ref. [25] are shown in Fig. 41. The test section was 114 mm inlet

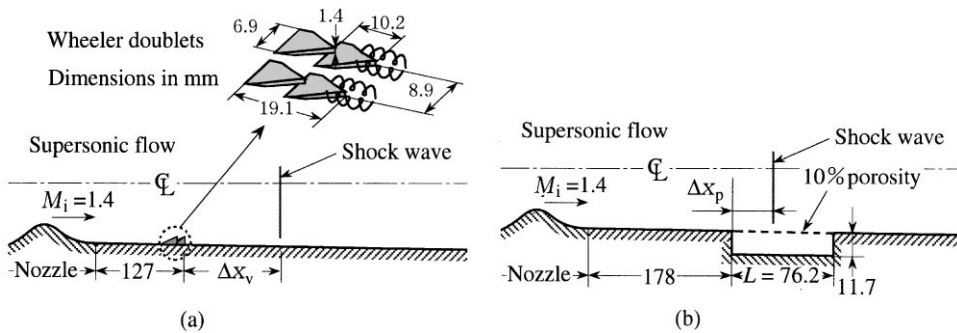


Fig. 41. Schematic sketch of experimental apparatus in Ref. [25]. (a) Vortex generators. (b) Passive cavity.

diameter and 635 mm long that diverged slightly at one degree (half-angle) to the nozzle centerline. The flow Mach number at the test section inlet (nozzle exit) was  $M_i = 1.4$ . Because of the divergence of the test section, the freestream Mach number upstream of the shock varied from  $M_{1e} = 1.56$  to 1.65, depending on the shock position in the test section. The undisturbed boundary layer thickness (no vortex generators present and shock far downstream) at the shock location ranged from  $\delta_1 = 4.6$  to 5.8 mm for the corresponding shock location from the test section inlet of 178 to 279 mm.

As shown in Fig. 41a, the Wheeler doublet generators, which create a counter-rotating array of vortices, were installed at the axial location 127 mm from the test section inlet. The height of the vortex generators was 1.4 mm and the lateral spacing was 8.9 mm. The undisturbed boundary layer thickness at the vortex generator location,  $\delta_v$ , was 3.9 mm. The passive cavity, as shown in Fig. 41b, were 76.2 mm long by 11.7 mm deep. The porosity of the wall was 10%. The passive cavity began at 178 mm from the test section inlet such that the cavity was approximately located in the shock region where the vortex generators provided the most alleviation.

The effects of the two passive control techniques on the wall static pressure distributions in the region of the pseudo-shock are reproduced in Fig. 42 [25]. The shock location from the test section inlet was 203 mm for all of the data in this figure. In the case, the freestream Mach number just upstream of the shock was  $M_{1e} = 1.58$ . The relative shock location from the downstream tip of the vortex generator,  $\Delta x_v$ , was  $20\delta_v$ , while the relative shock location from the leading edge of the cavity,  $\Delta x_p$ , was 0.33 times the length of the cavity  $L$ . The vertical axis is the ratio of the local static pressure  $p$  on the wall to the upstream plenum pressure  $p_{0p}$ . The horizontal axis indicates the ratio of the distance  $x$  streamwise from the location of the ideal normal shock to the undisturbed boundary layer thickness  $\delta_1$  just upstream of the shock. The dashed (marked Ideal) and solid (marked Base) lines represent the wall static pressure distributions in the case of single normal shock without boundary layer and the case of no passive control applied, respectively.

As is recognized from the pressure distribution shown by the circular symbols, the vortex generators eliminates the inflection point in the pressure distribution of the baseline, that is, the

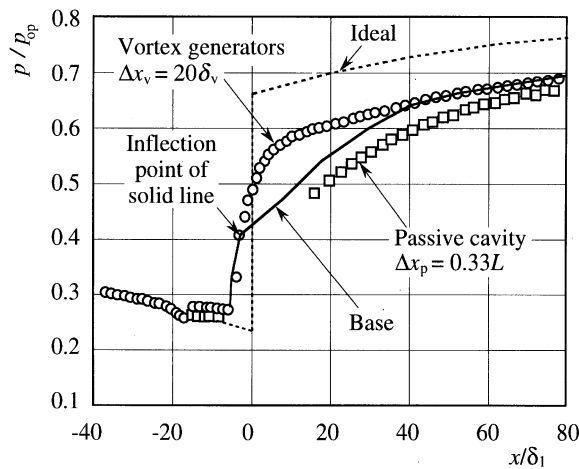


Fig. 42. Effect of passive control on wall static pressure distributions (experimental data from Ref. [25]).

shock-induced boundary layer separation is significantly suppressed. The interaction length defined as the distance from the initial pressure rise to where the distribution parallels the ideal curve is greatly reduced. While, the static pressure distribution for the passive cavity shown by the square symbols is very similar in shape to the baseline case but depressed in value. The interaction length appears to be somewhat increased, that is, the passive cavity spreads the pressure rise over a larger axial length. This means that the length of the pseudo-shock is increased. The depressed value in static pressure relative to the baseline curve is mainly due to the decrease in static pressure rise through the more oblique shock system and partially to the increased thickening of the boundary layer.

The advantage of the passive cavity is the reduction of the total pressure loss across the shock system. Fig. 43 [25] shows the distributions of the cross-sectional mass-averaged total pressure  $p_{0m}$  nondimensionalized by the upstream stagnation pressure  $p_{0p}$ , in the case that the shock position from the test section inlet is 230 mm ( $\Delta x_v = 26\delta_v$ ,  $\Delta x_p = 0.67L$ ). The horizontal axis is the ratio of the distance downstream from the shock position to the undisturbed boundary layer thickness  $\delta_1$ . The passive cavity has the highest mass-averaged total pressure over all of the range measured, followed by the baseline and then the vortex generator data. The relatively low total pressure illustrates the primary disadvantage of the vortex generators. However, the rate of decrease is not as rapid as the baseline and the passive cavity.

The passive cavity control technique was applied to the pseudo-shock in a rectangular duct by Matsuo et al. [113]. They showed that the flow including the shock train is substantially affected, and that, at a certain condition, a flow similar to the shockless state suggested by Crocco described in Section 6.1 is achieved. The total pressure within the pseudo-shock in the case is decreased gradually due to the mixing loss between the high velocity flow in the central core and the low velocity flow in the neighborhood of the wall.

Some other passive control techniques have been applied to the flow field including the pseudo-shocks so far. In order to reduce the required length of a duct for the pressure recovery by the pseudo-shock, Neumann and Lustwerk [4] conducted an experiment of a “multicellular

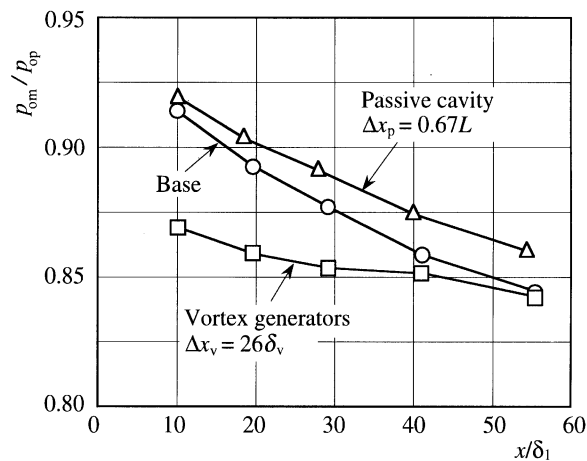


Fig. 43. Effect of passive control on total pressure (experimental data from Ref. [25]).

diffuser”, by introducing some dividing plates into the flow passage in a diffuser. Since the equivalent diameter of each cell divided by the plates is smaller than that of the original diffuser and the length of the pseudo-shock is directly proportional to the duct diameter for the same incoming Mach number as mentioned in Section 4.5, the pressure recovery region is supposed to decrease in the multicellular diffuser. They reported that the overall length can be reduced 25% over the original diffuser without loss in efficiency. Similar control method was reported by Hasinger and Miller [114].

Another method is the use of a small protuberance on the duct wall. The small protuberance can alter the characteristics of the shock train. Existence of such a protuberance, when it is small compared with the incoming boundary layer thickness, can keep to fix the leading shock of the shock train at the leading edge of the protuberance, thereby changing the global shape of the shock train. Miyazato et al. [115] showed that when foot of the leading shock of a normal shock train is at just upstream of the protuberance, the normal shock train nearly changes in shape to a series of weak oblique shocks, extending over a longer distance. Although they did not measure the total pressure loss in the case, it may be reduced by introducing the very small protuberance in the pseudo-shock region.

## **9. Self-excited oscillations of pseudo-shocks**

When no boundary layer is present, the location of a normal shock in internal flows is easily determined and fixed provided that the upstream and downstream pressures and the flow passage geometry are known. This is not so straightforward under such a circumstance that the shock interacts with the wall boundary layers. For example, the terminal shock illustrated in Fig. 25 in Section 7.2 indicates its time-mean position and shape. In real flows, the shock position fluctuates with time, even if the boundary conditions such as the pressures upstream and downstream of the flow are held constant [39].

A lot of papers have been reported on the shock position oscillations and the resulting pressure fluctuations in transonic diffuser flows [116–121], the oscillations of the pseudo-shocks in constant area ducts [53–57], and the shock oscillations in supersonic diffusers [122,123]. A review paper on the self-excited oscillations in internal transonic flows is presented by Meier et al. [124]. The pressure fluctuation caused by shock oscillation gives rise to the fluctuating wall loads as well as the violent noise generation. There may be a fatigue failure of the flow passage, if the oscillation is sufficiently strong. However, it should be said that our present understanding of these shock oscillations is rather limited and many physical aspects of the oscillation are not well understood.

In this section, at first, we describe the self-excited shock oscillations in transonic diffusers extensively performed by Sajben et al. [116–118] and Bogar et al. [119,120] in McDonnell Douglas Research Laboratories. The flow Mach number in these papers is not so high as a pseudo-shock is formed in the flow passage, but the results described in these papers seem to bring light on the essential characteristics of the flow oscillations caused by the shock/boundary layer interactions in internal gas flows. Then, the self-excited oscillation of the pseudo-shock is described in the subsequent sections in this section. The common characteristics of the shock oscillation caused by the interaction with the boundary layer are presented, using the previous experimental data.

### 9.1. Shock oscillations in transonic diffusers

Sajben et al. [116,117] performed an experiment involving two-dimensional transonic diffuser flows including a shock near the throat, for investigating flow fluctuations appearing in a supersonic inlet aircraft system, which is called dynamic inlet distortion in propulsion technology. The experimental apparatus is shown in Fig. 44. The diffuser model was a converging-diverging channel with a flat bottom, equipped with an elaborate boundary layer slots (not depicted in the figure) to ensure acceptable two-dimensionality of the flow. The exit-to-throat height ratio  $H_e/H^*$  of this model is 2.38. This model was attached to a plenum chamber (pressure  $p_{op}$ ) immediately upstream of the model, and the flow from the model was discharged to the atmosphere (pressure  $p_e$ ).

Shock position records were obtained from high-speed schlieren films, and the streamwise position of the intersection between the upstream edge of the shock and a horizontal line 25.4 mm above the bottom wall was recorded. A typical shock position versus time is shown in Fig. 45 [116], where the vertical axis represents the streamwise shock position from the throat station. This was recorded for the pressure ratio of  $p_{op}/p_e = 1.13$ . The oscillation seems to be rather random, but it has some peaks in power spectral density distributions, as will be described later.

The experimental results of the time-mean flow characteristics is given in Fig. 46 [117]. The horizontal axis is the overall pressure ratio  $p_{op}/p_e$ , and the vertical axis denotes the nondimensional streamwise distances from the throat section to the separation point at the top wall  $x_s/H^*$ , the

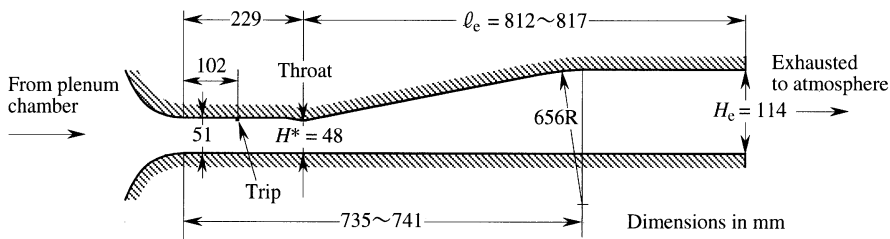


Fig. 44. Wall contours and principle dimensions of two-dimensional diffuser model in Refs. [116,117].

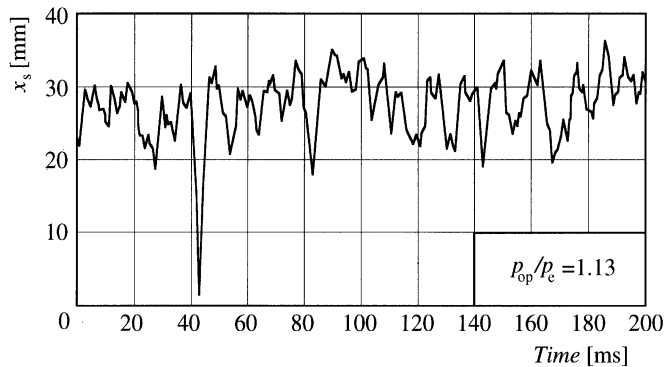


Fig. 45. Typical shock position versus time record in transonic diffuser flows (reproduced from Ref. [116]).

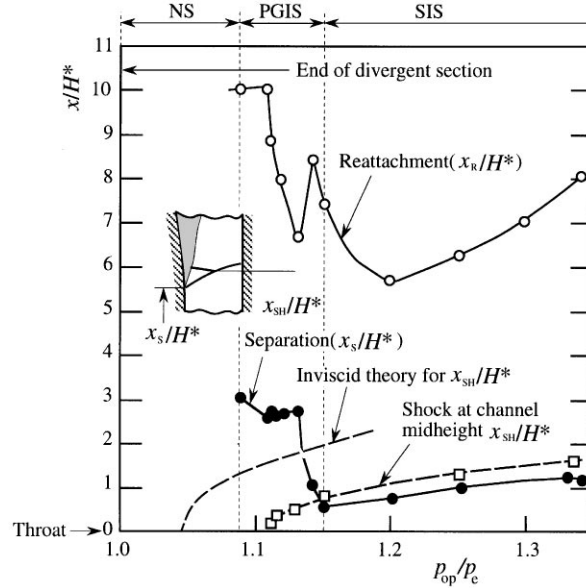


Fig. 46. Time-mean flow characteristics in two-dimensional transonic diffuser model (experimental data reproduced from Ref. [117]).

time-mean shock position at the channel midheight  $x_{SH}/H^*$  and its position predicted by inviscid theory, and the reattachment point of flow at the top wall  $x_R/H^*$ , where  $H^*$  is the throat height.

From the results shown in Fig. 46, the transonic diffuser flows can be classified into three types, that is, no separation flow (NS), pressure-gradient-induced separation flow(PGIS), and shock-induced separation flow (SIS). The range of  $p_{op}/p_e$  corresponding to each type is shown at the top of the figure. Sajben et al. [116,117] recognized that the character of the shock fluctuations is dependent on the immediate cause of separation. For the case of PGIS, the peak oscillation frequency decreases with the shock strength, and there is a significant spectral content at low frequencies. For the case of SIS, peak frequencies and shock oscillation amplitudes both increase with the shock strength.

The flow patterns mentioned above depends not only on the pressure ratio  $p_{op}/p_e$  or the Mach number  $M_{1e}$  immediately upstream of the shock, but also on the diffuser geometry. McDonnell Douglas Research Laboratories conducted two-dimensional transonic diffuser tests using another model [118,119], which has an exit-to-throat height ratio of  $H_e/H^* = 1.52$  that is smaller than that of Fig. 44. In this experiment, the PGIS mode did not appear, and only the NS and SIS modes including the transition phase between them were observed. One of the results is reproduced in Fig. 47, where the vertical axis denotes the peak frequencies observed in the shock displacement power spectral density distributions. Here, it should be added to say that Ref. [118] mentioned that the number and frequencies of these peaks are strong functions of both  $M_{1e}$  and the diffuser length  $\ell_e$  (see Fig. 44). Fig. 47 shows the results in the case of a rather short diffuser length.

From the experimental results including Fig. 47, Bogar et al. [118] concluded as follows: For the Mach number  $M_{1e}$  below about 1.27 (NS mode), the mechanism of the oscillation is the propaga-



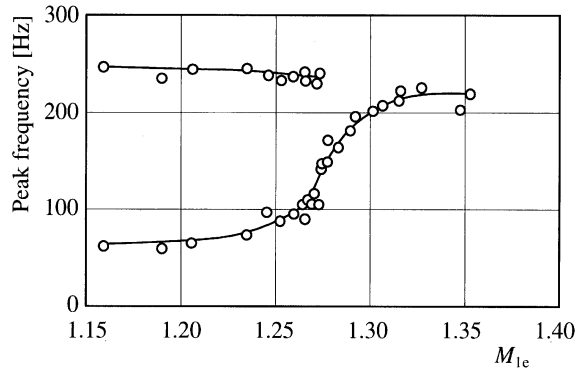


Fig. 47. Mach number dependence of shock motion spectral peaks in transonic diffuser flows (reproduced from Ref. [118]).

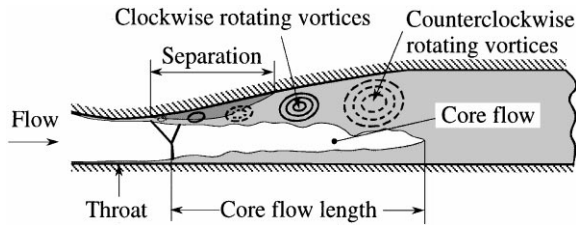


Fig. 48. Schematic illustration of diffuser flow with shock-induced separation after Refs. [118,120].

tion of acoustic waves along the channel in both upstream and downstream directions. Hence, the frequencies of the higher harmonic may appear and they scale inversely with the distance from the shock position to the exit of the diffuser. The frequencies of these oscillations are well predicted by inviscid, one-dimensional, acoustic calculations. On the other hand, in the case of SIS for  $M_{1e}$  above 1.27, the single-peak frequency (about 210 Hz) observed in Fig. 47 is independent of the diffuser length and not predicted by the acoustic theory. The mechanism of this mode of oscillation was not clear.

Bogar et al. [118] considered that the frequency in the SIS mode may scale with the length of the time-mean core flow, which is shown in Fig. 48. The core flow region was defined as that within which the mean total pressure is between 98 and 100% of the time-mean, post-shock total pressure, and they obtained experimentally the relation between the core flow length and the upstream Mach number  $M_{1e}$ .

In order to investigate the modal structure of the oscillations in the SIS flows, using the same diffuser model as that of Ref. [118], Bogar [119] made simultaneous measurements of the instantaneous shock location by a shock imaging camera and the subsonic velocity flowfield by a laser Doppler velocimeter system. As the result, as shown in Fig. 48, he observed the presence of a downstream-traveling, counterrotating vortices that originates successively near the upstream edge of the separation bubble and migrates toward the centerline of the flow, as it is convected downstream at approximately one-half of the core flow velocity.

Bogar [119] did not provide any information about the relation between the observed flow characteristics and the frequency of the shock oscillations in the SIS mode, but his experiment seems to suggest that the frequency may be dependent of the successive generation of vortices near the separation bubble and the length of the inviscid core flow.

Hsieh et al. [120] performed a numerical simulation for self-excited shock oscillations in the same geometry of the transonic diffuser as that of Ref. [119], and reported that the formation of a succession of downstream-traveling vortices observed experimentally is also vividly displayed in the numerical results and that the predicted frequency is about 50% higher than the experimental value. In a pseudo-shock flow which will be discussed in the following sections, the shock-induced separation inevitably occurs. The experimental and numerical results mentioned above may be of value, in considering the oscillation of pseudo-shocks.

## 9.2. Oscillations of shock trains

The self-excited oscillation of the shock train generated in internal gas flows has been recognized as from those of old. For example, in relation to Fig. 39a in Section 8.1, Weise [112] in 1947 described that “the photograph shows another significant fact, namely, the appearance of waves downstream from the forkes, and a certain fluctuation of the phenomenon was confirmed by slow-motion pictures”. Also, Cohen and Valerino [33] in 1950, relating to the shock configuration shown in Fig. 40 in Section 8.1, mentioned that “the configuration would oscillate as a unit in upstream-downstream direction with an unconstant frequency” when no suction was applied, and that “with optimum bleedoff, the amplitude of the oscillation was greatly reduced”. Furthermore, Wegener and Lobb [69] conducted an experiment on a hypersonic wind tunnel diffuser test in 1953, and described in the paper that “aft of the throat, transition to subsonic flow takes place through an oscillating shock system”.

Probably the first experimental investigation of the shock train oscillation in a constant area straight duct was performed by Ikui et al. [53] in 1974. Later, the phenomenon was studied mainly in Japan [54–57]. The apparatus in Ref. [53] consisted of a plenum chamber, supersonic nozzle, test section with a 60 mm square cross section and 830 mm in length, and diffuser. High pressure air in a reservoir was led to the nozzle, and passing through the test section and diffuser, discharged to the atmosphere. After a pseudo-shock was introduced into the test section by controlling the upstream pressure and then keeping the upstream pressure constant, the instantaneous displacements of the shock train were recorded by a high speed schlieren camera system.

An example [53] of each shock position fluctuation of the shock train versus time is reproduced in Fig. 49, where the freestream Mach number immediately upstream of the shock was 2.79, and the Reynolds number based on the equivalent diameter of the duct was  $2.21 \times 10^6$ , and the frame speed was 7440 fps. The vertical axis denotes the nondimensional distance streamwise from the reference point (450 mm downstream from the duct inlet) divided by the equivalent diameter of the duct, and  $x_1$ , etc., denote the first shock position constituting the shock train, etc., respectively. This figure shows clearly that the oscillations of each shock forming the shock train are of similar fashion. Ikui et al. [53] mentioned in their paper that the amplitude of oscillation increases with an increase of the flow Mach number just upstream of the shock, and that the spectral density distribution of the oscillation has two prominent peaks of a several 10 Hz and several 100 Hz.

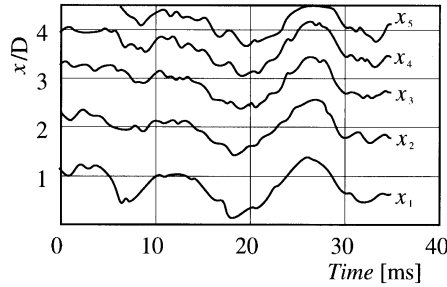


Fig. 49. Oscillation of shock train with time in constant area duct (reproduced from Ref. [53],  $M_{1e} = 2.79$ ,  $Re_D = 2.21 \times 10^6$ ).

Ikui et al. [53] guessed that the shock train oscillation might be resulting from the turbulent fluctuation involved in the incoming flow. Later Yamane et al. [54,55] conducted similar experiments in a constant area duct, and ascribed the oscillation to the pressure fluctuation which propagates upstream from low subsonic region far downstream of the shock train. Recently, Sugiyama et al. [56] argued that the unsteady separation motion at the foot of shock causes the shock train oscillation. This conflict is unlikely to be resolved in near future, unless more systematic work is made.

The current numerical calculation methods are largely based on time-mean flow physics without taking account of the shock oscillation effect. Thus the resulting computational results might have not captured some important features of the shock train flow, thus their validity being very questionable. The lack of the detailed information on shock train oscillation has so far hampered the development of more realistic mathematical approach for the oscillation. To the authors' knowledge, there is no computational work with respect to the shock train oscillation, although the oscillation problems have been observed for a long time.

### 9.3. Correlation between shock oscillations and pressure fluctuations

The oscillation of each shock constituting the shock train gives rise to pressure fluctuation not only in the shock train region but also at the downstream region of the pseudo-shock. Matsuo et al. [57] investigated experimentally the correlation between the shock oscillations and the resulting pressure fluctuations. The test section had a rectangular cross section with a height at the inlet of 25 mm. The top and bottom walls were inclined at  $0.4^\circ$  to the centerline to stabilize the time-mean location of the pseudo-shock. The wall static pressures were measured on the bottom surface, and the static pressure distributions along the centerline of the test section were also measured by using a through-tube inserted in the test section.

A typical schlieren photograph of the shock train in the test section and its illustration for explanation is reproduced from Ref. [57] in Fig. 50. This photograph was taken for the condition of the Mach number and boundary layer thickness just upstream of the shock was 1.75 and 4 mm, respectively, and the Reynolds number based upon the boundary layer thickness was  $1.2 \times 10^5$ . The significance of the time-mean flow seen in the photograph should be noticed before we discuss the fluctuating static pressure data. The first shock is shaped like a lambda, while the following shocks

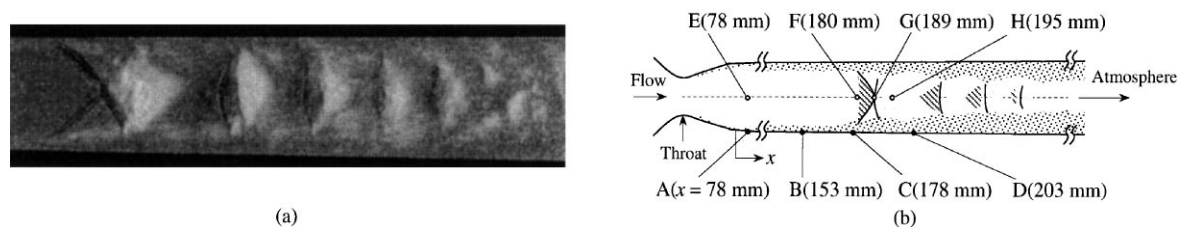


Fig. 50. Schlieren photograph showing shock train in constant area duct and its schematic illustration for explanation (reproduced from Ref. [57]). (a) Schlieren photograph of shock train. (b) Schematic illustration of Fig. (a).

are seen to be of nearly normal shock. The region near the boundary layer edge remains supersonic throughout the interaction, while the core flow goes subsonic following each shock consisting of the shock train. A large increase in the boundary layer thickness occurs under the first shock. Each successive shock is weaker, and the spacing between successive shocks decreases through the interaction.

In Fig. 50b, the points marked A, B, C, and D on the bottom wall indicate the measuring stations of the static pressures, and the locations of these points (distance  $x$  from the inlet of the test section along the duct) are shown in the figure. The static pressure along the centerline of the duct was measured not discretely but continuously in this experiment by a through-tube, and the points marked E, F, G, and H in Fig. 50b was chosen to discuss the intermittency characteristics of the pressure fluctuations. The point E is located on the duct axis at the same cross section as that of the point A. The point G ( $x = 189$  mm) represents just the time-mean position of the first shock on the centerline, and the points F and H are located at the positions of 9 mm upstream and 6 mm downstream of the first shock, respectively.

The pressure histories with time at the points E, F, G, and H are reproduced from Ref. [57] in Fig. 51, where the vertical axis denotes the pressure ratio of the local static pressure  $p$  to the plenum pressure  $p_{op}$ , and the ratio  $p_m/p_{op}$  of the time-mean pressure  $p_m$  at each point to  $p_{op}$  is shown by the arrow on the right side of each figure. The oscillation of the static pressure at point E is negligibly small. In Fig. 51b, special attention should be paid to the fact that the pressure at the point F becomes intermittently higher than the time-mean value. Contrary to this, the pressure at the point H in Fig. 51d becomes lower intermittently than the time-mean value. These are caused by the first shock passing through these points intermittently. The pressure at point G in Fig. 51c oscillates both to the higher and lower sides from its time-mean value in nearly the same manner, since this point is located exactly at the time-mean position of the first shock. The maximum amplitude in this case amounts to about 17 kPa, which is 17% of the atmospheric pressure.

The above-mentioned nature of instantaneous static pressure under moving shock situations was observed, probably at first, in a forward-facing step flow by Kistler [125] in 1964. Since then, many researchers observed such a intermittency in shock/boundary layer interaction regions, mostly, in external flows. For example, Dolling and Murphy [126] described the intermittent wall pressure signal in a flow past a two-dimensional compression ramp, and Hayashi et al. [127] observed the intermittent thin-film heat-transfer gage signal in the interaction flows of oblique shocks with boundary layers on a flat plate. In internal flows, Kim et al. [121] reported such an intermittency in supersonic diffuser flows.

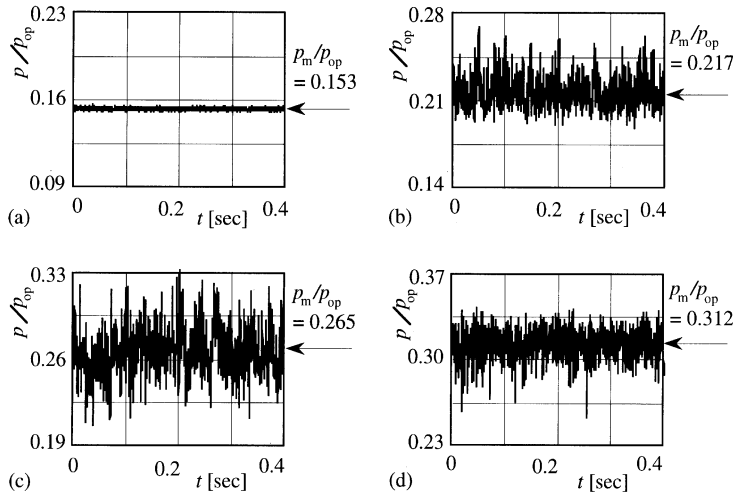


Fig. 51. Pressure-time history showing static pressure oscillations on the centerline of constant area duct (reproduced from Ref. [57]). (a) Point E (far upstream of the first shock). (b) Point F (immediately upstream of the first shock). (c) Point G (just at the first shock). (d) Point H (immediately downstream of the first shock).

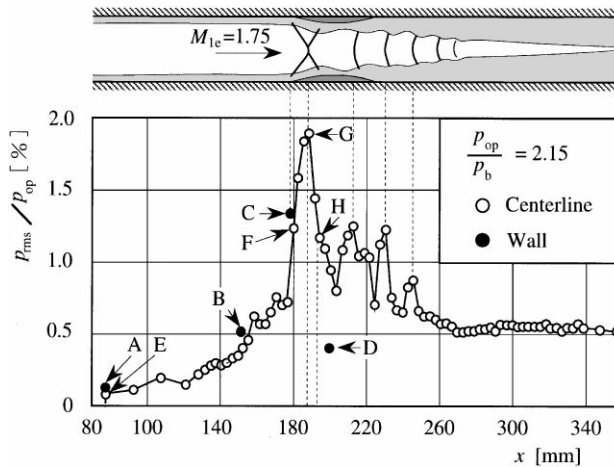


Fig. 52. Distribution of root-mean square of static pressure oscillations along centerline and wall of constant area duct (experimental data reproduced from Ref. [57]).

The root-mean-square (rms) values  $p_{rms}$  of the fluctuating static pressures normalized by the plenum pressure  $p_{op}$  are plotted against the distance from the test section inlet  $x$  in Fig. 52 [57], where the time-mean shock train position is also shown at the top for reference. The points marked A–H denote the values at points A–H in Fig. 50, respectively. Along the centerline, the  $p_{rms}$  increases very steeply at the first shock and shows the peaks at the points of the time-mean positions of the first and successive shocks. Downstream of the shock train, the  $p_{rms}$  tends to a nearly constant value, which is larger than the value far upstream of the shock. Note that the

value at the point *D* is about one-half of that at the centerline of the same cross section. This means that the flow near the centerline oscillates more violently than near the wall, and so a transverse consideration should be included in the analysis of the flow oscillations.

A qualitatively similar distribution of the root-mean-square values as that shown in Fig. 52 was obtained by Yamane et al. [54] for the pseudo-shock in a constant area duct, and by Chen et al. [117] and Matsuo et al. [122] for the wall pressure fluctuations in transonic and supersonic diffuser flows, respectively.

It has been observed in the previous experiments [53,56] on the pseudo-shock oscillations in constant area ducts that the amplitude of shock oscillations and the resulting pressure fluctuations increase with an increase in Mach number upstream of the shock, and that the spectral density distribution of the oscillation has two prominent peak frequencies, the lower one below a hundred Hz and the higher one of several hundred Hz. Also, the oscillation of the first shock is strongly correlated with the behaviors of the successive shocks [53,56]. The space–time correlation data with respect to the pressure fluctuations in the pseudo–shock region indicate that the oscillation of the first shock gives rise to the subsequent shock oscillations with some phase delay [123].

Recently, in addition to the streamwise oscillation of the pseudo-shock flows mentioned above, a low-frequency transverse oscillation was reported in a case of comparatively high Mach number flow by Carroll and Dutton [22]. These streamwise and transverse oscillations of flow in the pseudo-shock region produce a highly unsteady flow. Our present understanding of these unsteady flows is rather limited. There is not enough of the necessary basic data on the amplitudes of oscillation, the peak frequencies appearing in the shock displacement and/or pressure fluctuation power spectral density distributions, etc. The reason and flow mechanism of self-excited oscillation of the pseudo-shock have been left unsolved until now.

## 10. Concluding remarks

From those of old, the interaction between oblique shocks and boundary layers has been observed mainly in external flows, and the interaction of normal shocks with boundary layers most often in a variety of internal compressible flows. The strong interaction of normal shocks with boundary layers occurring in internal flows gives rise to shock trains or pseudo-shocks.

In this paper, previous experimental, analytical, and numerical investigations on the shock trains and pseudo-shocks were reviewed. The time-mean and oscillating characteristics of the shock trains and pseudo-shocks in constant area ducts were described. Some examples of shock trains and pseudo-shocks in various flow devices investigated in previous papers were also presented.

In addition to the subjects discussed in this paper, some other papers have been published so far concerning the pseudo-shocks, or the transition region from supersonic to subsonic velocities in internal flows. For example, Cuffel and Back [128], and Back et al. [129] conducted an experiment on the flow structure in a pseudo-shock region using a supersonic diffuser with surface cooling. Chen and Williams [130] investigated experimentally the transition from supersonic to subsonic flow in a circular tube at low Reynolds numbers. Hanzawa and Takashima [131] performed a numerical simulation on the pseudo-shocks in the case of a low-density supersonic flow in a straight duct.

The deceleration from supersonic to subsonic velocity through the pseudo-shock is a very complicated three-dimensional process, extending over a great distance along the flow direction. It is affected by the Mach number, the boundary layer thickness and the velocity distribution within the layer, the turbulence intensity of flow, the geometry of flow passage including its aspect ratio, the upstream and downstream flow conditions, particularly, the overall pressure ratio, etc.

The deceleration process greatly affects the performance and efficiency of flow devices. It almost always entail an increase in total pressure loss, hence deterioration of the performance of flow devices, and sometimes unsteadiness of the flow field. From the engineering and industrial point of view, it is desirable to develop proper control techniques to prevent such negative consequences. However, our current understanding of the mechanism and characteristics of the pseudo-shocks remains insufficient. There is a considerable amount of uncertainty still requiring a good deal of elucidation. A more thorough investigation is highly needed for fully understanding of the shock train and pseudo-shock phenomena.

## References

- [1] Green JE. Interactions between shock waves and turbulent boundary layers. *Prog Aerospace Sci* 1970;11:235–340.
- [2] Delery JM. Shock wave/turbulent boundary layer interaction and its control. *Prog Aerospace Sci* 1985;22(4):209–80.
- [3] Neumann EP, Lustwerk F. Supersonic diffusers for wind tunnels. *J Appl Mech* 1949;16(2):195–202.
- [4] Newman EP, Lustwerk F. High-efficiency supersonic diffusers. *J Aeronaut Sci* 1951;18(6):369–74.
- [5] Lukasiewicz J. Diffusers for supersonic wind tunnels. *J Aeronaut Sci* 1953;20(9):617–26.
- [6] Shapiro AH. The dynamics and thermodynamics of compressible fluid flow, vols. 1 and 2. New York: Ronald Press, 1953:135–9, 1153–56.
- [7] Tamaki T, Tomita Y, Yamane R. A study of pseudo-shock, 1st Report,  $\lambda$ -type pseudo-shock. *Bull JSME* 1970;13(55):51–8.
- [8] Tamaki T, Tomita Y, Yamane R. A study of pseudo-shock, 2nd Report, X-type pseudo-shock. *Bull JSME* 1971;14(74):807–17.
- [9] Waltrup PJ, Billig FS. Structure of shock waves in cylindrical ducts. *AIAA J* 1973;11(10):1404–8.
- [10] Waltrup PJ, Cameron JM. Wall shear and boundary-layer measurements in shock separated flow. *AIAA J* 1974;12(6):878–80.
- [11] Ikui T, Matsuo K, Nagai M. The mechanism of pseudo-shock waves. *Bull JSME* 1974;17(108):731–9.
- [12] Ostras VN, Penzin VI. Experimental study of friction in a channel with a pseudo-shock. *Fluid Mech Soviet Res* 1975;4(6):32–8.
- [13] Merkli PE. Pressure recovery in rectangular constant area supersonic diffusers. *AIAA J* 1976;14(2):168–72.
- [14] Mateer GG, Viegas JR. Mach and Reynolds number effects on a shock-wave/boundary-layer interaction. *AIAA J* 1980;18(8):1016–8.
- [15] Ikui T, Matsuo K, Sasaguchi K. Modified diffusion model of pseudo-shock waves considering upstream boundary layers. *Bull JSME* 1981;24(197):1920–7.
- [16] Om D, Viegas JR, Childs ME. Transonic shock-wave/turbulent boundary-layer interactions in a circular duct. *AIAA J* 1985;23(5):707–14.
- [17] Om D, Childs ME. Multiple transonic shock-wave/turbulent boundary-layer interaction in a circular duct. *AIAA J* 1985;23(10):1506–11.
- [18] Ktarkherman MG, Mal'kov VM, Ruban NA. Slowing down of a supersonic flow in a rectangular channel of constant cross section. *J Appl Mech Tech Phys* 1985;25(6):854–62.
- [19] Sugiyama H, Takeda H, Zhang J, Abe F. Multiple shock wave and turbulent boundary layer interaction in a rectangular duct. In: Gronig H, editor. Shock tubes and waves, Proc 16th Int Symp on Shock Tubes and Waves. VCH 1987:185–91.

- [20] Arai T, Sugiyama H, Abe F, Takahashi T, Onodera O. Internal structure of pseudo-shock waves in a square duct. In: Kim YM, editor. Current topics in shock waves, 17th Int Symp on Shock Waves and Shock Tubes. Lehigh Univ. 1990:850–5.
- [21] Sugiyama H, Arai T, Uno N, Takahashi T. Three-dimensional structure of pseudo-shock wave in a rectangular duct. In: Takayama K, editor. Shock waves. Proc 18th Int Symp on Shock Waves, Berlin: Springer, 1991; 1:631–6.
- [22] Carroll BF, Dutton JC. Characteristics of multiple shock wave/turbulent boundary-layer interactions in rectangular ducts. *J Propulsion Power* 1990;6(2):186–93.
- [23] Carroll BF, Dutton JC. Turbulence phenomena in a multiple normal shock wave/turbulent boundary-layer interaction. *AIAA J*. 1992;30(1):43–8.
- [24] Carroll BF, Dutton JC. Multiple normal shock wave/turbulent boundary-layer interactions. *J Propulsion Power* 1992;8(2):441–8.
- [25] McCormick DC. Shock/boundary-layer interaction control with vortex generators and passive cavity. *AIAA J* 1993;31(1):91–6.
- [26] Sugiyama H, Arai T, Hongo S, Kawase T, Uno N. Structure of multiple shock-wave/turbulent boundary-layer interactions in a rectangular duct. In: Sturtevant B, Shepherd JE, Hornung HG, editors. Shock waves. Proc 20th Int Symp on Shock Waves, Singapore: World Scientific, 1995;1:729–34.
- [27] Nill LD, Mattick AT. An experimental study of shock structure in a normal shock train. *AIAA Paper No.96-0799*, 1996.
- [28] Sugiyama H, Arai T, Uno N, Wang Y. Structure and turbulence phenomena of multiple shock wave/turbulent boundary layer interaction in a supersonic duct. *JSME Centennial Grand Congress, Int Conf on Fluid Engineering* 1997;3:1205–10.
- [29] Kim HD. An experimental study of weak normal shock-wave/turbulent boundary-layer interaction in internal flows. PhD Thesis, Kyushu University, Japan, 1991.
- [30] Nussdorfer TJ. Some observations of shock-induced turbulent separation on supersonic diffusers. *NACA R.M. E51L26*, 1954.
- [31] Crocco L. One-dimensional treatment of steady gas dynamics. In: Emmons HW, editor. Fundamentals of gas dynamics, Princeton: Princeton University Press, 1958:110–30.
- [32] Ikui T, Matsuo K. Researches of supersonic flow with the shock wave as main subject. *J JSME* 1969;72(609):1306–12 (in Japanese).
- [33] Cohen CB, Valerino AS. Investigation of operating pressure ratio of a supersonic wind tunnel utilizing distributed boundary-layer suction in test section. *NACA Res Memo E50H04*, 1950.
- [34] Faro IDV, editor. Handbook of supersonic aerodynamics, vol. 6. sec. 17, Navweps Rep. 1488, 1964.
- [35] Billig FS. Combustion processes in supersonic flow. *J Propulsion Power* 1988;4(3):209–216.
- [36] Stockbridge RD. Experimental investigation of shock wave/boundary-layer interactions in an annular duct. *J Propulsion Power* 1989;5(3):346–52.
- [37] Hunter LG, Couch BD. A CFD study of precombustion shock-trains from Mach 3–6. *AIAA Paper No.90-2220*, 1990.
- [38] Lin P, Rao GVR, O'Connor GM. Numerical analysis of normal shock train in a constant area isolator. *AIAA Paper No. 91-2162*, 1991.
- [39] Sajben M, Donovan JF, Morris MJ. Experimental investigation of terminal shock sensors for mixed-compression inlets. *J Propulsion Power* 1992;8(1):168–74.
- [40] Sullins G, McLafferty G. Experimental results of shock trains in rectangular ducts. *AIAA Paper No.92-5103*, 1992.
- [41] Anderson JD, Jr. Modern compressible flow with historical perspective. New York: McGraw-Hill, 1990:93–5.
- [42] Thompson PA. Compressible-fluid dynamics. New York: McGraw-Hill, 1972:305.
- [43] Hataue I. Computational study of the shock-wave/boundary-layer interaction in a duct. *Fluid Dyn Res* 1989; 5(3):217–34.
- [44] Lin P, Rao GVR, O'Connor GM. Numerical investigation on shock wave/boundary layer interactions in a constant area diffuser at Mach 3. *AIAA Paper No.91-1766*, 1991.
- [45] Carroll BF, Lopez-Fernandez PA, Dutton JC. Computations and experiments for a multiple normal shock/boundary-layer interaction. *J Propulsion Power* 1993;9(3):405–11.



- [46] Yamane R, Oshima S, Nakamura Y, Ishii T, Park MK. Numerical simulation of pseudo-shock in straight channels. *JSME Int J Ser B* 1995;38(4):549–54.
- [47] Knight DD. A hybrid explicit-implicit numerical algorithm for the three-dimensional compressible Navier–Stokes equations. *AIAA J* 1984;22(8):1056–63.
- [48] Viegas JR, Horstmann CC. Comparison of multi-equation turbulent models for several shock boundary-layer interaction flows. *AIAA J* 1979;17(8):811–20.
- [49] Zimont VL, Ostras VN. Calculation of pseudo-shocks in a cylindrical duct. *Fluid Mec Soviet Res* 1976;5(2):78–87.
- [50] Shchetnikov ES. Piecewise-one-dimensional models of supersonic combustion and pseudo-shock in a duct. *Comb Expl Shock Waves* 1975;9(4):409–17.
- [51] Nagai M, Yaga M. On the pseudo-shock wave relations. In: Kral LD, Spina EF, Arakawa C, editors. *ASME FED. vol. 224, Transitional and turbulent compressible flows*. New York: The American Society of Mechanical Engineers, 1995:103–8.
- [52] Matsuo K, Miyazato Y, Kim HD. Mass-averaging pseudo-shock model in a straight flow passage. *J Aerospace Eng* 1998 (to be published).
- [53] Ikui T, Matsuo K, Nagai M, Honjo M. Oscillation phenomena of pseudo-shock waves. *Bull JSME* 1974;17(112):1278–1285.
- [54] Yamane R, Kondo E, Tomita Y, Sakae N. Vibration of pseudo-shock in straight duct, 1st Report, Fluctuation of static pressure. *Bull JSME* 1984;27(229):1385–92.
- [55] Yamane R, Takahashi M, Saito H. Vibration of pseudo-shock in straight duct, 2nd Report, Correlation of static pressure fluctuation. *Bull JSME* 1984;27(229):1393–8.
- [56] Sugiyama H, Takeda H, Zhang J, Okuda K, Yamagishi H. Locations and oscillation phenomena of pseudo-shock waves in a straight rectangular duct. *JSME Int J Ser II* 1988;31(1):9–15.
- [57] Matsuo K, Mochizuki H, Miyazato Y, Gohya M. Oscillatory characteristics of a pseudo-shock wave in a rectangular straight duct. *JSME Int J Ser B* 1993;36(2):222–9.
- [58] Waltrup PJ, Billig FS. Prediction of precombustion wall pressure distributions in scramjet engines. *J Spacecraft Rockets* 1973;10(9):620–2.
- [59] Bement DA, Stevens JR, Thompson MW. Measured operating characteristics of a rectangular combustor/inlet isolator. *AIAA Paper No.90-2221*, 1990.
- [60] Selig MS, Andreopoulos J, Muck KC, Dussauge JP, Smits AJ. Turbulence structure in a shock wave/turbulent boundary-layer interaction. *AIAA J* 1989;27(7):862–9.
- [61] Doerffer P, Dallmann U. Reynolds number effect on separation structures at normal shock wave/turbulent boundary-layer interaction. *AIAA J* 1989;27(9):1206–12.
- [62] Chakravarthy SR, Osher S. A new class of high accuracy TVD schemes for hyperbolic conservation laws, *AIAA Paper No.85-0363*, 1985.
- [63] Visbal M, Knight D. The Baldwin–Lomax turbulence model for two-dimensional shock-wave/boundary-layer interactions. *AIAA J* 1984;22(7):921–8.
- [64] Marshall TA, Dolling DS. Computation of turbulent, separated, unswept compression ramp interactions. *AIAA J* 1992;30(8):2056–65.
- [65] Goldberg UC. Separated flow treatment with a new turbulence model. *AIAA J* 1986;24(10):1711–3.
- [66] Goldberg UC, Chakravarthy SR. Prediction of separated flows with a new backflow turbulence model. *AIAA J* 1988;26(4):405–8.
- [67] Ikui T, Matsuo K, Mochizuki H, Somekawa K. Pseudo-shock waves in a divergent channel. *Bull JSME* 1980;23(175):20–5.
- [68] Liepmann HW, Roshko A. *Elements of gas dynamics*. New York: Wiley 1957:124–36.
- [69] Wegener PP, Lobb RK. An experimental study of a hypersonic wind-tunnel diffuser. *J Aeronaut Sci* 1953;20(2):105–10.
- [70] Matsuo K, Sasaguchi K, Mochizuki H, Takechi N. Investigation of the starting process of a supersonic wind tunnel. *Bull JSME* 1980;23(186):1975–81.
- [71] Eggink H. The improvement in pressure recovery in supersonic wind tunnels. *Aeronaut Res Council, Rep and Memo No 2703*, 1953.

- [72] Panchenko VI. Determination of minimal supersonic diffuser throat length, *Izvestiya VUZ. Aviatsionnaya Tekhnika* 1990;33(3):25–8.
- [73] Johnson JA III, Wu BJC. Pressure recovery in supersonic diffusers. *Trans ASME J Fluids Eng* 1975;97(3):374–6.
- [74] Sajben M, Bogar TJ, Kroutil JC. Experimental study of flows in a two-dimensional inlet model. *J Propulsion Power* 1985;1(2):109–17.
- [75] Talcott NA Jr, Kumar A. Two-dimensional viscous simulation of inlet/diffuser flows with terminal shocks. *J Propulsion Power* 1985;1(2):103–8.
- [76] Chyu WJ, Kawamura T, Benze DP. Navier–Stokes solutions for mixed compression axisymmetric inlet flow with terminal shock. *J Propulsion Power* 1989;5(1):4–5.
- [77] Hamed A, Shang JS. Survey of validation data base for shock wave boundary-layer interactions in supersonic inlets. *J Propulsion Power* 1991;7(4):617–25.
- [78] Mahoney JJ. Inlets for supersonic missiles. *American Institute of Aeronautics and Astronautics*, 1990:55–66.
- [79] Curran ET, Heiser WH, Pratt DT. Fluid phenomena in scramjet combustion systems. *Annu Rev Fluid Mech* 1996;28:323–60.
- [80] Power RB. Steam jet ejectors for the process industries. New York: McGraw-Hill 1994:1–33.
- [81] Addy AL, Chow WL. On the starting characteristics of supersonic ejector systems. *Trans AMSE Ser D J Basic Eng* 1964;86(4):861–8.
- [82] German RC, Bauer RC, Panesci JH. Methods for determining the performance of ejector-diffuser systems. *J Spacecraft Rockets* 1966;3(2):193–200.
- [83] Quinn B. Ejector performance at high temperatures and pressures. *J Aircraft* 1976;13(12):948–54.
- [84] Alperin M, Wu JJ. Thrust augmenting ejectors. Part 1, *AIAA J* 1983;21(10):1428–36, Part 2, *AIAA J* 1983;21(12):1698–706.
- [85] Fabri J, Siestrunk R. Supersonic air ejectors. In: Dryden HL, von Karman T, editors. *Advances in applied mechanics*, vol. 5, New York: Academic Press, 1958: pp. 1–34.
- [86] Matsuo K, Sasaguchi K, Kiyotoki Y, Mochizuki H. Investigation of supersonic air ejectors, Part 2, Effects of throat-area-ratio on ejector performance. *Bull JSME* 1982;25(210):1898–905.
- [87] Dutton JC, Carroll BF. Limitation of ejector performance due to exit choking. *Trans ASME Ser I J Fluids Eng* 1988;110(1):91–3.
- [88] Matsuo K, Sasaguchi K, Tasaki K, Mochizuki H. Investigation of supersonic air ejectors, Part 1, Performance in the case of zero-secondary flow. *Bull JSME* 1981;24(198):2090–7.
- [89] Matsuo K, Mochizuki H, Kobayashi A. On the double-vacuum phenomenon of a supersonic air ejector. *Bull JSME* 1986;29(251):1434–9.
- [90] Gaydon AG, Hurler IR. *The shock tube in high-temperature chemical physics*. London: Chapman & Hall 1963;1–82.
- [91] Matsuo K, Kage K, Kawagoe S. The interaction of a reflected shock wave with the contact region in a shock tube. *Bull JSME* 1975;18(121):681–8.
- [92] Mori H. A theoretical investigation of pressure depression in externally pressurized gas-lubricated circular thrust bearings. *Trans ASME Ser D J Basic Eng* 1961;83(2):201–8.
- [93] Mori H, Ezuka H. A pseudo-shock theory of pressure depression in externally pressurized circular thrust gas bearings, *Preprints of JSLE-ASLE Int Lubrication Conf* 1975:115–22.
- [94] Yamane R, Oshima S, Takahashi M, Tamaki H. Pseudo-shock in radial supersonic flow. *Bull JSME* 1985;28(235):46–53.
- [95] Yamane R, Oshima S, Okada K. Pseudo-shock in radial supersonic flow with swirl. *Bull JSME* 1984; 27(229):1467–71.
- [96] Louis JF, Gal G, Blackburn PR. Detailed theoretical and experimental study on a large MHD generator. *AIAA J* 1965;3(8):1482–90.
- [97] Roy GD, Wu YCL. Study of pressure distribution along supersonic magnetohydrodynamic generator channel. *AIAA J* 1975;13(9):1149–53.
- [98] Lu PC, Wang KH. MHD pseudo-shock and qualitative model in the performance of supersonic generators. *J Energy* 1983;7(3):211–7.

- [99] Okubo M, Tanemoto F, Yamada K, Kushida L, Yamasaki H, Biswas D. Numerical simulations and experimental studies on supersonic flow in disk channel. *Proc. 17th Symp on Efficient Use of Energy and Direct Electrical Power Generation*, 1995:171–82.
- [100] Seki Y, Teramoto Y, Maeda T, Hagita T, Yoshikawa K, Shioda S, Yamasaki H. Asymmetric flow behavior in disk MHD generator. *Proc. 12th Int Conf on Magnetohydrodynamic Electrical Power Generation* 1996;2:729–35.
- [101] Suekane T, Maeda T, Okuno Y, Kabashima S. Numerical simulation on MHD flow in disk closed cycle MHD generator. *AIAA Paper No.97-2396*, 1997.
- [102] Veret C, Philbert M, Surget T, Fertin G. Aerodynamic flow visualization in the ONERA facilities. *Proc Int Symp on Flow Visualization*, 1977:255–60.
- [103] Philbert M, Fertin G. Schlieren systems for flow visualization in axial and radial flow compressors. *Trans ASME Ser A. J Eng Power* 1975;97(2):254–60.
- [104] Reethof G, Ward WC. A theoretically based valve noise prediction method for compressible fluids. *Trans ASME J Vib Acoust Stress Reliability Des* 1986;108(3):329–38.
- [105] Buresh JF, Schuder CB. The development of a universal gas sizing equation for control valves. *ISA (Instrument Society of America) Trans* 1964;3(4):322–8.
- [106] Addy AL, Morris MJ, Dutton JC. An investigation of compressible flow characteristics of butterfly valves. *Trans ASME J Ser I. J Fluids Eng* 1985;107(4):512–7.
- [107] Nakano M, Outa E, Tajima K. Noise and vibration related to the patterns of supersonic annular flow in a pressure reducing gas valve. *Trans ASME Ser I J Fluids Eng* 1988;110(1):55–61.
- [108] Brandmaier HE, Knebel ME. Steam flow through safety valve vent pipes. *Trans ASME Ser I J Fluids Eng* 1976;98(2):199–207.
- [109] Mattick AT, Hertzberg A, Russel DA. Shock controlled reactors. In: Takayama K, editor. *Shock Waves. Proc. 18th Int Symp on Shock Waves*, Berlin: Springer 1991;2:1289–94.
- [110] Mattick AT, Russel DA, Hertzberg A, Knowlen C. Shock-controlled chemical processing. In: Brun R, Dumitrescu LZ, editors. *Shock waves @ Marseille II*, Proc. 19th Int Symp on Shock Waves, Berlin: Springer, 1995:209–14.
- [111] Raghunathan S. Passive control of shock-boundary layer interaction. *Prog Aerospace Sci* 1988;25(3):271–96.
- [112] Weise A. The separation of flow due to compressibility shock. *NACA TM No.1152*, 1947.
- [113] Matsuo K, Mochizuki H, Miyazato Y, Yaga M. An application of passive boundary layer control to pseudo-shock waves. *Proc 2nd KSME-JSME Fluids Engineering Conf* 1990;2:64–69.
- [114] Hasinger SH, Miller DK. Two-dimensional supersonic diffuser experiments. *AIAA J* 1975;13(4):536–8.
- [115] Miyazato Y, Matsuo K, Furukawa Y, Yokoyama M, Mochizuki H. Flow visualization of passive shock-wave/boundary-layer interaction control. In: Nakayama Y, Tanahashi T, editors. *Proc 3rd Asian Symp on Visualization*, Shunkosha 1994:301–6.
- [116] Sajben M, Kroutil JC, Chen CP. Unsteady transonic flow in a two-dimensional diffuser. *AGARD No.227*, 1977.
- [117] Chen CP, Sajben M, Kroutil JC. Shock-wave oscillations in a transonic diffuser flow. *AIAA J* 1979;17(10):1076–83.
- [118] Bogar TJ, Sajben M, Kroutil JC. Characteristics frequencies of transonic diffuser flow oscillations. *AIAA J* 1983;21(9):1232–40.
- [119] Bogar TJ. Structure of self-excited oscillations in transonic diffuser flows. *AIAA J* 1986;24(1):54–61.
- [120] Hsieh T, Bogar TJ, Coakley TJ. Numerical simulation and comparison with experiment for self-excited oscillations in a diffuser flow. *AIAA J* 1987;25(7):936–43.
- [121] Kim HD, Matsuo K, Kawagoe S, Kinoshita T. Flow unsteadiness by weak normal shock wave/turbulent boundary layer interaction in internal flow. *JSME Int J Ser II* 1991;34(4):457–65.
- [122] Matsuo K, Kim HD. Normal shock wave oscillations in supersonic diffusers. *Shock Waves* 1993;3:25–33.
- [123] Miyazato Y, Kashitani M, Matsuo K. Flow oscillation induced by normal shock wave/turbulent boundary-layer interaction in a supersonic diffuser. In: Crowder JP, editor. *Flow visualization 7. Proc 7th Int Symp on Flow Visualization*, Begell House, 1995:853–8.
- [124] Meier GEA, Szumowski AP, Selerowicz WC. Self-excited oscillations in internal transonic flows. *Prog Aerospace Sci* 1990;27:145–200.
- [125] Kistler AL. Fluctuating wall pressure under a separated supersonic flow. *J Acoust Soc Amer* 1964;36(3):543–50.
- [126] Dolling DS, Murphy MT. Unsteadiness of the separation shock wave structure in a supersonic compression ramp flowfield. *AIAA J* 1983;21(12):1628–34.

- [127] Hayashi M, Aso S, Tan A. Fluctuation of heat transfer in shock wave/turbulent boundary-layer interaction. *AIAA J* 1989;27(4):399–404.
- [128] Cuffel RF, Back LH. Flow and heat transfer measurements in a pseudo-shock region with surface cooling. *AIAA J* 1976;14(12):1716–22.
- [129] Back LH, Cuffel RF, Massier PF. Flow and heat transfer measurements along a cooled supersonic diffuser. *AIAA J* 1984;22(6):777–80.
- [130] Chen RY, Williams JC III. On transition from supersonic to subsonic flow at low Reynolds number in a tube. *Trans ASME Ser E J Appl Mech* 1969;36(2):146–50.
- [131] Hanzawa M, Takashima Y. Numerical simulation on low density supersonic flow in a straight duct. *Bull Res Laboratory for Nucl Reactors* 1981;6:11–22.